ABSTRACT

RADIO-DERIVED THREE-DIMENSIONAL STRUCTURE OF A SOLAR ACTIVE REGION

by
Samuel D. Tun

Solar active regions are the source of the most violent events observed on the Sun, some of which have a direct impact to modern civilization. Efforts to understand and predict such events require determination of the three-dimensional distributions of density, temperature, and magnetic fields above such active regions. This thesis presents the structure of the solar atmosphere above active region AR 10923, observed on 2006 Nov 10, as deduced from multi-wavelength studies including combined microwave observations from the Very Large Array (VLA) and the Owens Valley Solar Array (OVSA). The VLA observations provide excellent image quality at a few widely spaced frequencies while the OVSA data provide information at many intermediate frequencies to fill in the spectral coverage. In order to optimize the OVSA data for spectroscopic studies, the L1 method of self-calibration was implemented at this observatory, producing the best single frequency maps produced to date. Images at the 25 distinct, available frequencies are used to provide spatially resolved spectra along many lines of sight in the active region, from which microwave spectral diagnostics are obtained for deducing two-dimensional maps of temperature, magnetic field strength, and column density.

The derived quantities are compared with multi-wavelength observations from *SoHO* and *Hinode* spacecraft, and with a standard potential magnetic field extrapolation. It is found that a two component temperature model is required to fit the data, in which a hot (> 2 MK) lower corona above the strong-field plage and sunspot regions (emitting via the gyroresonance process) is overlaid with somewhat cooler

($\sim$ 1 MK) coronal loops that partially absorb the gyroresonance emission through the free-free (Bremsstrahlung) process. It is also found that the potential magnetic field extrapolation model can quantitatively account for the observed gyroresonance emission over most of the active region, but in a few areas a higher field strength is required. These areas of discrepancy are found to coincide with the foot points of hot X-ray loops over the sunspot's penumbra. The results and the extrapolation are used to explore the coronal configuration needed to explain the observations, from which it is found that the bulk of radio and X-ray free-free emission emanates from two loop systems, distinguished by the location of their loop foot points. The proposed stratification may explain the observed distribution of column emission measure and the differences in this quantity as obtained from X-rays or radio emission.

RADIO-DERIVED THREE-DIMENSIONAL STRUCTURE OF A SOLAR ACTIVE REGION

by
Samuel D. Tun

A Dissertation
Submitted to the Faculty of
New Jersey Institute of Technology and
Rutgers, The State University of New Jersey – Newark
in Partial Fulfillment of the Requirements for the Degree of
Doctor of Philosophy in Applied Physics

Federated Physics Department

January 2011

APPROVAL PAGE

RADIO-DERIVED THREE-DIMENSIONAL STRUCTURE OF A SOLAR ACTIVE REGION

Samuel D. Tun

Dr. Dale E. Gary, Dissertation Advisor — Date
Distinguished Professor of Physics, Director of Owens Valley Solar Array, NJIT

Dr. Haimin Wang, Committee Member — Date
Distinguished Professor of Physics, Associate Director of Center for Solar-Terrestrial Research and Big Bear Solar Observatory, NJIT

Dr. Daniel Murnick, Committee Member — Date
Professor of Physics, Rutgers

Dr. Tao Zhou, Committee Member — Date
Associate Professor of Physics, NJIT

Dr. Tim Bastian, Committee Member — Date
Astronomer, NRAO

BIOGRAPHICAL SKETCH

Author: Samuel Dionisio Tun Beltran

Degree: Doctor of Philosophy

Date: January, 2011

Undergraduate and Graduate Education:

Doctor of Philosophy in Applied Physics, New Jersey Institute of Technology, Newark, NJ, 2011

Bachelor of Science in Physics with Astrophysics Option, New Mexico Institute of Mining and Technology, Socorro, NM, 2003

Major: Applied Physics

Presentations and Publications:

Tun, S.D., Gary, D.E., Georgoulis, M.K., "Three-dimensional Structure of a Solar Active Region from Spatially and Spectrally Resolved Microwave Observations," The Astrophysical Journal, in press.

Tun, Samuel D., "Coronal active region structure results from joint OVSA-VLA observations," Plenary Talk, Community of European Solar Radio Astronomers Meeting, La Roche en Ardenne, Belgium, May 2010.

Tun, Samuel D., "Derivation of the Magnetic Field Configuration above a Solar Active Region using Spatio-spectral Radio Data from the OVSA," American Astronomical Society, SPD meeting #40, #29.03, Oral Presentation, Boulder, CO, May 2009.

Tun, Samuel D., Gary, D. E., Nita, G. M., Lee, J., "Analysis of a Flare Producing Active Region Using Data from the Upgraded OVSA," American Astronomical Society, SPD meeting #37, #1.17, Durham, NH, June, 2006.

Tun, S. D., Gary, D., White, S. M., "Antenna Configurations for the FASR B Array," American Geophysical Union, Spring Meeting 2005, abstract #SP43A-09, New Orleans, LA, May 2005.

Tun, S. D., Gary, D. E., Lee, J., "Simulation of Microwave Emissions from Helmet Streamer," American Astronomical Society Meeting 204, #71.02, Denver, CO, May, 2004.

To Raquel and Angelos, whose love and support are truly the reasons why any of this is possible. To Ruth, Juan, Samuel, Jose, and Ruth who have been patient and loving through my endeavors. To my parents, Ruth and Samuel, who inculcated a love and respect towards learning and brought me to this big, wonderful land of immense opportunities. And to my eternal muse, whose universal beauty beckons me into the secret and unknown to now and forever explore.

ACKNOWLEDGEMENT

I would like to thank my advisor, Dr. Dale Gary, for taking me in and guiding me along while investing in me quite a bit of trust and, I suppose, some faith that I would figure things out for myself. He supported and stood by me much farther than I thought any advisor would. The members of my committee allowed me to proceed with what was an ambitious endeavor, and it has paid off. Although ambitious in its goals, this thesis presents results akin to those initially sought, but arrived at through a different set of techniques. The committee members were also constructive at the end, and I felt immense pleasure at the treatment I received at my defense, that of a true scientist. Dr. Stephen White was of great help during the observations at the VLA, as well as Dr. Tim Bastian who also applied the SOLCAL calibration to the VLA data. I am also grateful to Dr. A. Vourlidas for crucial discussions on solar radio emission and the interpretation of radio data, and for unfaltering moral support. I would very much like to thank Christine Oertel for helping me, even rescuing me from myself, in getting all paperwork and various deadlines met. The folks over at C2PRISM were simply great, allowing me to carry out and improve upon one of my interests, education, and support myself at the same time. I do believe that I am a better scientist, educator, and public speaker as a result. And where would I be without the various friends that I have made throughout my years at NJIT. Although I've much neglected them in the later parts, they've been patient and always supportive through my times of doubt, and joyous with me in my triumphs.

This work was supported by NSF grant AST-0908344, NASA grant NNG06GJ40G and NSF GK-12 Award 0638423 to the New Jersey Institute of Technology.

TABLE OF CONTENTS

Chapter **Page**

TABLE OF CONTENTS
(Continued)

Chapter **Page**

LIST OF FIGURES

Figure **Page**

Figure **Page**

Figure **Page**

Figure **Page**

Figure **Page**

LIST OF FIGURES

(Continued)

Figure **Page**

LIST OF ACRONYMS

AO	Adaptive Optics
AOA	Adaptive Optics Associates
xxxx	xxx
AR:	active region
β:	ratio of plasma pressure to magnetic pressure
B_l (B_z):	line of sight component of the magnetic field
B_{tot} (B)	total magnetic field strength
ff:	free-free, or bremsstrahlung
FOV:	field of view
GHz:	Giga-Hertz (1×10^9Hz)
kG:	kilo-Gauss
LFFF:	linear force-free field
EM:	emission measure
EUV:	extreme ultraviolet
gyro:	gyroresonance
g_m:	complex gain of the mth antenna
h:	height above the photosphere
MK:	Mega-Kelvin (1×10^6K)
N:	number of antennas in an array
NLFFF:	non-linear force-free field
n_e:	electron density
ν:	frequency
ν_B:	fundamental gyrofrequency
$\nu_{tau=1}$	frequency at the spectrum turnover
OVSA:	Owens Valley Solar Array
o-mode:	ordinary mode
ROI:	Region Of Interest, an IDL routine as well as a selected region
s:	harmonic of the fundamental gyrofrequency, an integer (s=1, 2, 3, ...)
τ:	optical depth in free-free emission, parameter in gyroresonance spectra
T_b:	brightness temperature
T_e:	electron temperature
θ:	angle between the magnetic field vector and the line of sight
$\hat{V}_{mn}$:	true sky visibilities
$\tilde{V}_{mn}$:	observed visibilities
VLA:	Very Large Array
x-mode:	extraordinary mode

CHAPTER 1

INTRODUCTION

1.1 Motivation and Thesis Structure

A sunspot is the photospheric bisection of strong magnetic fields originating from plasma currents in the solar interior. A simple sunspot consists of a dark central region, the umbra, surrounded by a lighter, concentric region called the penumbra. The umbra is characterized by having the strongest, vertically directed magnetic fields along with temperature and height depressions from the surrounding photosphere. While the photosphere has a typical temperature of 5780 K, a sunspot umbra has temperatures ranging from $3,400$-4500 K. Magnetic field lines in the penumbra are more inclined than in the umbra, and a rise in temperature reduces their observable contrast to the surrounding photosphere. The photosphere surrounding a sunspot contains a scattered distribution of magnetic flux, and in conjunction with the sunspot these domains comprise a solar active region (AR). Vertically, the temperature increases with height to the chromosphere, which has a mean temperature of $10,000$ K. Although the average height of the chromosphere is about 2000 km, the chromosphere is an extremely inhomogeneous region, with mottles and spicules protruding upwards to heights of 5000 km above the solar surface (Stix 2004). Above the chromosphere is a temperature discontinuity of several millions of degrees, through what is known as the transition region. This region is also inhomogeneous in shape and height, although it is generally considered spatially thin. It is in this region that the plasma temperature rises abruptly to coronal values. The corona, the highest and thickest layer of the solar atmosphere, is characterized by a low plasma density, a high kinetic temperature of several millions of degrees, and is permeated by magnetic fields.

The magnetic pressure dominates over the plasma pressure in the corona, so that the magnetic field controls the distribution of the density and temperature.

In addition, the release of magnetic energy is proposed to be the chief mechanism for energy deposition from sub-surface processes into the million-degree corona (Aschwanden, 2006). Great effort has been expended towards determining the three-dimensional distribution of the magnetic field, temperature, and density of the corona above solar active regions in order to understand magnetic energy storage and subsequent release. Radio observations of the Sun provide a powerful diagnostic of the coronal plasma since they offer a direct measure of the source's electron temperature (T_e), column emission measure (EM), and, depending on the responsible emission mechanism, the total magnetic field strength ($B_{\rm tot}$) or its component (B_l) along the line of sight (Gary & Hurford, 2004). There are two radiation mechanisms that dominate the radio emission of the corona from 1-20 GHz: free-free (bremsstrahlung) and gyroresonance emission (White & Kundu, 1997). The two mechanisms exhibit easily identifiable spectral behavior if sufficient frequency coverage is available, and the aforementioned physical quantities can be directly obtained from spatially resolved spectra, as will be discussed in section 3.4.

Zheleznyakov (1962) and Kakinuma & Swarup (1962) independently established, on theoretical grounds, that gyroresonance emission must be responsible for the sunspot-associated emission at centimetric wavelengths. Studies at one or a few widely-spaced frequencies confirmed this picture (e.g. Lang & Willson, 1980, 1982; Alissandrakis & Kundu, 1982; Chiuderi-Drago et al., 1982; Shevgaonkar & Kundu, 1985; Gopalswamy et al., 1991; Zlotnik et al., 1996, 1998), while optically thin free-free emission was found to be responsible for the plage associated component at these same wavelengths (Felli et al., 1981; Gary & Hurford, 1987). Studies at decimetric wavelengths verified that optically thick free-free emission is responsible for the radiation at these longer wavelengths (Chiuderi Drago et al., 1977; Dulk & Gary, 1983; Lang & Willson, 1982; Lang et al., 1983), although gyroemission may still contribute somewhat in this regime (Lang et al., 1987a,b; White et al., 1992; Vourlidas et al.,

1996). The transition between the dominance of the two mechanisms occurs around 10 cm (Gary & Hurford, 1987). At very short centimetric wavelengths ($\leq$ 2cm) the emission is again due to free-free emission, but emanates from the much cooler chromosphere or from the transition region (Shevgaonkar & Kundu, 1985; Hurford, 1986; Gary & Hurford, 1987). These single-frequency studies determined that, in general, free-free emission dominates at lower frequencies while gyroresonance emission does so at higher ones. This has implications for the distribution of plasma in height above the active region since emission observed at higher frequencies emanates from deeper in the corona (lower heights above the photosphere) than the radiation at longer wavelengths.

These two mechanisms exhibit distinct frequency spectra (Gary & Hurford, 2004) and spectroscopic analysis of spatially and spectrally resolved radio data returns model-independent physical parameters. The difficulty in carrying out such studies stems from the lack of instruments able to obtain high-fidelity maps at many closely-spaced frequencies. This issue has been addressed by averaging the observed radio flux over the entire source, by fitting models to the spectra from widely-spaced frequencies, modeling of the parameters that reproduce the observations, or by using lunar limb occultations during an eclipse to decrease the complexity of the radio sources. Analysis through such a lunar limb rastering by Gary & Hurford (1987) in conjunction with a potential field extrapolation suggested that the free-free emission at 1.45 GHz originated from the tops of loops connecting the sunspots in the AR. Spectral analysis of source-averaged Owens Valley Solar Array (OVSA) data allowed Lee et al. (1993) to detect a free-free component previously dominated by the gyroresonance signature at higher temperature when their target AR crossed over the limb. Implicit in the geometry of the observations is that the AR had a mega-Kelvin (MK) free-free component overlying a hotter gyroresonance component, which was obscured by the limb when the AR crossed beyond. Gary & Hurford (1994) fit OVSA

data with model spectra representative of free-free or gyroemission. In this manner they produced two-dimensional maps of the T_e, EM, and $B_{\rm tot}$ distributions above their active region as projected onto the sky plane. While most of their averaged spectra conformed to a homogeneous corona model, several spectra were found to have positive slopes in the optically thick part corresponding to low frequencies, and were ill-fit with the homogeneous temperature models used. In a study using spectra from the sparse frequencies available from the Very Large Array (VLA), Vourlidas et al. (1997) showed that these were best fit by a multi-thermal free-free emission model. However, they too had some spectra that suggested a high positive slope in the optically thick, low-frequency portion which could not be explained by their free-free only models. For those spectra, they concluded that gyroresonance emission was responsible for the radiation at 4.8 GHz and above. They also concluded that the umbral and penumbral environments are distinct, and that the hot loops anchored in the penumbra are associated with X-ray emission. In a prior study, Vourlidas et al. (1996) found that the soft X-ray and 1.5 GHz VLA observations came from similar structures at the tops of the longest loops connecting the two sunspots in the region, similar to the findings of Gary & Hurford (1987). In their schematic representation of the morphology of the atmosphere as suggested by the analysis, the free-free emission at longer wavelengths comes from greater heights than the sources of the 4.7 and 8.4 GHz emission.

Lower in the solar atmosphere, there is a strong indication of the existence of cool material directly above sunspot umbrae. The first evidence of this was derived from extreme ultra-violet (EUV) (Foukal et al 1974, 1975, 1976) and X-ray (Webb and Zirin 1981) observations. Radio observations at 6 cm and shorter wavelengths presented features explainable by the existence of cooler plasma over the penumbra (Kundu and Velusamy 1980 ; Kundu, Schmahl, and Rao 1981; Alissandrakis and Kundu, 1982; Alissandrakis et. Al. 1993; Zlotnik et al 1997). Studies combining

radio observations with X-ray (Siarkowski et al 1989) and EUV (Brosius and White 2004) data have also arrived at this conclusion. However, a few studies conclude that there was no significant temperature depression above the umbra (Strong et al 1984) or that there was a temperature enhancement above this region in their target sunspots(Lang and Willson). This issue, then, has not been completely resolved. To date no radio spectral analysis has been performed towards solving this question.

This thesis presents the results of combining high-fidelity maps at the few, widely-spaced frequencies observed by the VLA with maps providing the high-spectral resolution capabilities of OVSA. The VLA's 27 antennas have a more complete sky coverage than the OVSA's 7 elements, while the multitude of closely spaced frequencies covered by this later instrument more completely reveal the variations in frequency of the spectra. Stacking the maps in frequency allows us to explore the spectra at various lines of sight. The advantage of this approach is that the VLA provides additional spectral points as well as consistency checks for the OVSA data. The latter allows us to study the variations in frequency in greater detail.

The thesis is structured in the following manner. In the rest of Chapter 1 the results of previous radio studies of active region structure and the theory applicable to the interpretation of radio observations is discussed. The concepts of interferometry and self-calibration are presented in Chapter 2 in order to discuss critical improvements made to OVSA mapping algorithms. Chapter 3 describes the target AR and the observations available for the analysis. This chapter also describes the spectral analysis and model fitting implemented on the radio data and the physical maps that result. Next there is a discussion, in Chapter 4, of the implications of these results as they pertain to the observed emission, resulting in conjectures for the AR structure. Chapter 5 lays out a method for using the spectral model fits to determine the three-dimensional spatial distribution of temperatures from the base

of the corona through the transition region, down to the chromosphere. Finally, in Chapter 6 the overall results are summarized and frameworks for future studies are put forward.

1.2 Spectral Analysis Tools for Solar Observations

A review is warranted on how the physical parameters of electron temperature (T_e), column emission measure (EM), and total magnetic field strength ($B_{\rm tot}$) are obtained from analysis of radio spectra. The general results relevant to this work are discussed and the interested reader is referred to the thorough review by Gary & Hurford (2004) and references therein for greater details. Free-free radio emission arises from distant Coulomb interactions between free electrons and ions in the coronal plasma. Gyroresonance emission is a plasma resonance mechanism due to the gyration of electrons around magnetic fields. Because the mechanisms differ in the manner in which they emit, their spectra are different and easily identifiable.

Irrespective of emission mechanism, the solution to the radiative transfer equation for an isolated, homogeneous source (Dulk, 1985) is

$$T_b \approx T_e(1 - e^{-\tau}) \tag{1.1}$$

T_b is the brightness temperature, essentially the surface brightness of an equivalently hot black body, in units of temperature. It is the effective temperature of the emitting body, equal to T_e when the source is optically thick. The optical depth τ is a measure of the opacity, the dimensionless line of sight integral over the absorption coefficient, and includes most of the physics in the equation. When $\tau \gg 1$, $T_b = T_e$ and the source is optically thick. When $\tau \ll 1$ then $T_b = \tau T_e$ and the source is optically thin. The two regions for a typical spectrum are marked in Figure 1.1a, which is a modified version of figure 4 from Gary & Hurford (1994). It is clear that T_e can be read directly from the optically thick (flat) portion of the spectrum. The two

regimes are separated by the condition $\tau = 1$ and it is at this circumstance that the other physical parameters can be obtained.

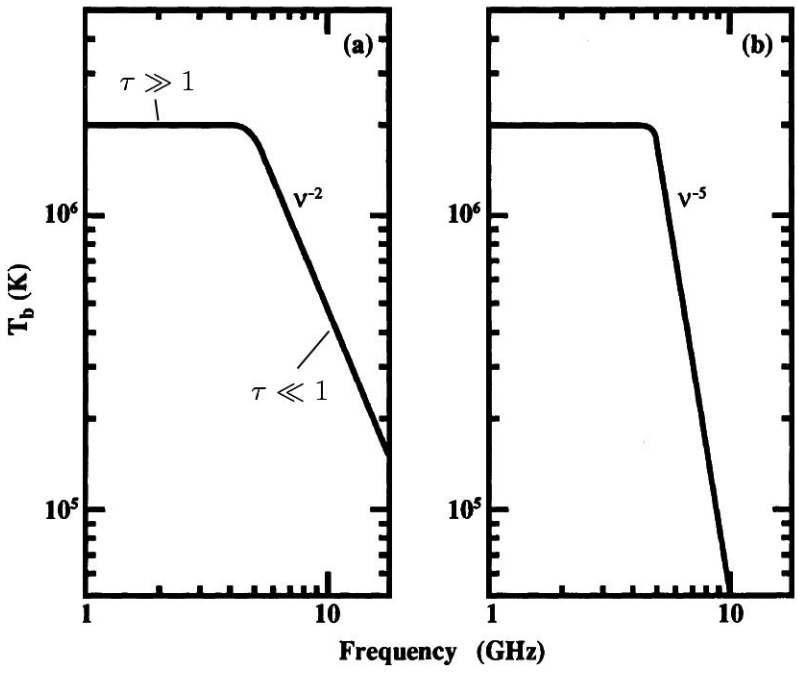

Figure 1.1 Expected T_b spectra for a homogeneous corona: (a) free-free spectrum with the optically thick and thin regimes labeled, and (b) gyroresonance spectrum with a representative high-frequency slope of ν^{-5}, which may theoretically be as steep as ν^{-10} (adapted from Gary & Hurford 1994).

The optical depth for free-free emission from plasma under typical coronal conditions is given by (Dulk, 1985)

$$\tau \approx 0.21 \nu^{-2} T_e^{-3/2} \int n_e^2 dl \tag{1.2}$$

where n_e is the electron density, ν is the observing frequency, and the integral is taken along the line of sight. The optical depth is proportional to ν^{-2}, which makes the optically thin T_b slope easily identifiable. When $\tau = 1$ the above equation can be rearranged to give

$$\int n_e^2 dl = 4.8 \nu_{\tau=1}^2 T_e^{3/2} \mathrm{cm}^{-5} = EM \tag{1.3}$$

where EM is the column emission measure. The value of $\nu_{\tau=1}$ is also read directly from the spectrum.

Gyroresonance emission is a resonance phenomenon whose optical depth depends on n_e, T_e, ν, the magnetic field strength, gradient, and orientation. While the optical depth along the line of sight is rather sensitive to the angle between the magnetic field and the line of sight, the main condition for the resonance is that $\nu \approx s\nu_B$, where $\nu_B = 2.8 \times 10^6 B_{\rm tot}$. Here ν_B is the electron gyrofrequency and s is the harmonic number, an integer. The variation of $B_{\rm tot}$ and T_e along the line of sight produces a spectrum like the one shown in Fig. 1.1*b*. At sufficiently high frequencies, the magnetic fields required to match the resonance condition are no longer in the corona and the brightness temperature begins to drop rapidly to chromospheric temperatures. The frequency at which the spectrum begins to fall comes from the last optically thick harmonic layer still at coronal temperatures. The frequency just above the break in the spectrum, then, provides information about the highest coronal magnetic field strength along the line of sight. Because of the similarity in shape of the spectra in Figs. 1.1*a*, *b*, the spectrum can be described by equation (1.1). In this case, τ should be understood as merely a model parameter and should not be interpreted as optical depth. For mathematical definiteness, the point where equation (1.1) becomes $T_b = T_e(1 - e^{-1})$ is chosen to define the turnover frequency $\nu_{\tau=1}$, just above the break, where $\tau_{model} = 1$. Now the magnetic field at the base of the corona can be defined through a variant of the resonance condition equation

$$B_{\rm tot} = \frac{\nu_{\tau=1}}{2.8 \times 10^6 s} \tag{1.4}$$

As with the free-free spectrum, this $\nu_{\tau=1}$ can be read directly from the spectrum. In magnetized plasma, the emission is broken down into two plasma wave modes, which can be observed as opposite circular polarizations. A discussion of the modes and the expected harmonics will be presented in section 2.3, but in general $s = 2$ for *ordinary* (o) mode and $s = 2$ or 3 for *extraordinary* (x) mode. The high frequency

slope has a dependence of ν^{-5} to ν^{-10}, but variations in temperature and density will keep the slope shallower than the maximum (Gary & Hurford, 1994).

The results of previous studies relevant to spectral analysis of radio observations of the Sun are 1) low frequency sources emit via the free-free mechanism and coincide with the tops of long active region loops, 2) mid to high frequency sources emit via the gyroresonance mechanism, which is closely associated with high magnetic field strengths which in turn implies that they occupy low heights in the solar atmosphere, 3) there is evidence that free-free sources lie above gyroresonance layers in some active regions, 4)some microwave spectra are not fit well with homogeneous temperature models, with evidence that gyroresonance emission may explain the spectral shape from mid to high frequencies, and 5) the umbral and penumbral regions, along with their corresponding magnetic field lines, are distinct environments differing in temperature and associated emissions. With the spectral analysis tools presented in section 1.2, this evidence will afford the framework on which to spatially separate the various layers of the solar atmosphere. Before such a study is undertaken, however, the radio data must be optimized to ensure that the results reflect reality as faithfully as possible.

CHAPTER 2

INTERFEROMETRY AND SELF-CALIBRATION AT OVSA

The science results presented later in this thesis were possible in great part because of improvements to the imaging algorithms used on OVSA data. Although modifications were made to the existing CLEAN deconvolution algorithm, it was the implementation of a self-calibration method that made possible the type of spectral analysis applied. In order to discuss these improvements it is necessary to review the basics of interferometry and self-calibration and their implementation at OVSA. The following summaries of the mature theories of radio interferometry, imaging, deconvolution, and self-calibration draw heavily from the comprehensive descriptions in Pearson & Readhead (1984), Thompson (1999), Briggs (1999), Cornwell et al. (1999), and Cornwell & Fomalont (1999). The reader is referred to these papers for complete details about these theories.

2.1 Interferometry and Image Reconstruction at OVSA

An interferometer correlates the signals received from two antennas observing the same portion of the sky. This measurement, known as the complex visibility, is a Fourier component of the sky brightness distribution. By taking the sum of the complex visibilities from the various baselines available from an array of antennas, an estimate of the sky brightness is made by use of the inverse Fourier transform. This inversion produces what is called the dirty map, which is the true sky brightness convolved with the interferometer's point-spread-function, also known as the dirty beam. The point spread function is the Fourier transform of the interferometer's normalized complex visibility pattern and therefore contains Fourier sidelobes. Because it is a Fourier sum, the sidelobe levels are greater for arrays with a reduced number of elements, such as the OVSA with 7 elements. An observatory with many elements, such as the VLA with 27 antennas, has a more complete sky coverage,

sampling most interesting solar sources adequately, and is therefore less affected by this type of sidelobe. The VLA mapping routines, in addition, use a well-tested data weighting scheme that can minimize its sidelobes or increase the dynamic range as desired. Images from the VLA can therefore also serve as fidelity tests of OVSA maps.

For any interferometer array, it is desirable to remove the effects of the dirty beam as much as possible. This process is known as deconvolution, the result of which is an improved estimate of the true sky brightness. At the OVSA, the Högbom method of deconvolution, CLEAN, is used to produce a map of the sky intensity. This is then converted to a T_b map to aid in the physical interpretation of the data and facilitate comparison with data from other instruments. The existing CLEAN algorithm was modified to properly take into account the area of the synthesized beam, a correction amounting to a factor of $4 \times \ln(2)$ (Bastian 2008, private communication). The effect of this change is that the brightness temperatures reported in the self-calibrated OVSA maps is raised, bringing it closer to the values reported in the VLA maps. In order to make use of the Fast Fourier Transform algorithms available the visibility data must be interpolated onto a rectangular grid. The normalization scheme for the gridding interpolation scheme at OVSA was also modified to complete the steps towards approximating a non-discrete integral convolution (Briggs et al, 1999). The convolving gaussian is now normalized by its integral and the effect of the convolution is taken into account by dividing the maps by the Fourier Transform of this normalized gaussian. This modification addresses the tapering in the image introduced by using such a convolution in the Fourier plane.

It is common practice to use a CLEAN box to select and restrict the region over which the CLEAN loop acts on the dirty map. This reduces the number of degrees of freedom when performing a deconvolution. The CLEAN box, usually a rectangle of variable size, must include the entire source. In order to maximize the

number of independent constraints to the number of degrees of freedom available to the deconvolution process, the CLEAN boxes should be placed as tightly around the source as possible (Pearson & Readhead 1984). Towards this goal, the ROI (region of interest) routine in the Interactive Data Language (IDL) was used to allow the user to trace out any shape for use as a CLEAN box. The benefit of using such a CLEAN box is that, after some tests to infer the position, shape, and extent of the source within the dirty map, the CLEAN algorithm can be made to act only on the source. This is particularly important for the formation of the CLEAN map without residuals for use as a model in self-calibration. The tests to determine source size and shape include frequency synthesis mapping where the number of frequencies bracketing the target one is iteratively reduced, combined with a minimization of side-lobe response through a variation in the size and shape of the CLEAN ROI. Experimentally it was found that the modified CLEAN routines exhibit a reduced rms noise, the square-root of the variance in a patch of the image away from the source, relative to maps produced with the unmodified programs.

2.2 Implementation of L_1 Self-Calibration at OVSA

The correlated signal output of a real interferometer is the complex visibility degraded by a complex gain factor arising from amplitude and phase errors from the instrument and signal variations in transit through Earth's upper and lower atmosphere (Pearson & Readhead 1984; Cornwell and Fomalont 1999):

$$\tilde{V}_{mn} = g_m e^{i\theta_m} g_n e^{-i\theta_n} \; \hat{V}_{mn} \; + \; \varepsilon_{mn} \tag{2.1}$$

where $\tilde{V}_{mn}$ and $\hat{V}_{mn}$ are the observed and true sky visibilities from the m-n baseline, respectively, ε_{mn} is a zero-mean, thermal noise term, and the multiplication of the antenna gains $g_m e^{i\theta_m}$ and the complex conjugate of $g_n e^{i\theta_n}$ is the complex gain factor. Here θ_m and θ_n are the phase errors from antennas m and n, respectively. If a strong

calibration source is located near the observation target throughout the observing day, observations of it can be used to deduce the element gains as a function of time and these corrections then aid in bringing $\tilde{V}_{mn}$ and $\hat{V}_{mn}$ into agreement. However, this calibration is incomplete in that it is difficult to always have a strong, point-source calibrator near the target and the interpolation into phase corrections appropriate to the time and position of the target may not be appropriate. Most importantly, rapid variations such as those imposed by the propagation of the sky signal through the Earth's troposphere and ionosphere cannot be accounted for by such methods and some errors remain. These remaining errors can be addressed through self-calibration.

The basic principle of self-calibration is that an interferometer array provides more independent measurements than there are errors and this allows the treatment of element gains as free parameters. If all elements are correlated, an array of N elements has $\frac{1}{2}N(N-1)$ independent baselines, meaning it obtains that many complex visibility measurements. Taking into account that all phases are referenced to one of the elements, if every antenna has a complex gain error, there are $\frac{1}{2}N(N-1)-(N-1)$ "good" phase measurements and $\frac{1}{2}N(N-1)-N$ "good" amplitude measurements (Cornwell & Fomalont 1999). One way to exploit the abundance of information is to solve for the antenna gains directly by minimizing the difference between the left and right hand sides of equation 2.1, each time producing a better model of the sky intensity distribution from which a new $\hat{V}_{mn}$ is formed. Two methods have been well developed: minimizing the sum of the absolute values of the difference between the measured and true visibilities, the L_1 norm, or the sum of their squares, the L_2 norm. Treating each time interval idependently, the L_1 norm minimizes (Schwab 1982)

$$S_\epsilon(\theta) = \sum_{m<n} \omega_{mn}[|\tilde{V}_{mn} - e^{i(\theta_m-\theta_n)}\hat{V}_{mn}|^2 + \epsilon]^{1/2}. \tag{2.2}$$

where ω_{mn} are weights, whose proportions are determined from the inverse of the noise on the m-n baseline, ε_{mn}. The model sky visibilities $\hat{V}_{mn}$ are provided by

a CLEAN map, the gains are adjusted to minimize $S_\epsilon(\theta)$, and the resulting gains are used to correct the observed visibilities in order to produce a new, improved model. The process is repeated with the improved models from every iteration until the phase solution converges. Solutions are then calculated for a range of ϵ and extrapolated to $\epsilon = 0$ to arrive at the final solution for the gains. Schwab (1982) showed that, while both methods perform nearly equally well, the L_1 norm is less sensitive to outliers in the data. Outliers are points quite offset from their true visibilities due to temporary errors in the electronics or from changes to the signal phase incurred in transit. Although the most obvious errors may be flagged out of the data, some may remain, specially when the deviation from the norm may not be much larger, visually, than the average random errors in the data, making this method seem more appropriate to an interferometer with a relatively high noise level, such as the OVSA. The method is well developed by Schwab (1982) and the full set of equations will not be re-written here. It was verified, as Schwab (1982) found, that the algorithm converges rather quickly for a given ϵ. Tests on OVSA data showed that these solutions did not change significantly with changing ϵ within the range used by Schwab (1982), making an interpolation to $\epsilon = 0$ unnecessary. In addition, an amplitude and phase self-calibration run was found to actually degrade the map from the improvements made by phase only self-calibration runs. Hence the final programs include solutions for one low value of ϵ (0.5) and perform two consecutive phase only self-calibration runs. The programs and techniques developed to implement this method on OVSA data are now part of the OVSA software tree of the Solar SoftWare (SSW) package, written in IDL and in common use by the Solar Physics community. There are a few caveats to be discussed pertaining to self-calibration with an array such as the OVSA.

The issue of possible non-unique solutions from self-calibration for arrays with a low number of elements (Cornwell & Fomalont 1999) was found not to be a problem

at all. That is, for a given set of complex visibilities, application of the self-calibration algorithms created for this work return maps with consistent source structure and amplitude even with some variation of initial conditions, such as CLEAN box shape and size, and number of CLEAN components used to create the input model map. In the CLEAN algorithm, the source is decomposed according to the interferometer's response function and then restored into a number of CLEAN, gaussian components. The consistency of solutions can be seen in Figure 2.1, which displays the source centered one-dimensional profiles from self-calibrated maps made with a data set purposefully containing known bad data. Panel *a* shows the effects of changing the number of CLEAN components, or number of CLEAN iterations, used to make the initial model to begin the self-calibration. Only the lowest number of clean components shows a slight increase in one of the side lobes. Panel *b* shows the effect of changing the size and shape of the CLEAN ROI, previously a CLEAN box. The solid line is from an ROI tightly drawn around the brightest source, possibly excluding some more diffuse emission, the dotted line is from an ROI covering the source as well as an obvious, strong side lobe, and the dashed line is from an ROI covering a large area around the bright source, excluding the strong side lobe. Clearly, only minor changes in structure and amplitude occur, the worst side lobe response coming from the ROI encompassing the strong artifact in the data. This demonstrates the benefit of using the ROI function to select a CLEAN box, insted of a rigid square, since spurious sources might be difficult to exclude if one was restricted to a rectangle. This also shows that the programs are somewhat more user friendly, since precise knowledge of the source shape within the dirty map are not needed to produce good maps. The best maps are produced with a moderate number of CLEAN components and ROI for the initial model. In general, however, self-calibration does improve with an increasing number of antennas, since the ratio of visibility constraints to unknown complex gains is $\frac{N-2}{2}$ for phases and $\frac{N(N-3)}{2(N-1)}$ for amplitudes (Cornwell & Fomalont

1999). Because of persistent problems with one of OVSA's antennas, only 6 antennas were available, rendering these quantities in ratio of 2:1 and 9:5, respectively . Not only is this a smaller ratio of information to unknowns than from, say, the VLA's 27 antennas, but the poor sky coverage from so few elements presents a greater chance of producing model errors that can be frozen into the data and propagated through the self-calibration process (Cornwell & Fomalont 1999). The constraint of positivity on the T_b map was imposed to address this issue, but some defects in the maps may persist.

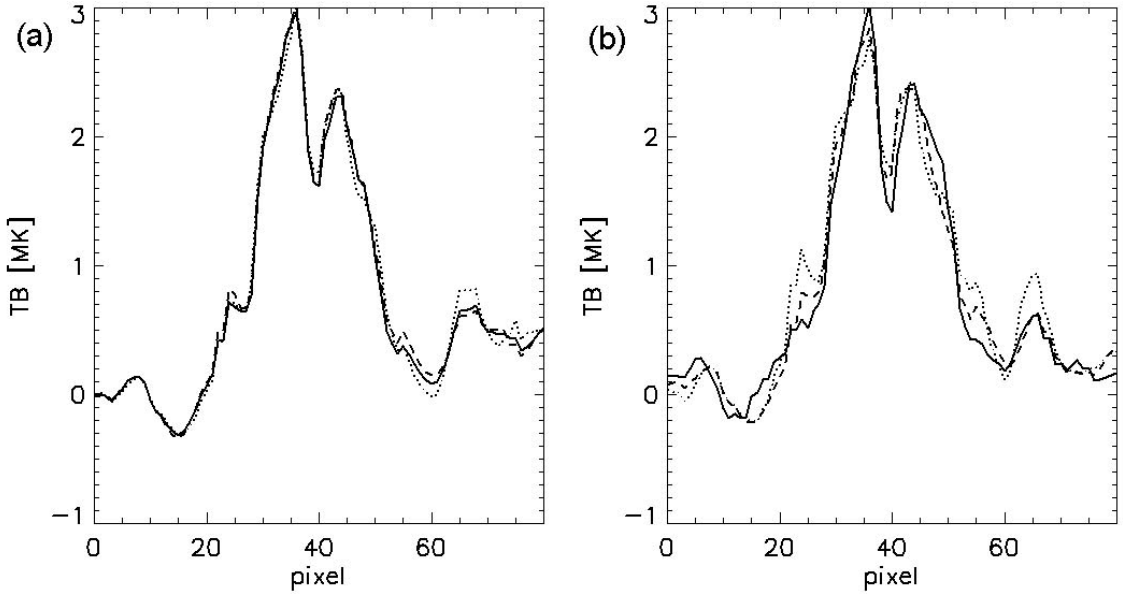

Figure 2.1 Tests of convergence and non-uniqueness of solution from self-calibration (a) varying the number of CLEAN components used to create the initial model: 1000 (solid), 200 (dotted), 3000 (dashed), and (b) varying the size and shape and size of the CLEAN ROI, tightly surrounding the brightest source (solid), encompassing the source and an obviously strong sidelobe (dotted), and an arbitrarily large CLEAN ROI excluding the strong sidelobe (dashed).

Despite having so few elements, the self-calibration of OVSA data results in either slightly modified or visibly smoothed temporal phase variations and, most importantly, a consistent improvement in the fidelity of the resulting T_b maps. The resulting self-calibrated, monochromatic maps not only exhibit lower noise than with

a CLEAN-only approach but also produce smoother spectra when stacked in frequency, as seen in Figure 2.2. In the plot in this figure, the near-match of the self-calibrated Stokes I OVSA (+) to VLA (**X**) brightness temperatures is obvious. The improved continuity across maps made at individual frequencies further attests that the algorithms correctly implement the self-calibration method and lend a critical level of confidence to the spectral analysis described in Chapter 3. All the resulting OVSA Stokes I maps yield good agreement in brightness temperature and general structure with their corresponding VLA maps, as will be shown later in this section and in Chapter 3. While the strong source at the center of the 4.8 GHz map is little affected by the self-calibration, the sidelobe level elsewhere in the map is reduced. This enables spectral analysis over a region wider than the strong, sunspot-associated source. The importance of this should not be minimized: accurate mapping of the entire active region's corona is crucial to arriving at the conclusions presented later in this thesis. The greatest rms noise in the self-calibrated maps is 4-5% of the peak values, as compared to 9-10% in the best new CLEAN maps and 14-15% from the unmodified CLEAN routines.

Figures 2.3 to 2.6 show the calibrated and self-calibrated baseline phases vs time at 1.4 and 4.8 GHz. Two frequencies are shown to demonstrate consistency in the method, despite the algorithm operating on data from a single frequency per run. When looking at these plots, it must be kept in mind that phases wrap around the range of $-\pi$ to π, causing some of the phase behavior to *appear* convoluted. The self-calibration algorithm also operates on the visibilities across the baselines for a single time value, meaning that no information is passed along in time. Some baselines exhibit an obviously improved smoothness of phase vs time, such as baselines 1-5, and 1-7. These baselines are the shortest in the array, and may not show much structure because they sample the sky with a low angular resolution. The more complex phase structure preserved in much longer baselines, such as 1-2, 1-6, and 2-6 presumably

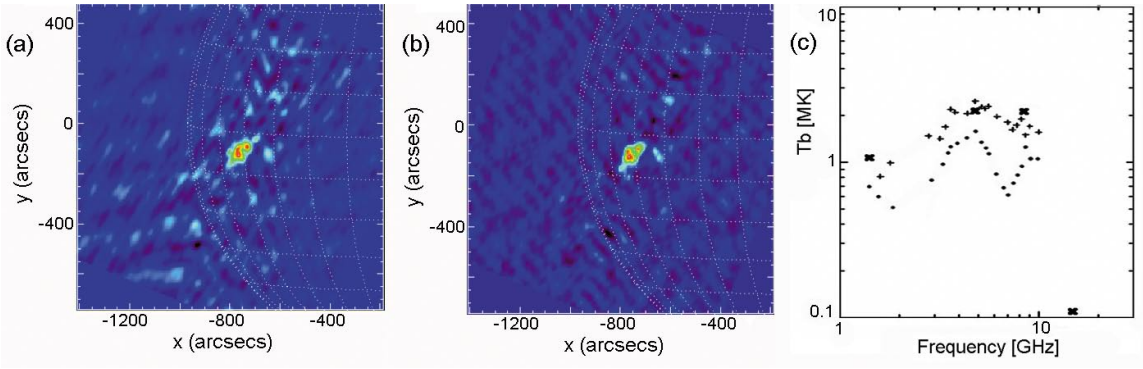

Figure 2.2 (a) OVSA 4.8 GHz map CLEANed with the revised algorithms. At this stage the T_b levels already match those of the VLA C-band map, (b) Same image after self-calibration. The noise in the maps is reduced while maintaining the structure of the strongest source. (c) Improved spectra from ($-760''$, $-110''$), near the T_b peak. The dots represent values from CLEAN maps using the previous versions of the programs, the pluses are the corresponding data points from the self-calibrated maps, and the thick Xs are the VLA data points. Note the amplitude match between both instruments and the improvement in spectral continuity between 5-10 GHz.

represent real variations in phase due to changing source structure resolved by these baselines. In no case does the phase self-calibration further degrade the baseline phases from the input values. The self-calibration algorithm has one limitation: a single baseline's visibilities cannot be eliminated from the data set. If any antenna's data shows a baseline that is corrupt, the entire data from that antenna must be removed before proceeding. This does not present a severe limitation, as will now be shown.

The inclusion of baseline 4-5, in particular, caused severe banding in the CLEAN map (Figure 2.7a) which was remedied by its exclusion from the data set (Figure 2.7b). As a test of the self-calibration algorithm, this baseline was included to see if sufficient phase corrections could be attained. The calibrated and self-calibrated phases for this baseline are shown in Figure 2.8. The resulting self-calibrated map shows that some banding remains (Figure 2.7c). T_b plots across the source and across the banding, away from the source, show that the map produced through self-

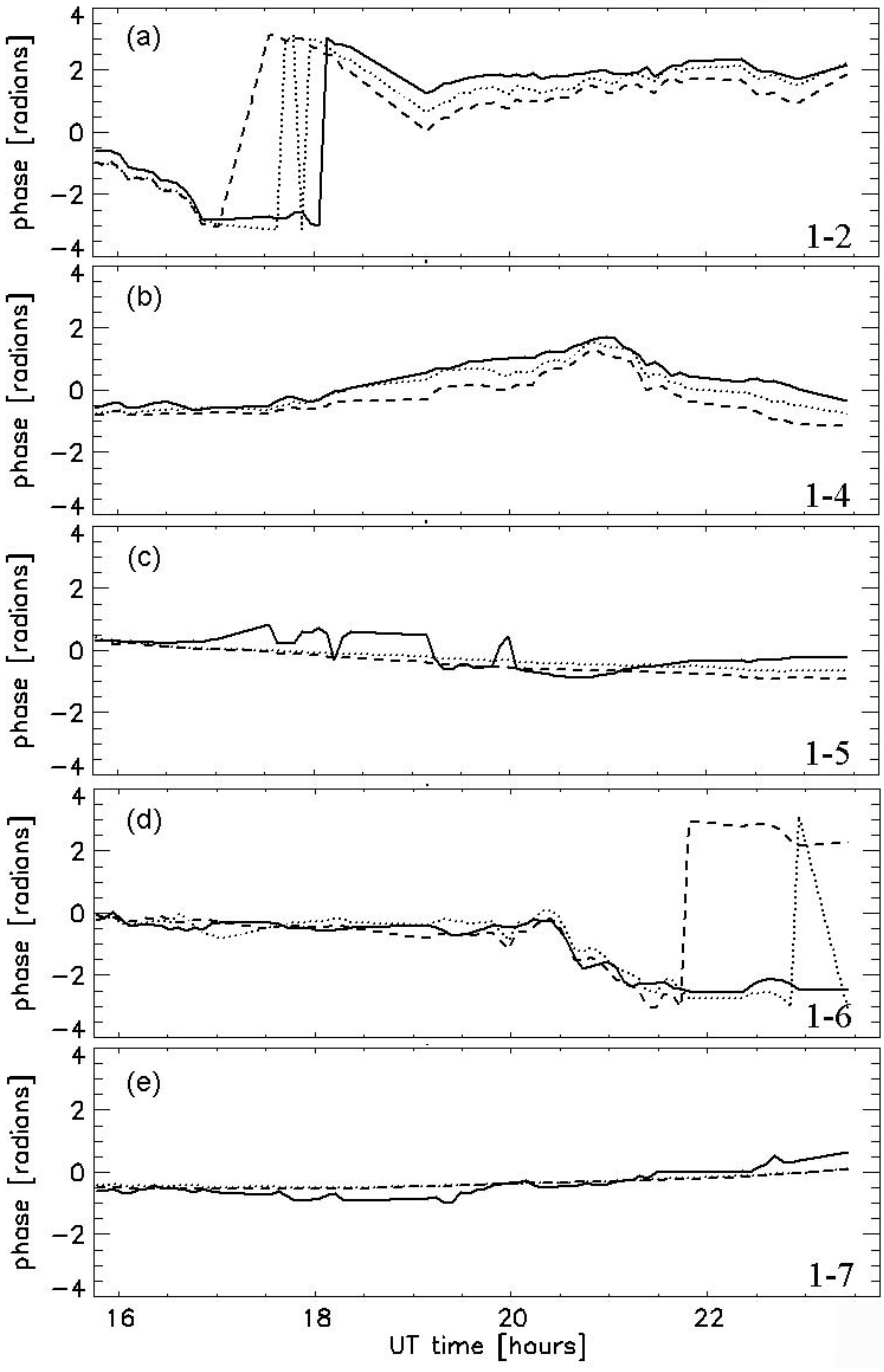

Figure 2.3 Baseline phases vs time during November 10, 2006 observed with OVSA at 1.4 GHz. Shown are the calibrated visibilities (solid), first (dotted) and second (dashed) phase self-calibration runs for (a)the 1-2 baseline, (b) 1-4, (c) 1-5, (d) 1-6, and (e) 1-7.

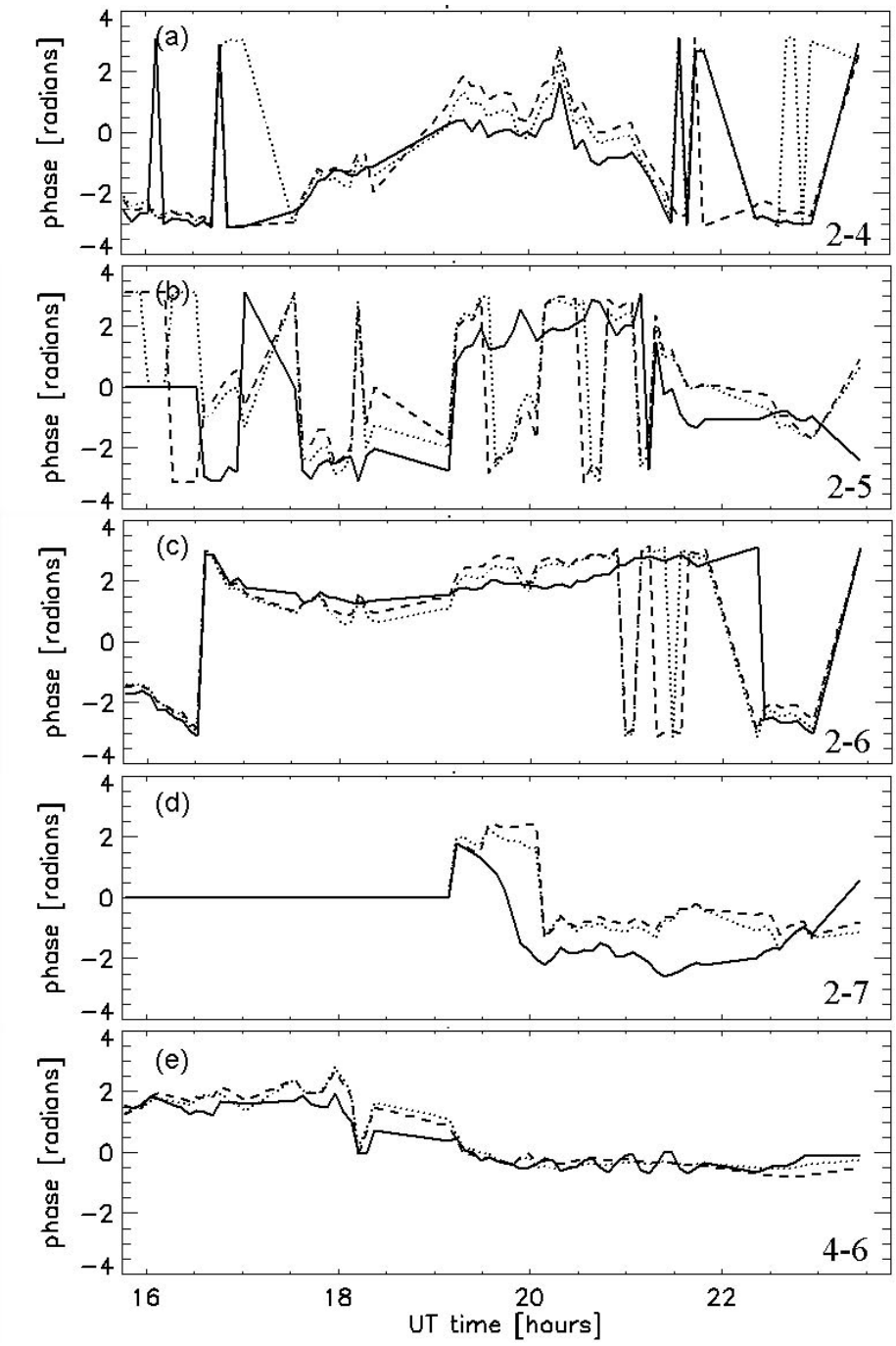

Figure 2.4 Continued display of baseline phases vs time during November 10, 2006 observed with OVSA at 1.4 GHz. Shown are the calibrated visibilities (solid), first (dotted) and second (dashed) phase self-calibration runs for (a)the 2-4 baseline, (b) 2-5, (c) 2-6, (d) 2-7, and (e) 4-6.

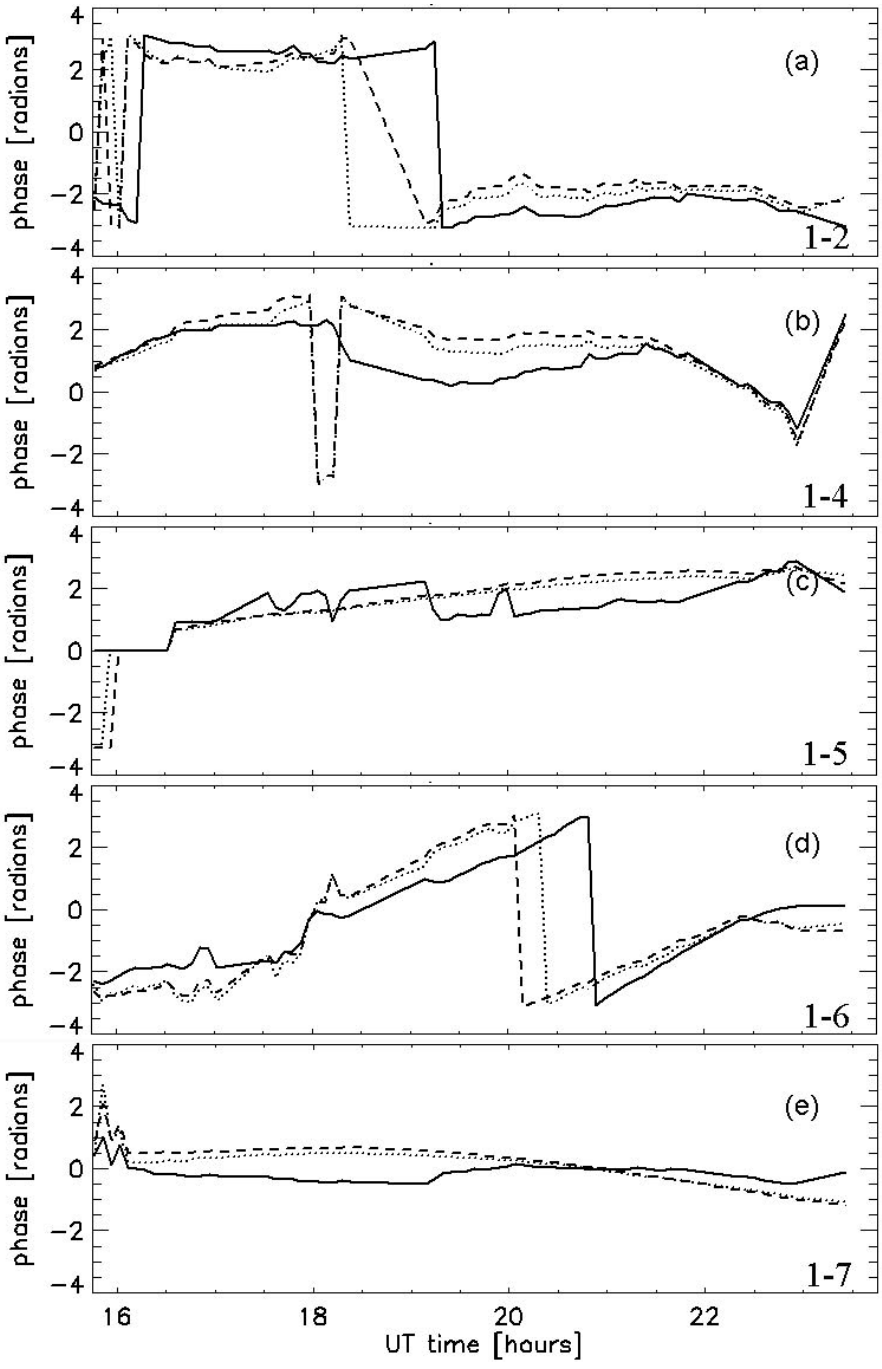

Figure 2.5 Baseline phases vs time during November 10, 2006 observed with OVSA at 4.8 GHz. Shown are the calibrated visibilities (solid), first (dotted) and second (dashed) phase self-calibration runs for (a)the 1-2 baseline, (b) 1-4, (c) 1-5, (d) 1-6, and (e) 1-7.

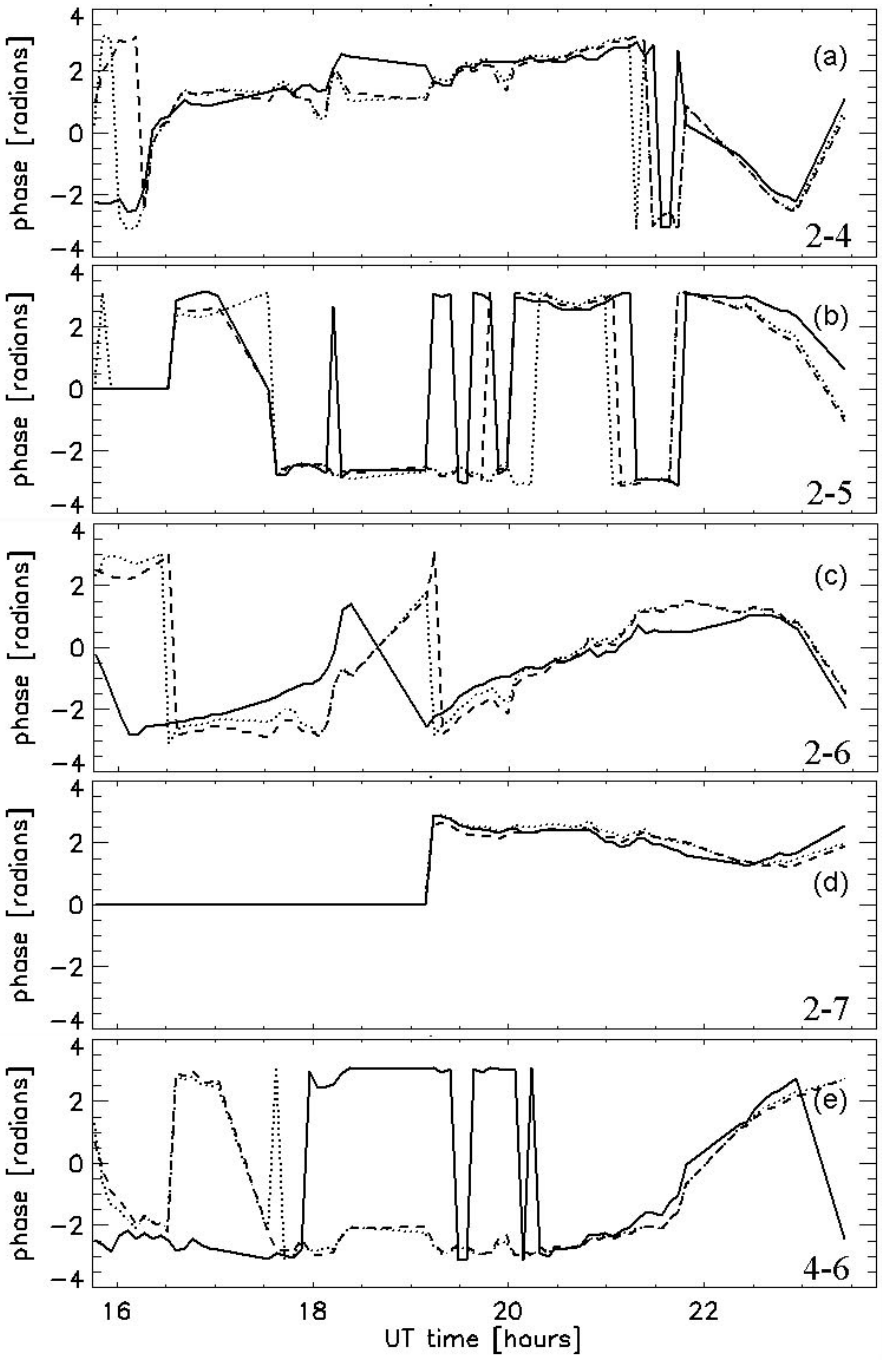

Figure 2.6 Continued display of baseline phases vs time during November 10, 2006 observed with OVSA at 4.8 GHz. Shown are the calibrated visibilities (solid), first (dotted) and second (dashed) phase self-calibration runs for (a)the 2-4 baseline, (b) 2-5, (c) 2-6, (d) 2-7, and (e) 4-6.

calibration with baseline 4-5 matches the CLEAN map made without it very well across the source, and that their noise level across the bands nearly matches, although the periodicity of the banding remains (Figure 2.9). Ultimately, the banding effect is removed and the noise level is reduced further by the removal of visibility data from the 4-5 baseline after the self-calibration runs.

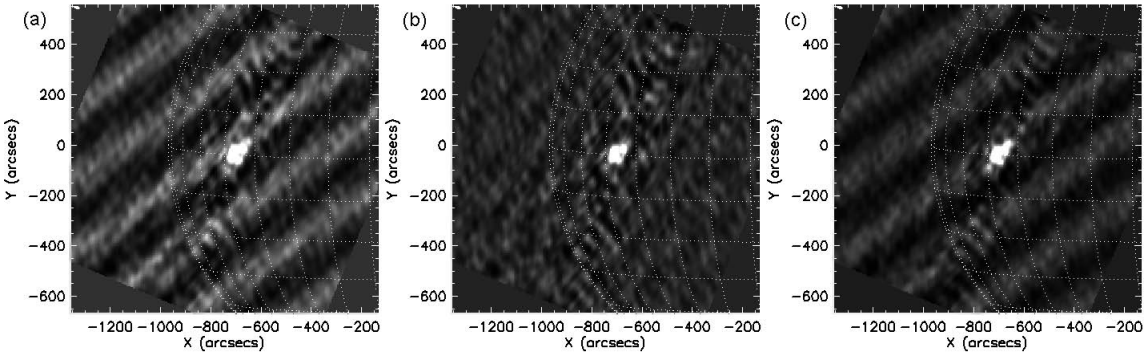

Figure 2.7 Tb maps made (a) with baseline 4-5, using the CLEAN method, (b) without baseline 4-5, using the CLEAN method, and (c) with baseline 4-5 using self-calibration. The high contrast and grey scale have been chosen to accentuate the banding, resulting in saturation of the main source.

As previously mentioned, VLA maps can serve as tests for OVSA maps at nearby frequencies. In this data set, these frequencies are 1.4, 4.8, and 8.2 GHz from the OVSA to 1.41, 4.84, and 8.48 from the VLA. Figure 2.10 shows the CLEAN and self-calibrated T_b profiles compared to the VLA's. The pixel resolutions at 1.4, 4.8, and 8.2 GHz are 16.4, 4.8, and 2.8″per pixel, so the source at low frequencies is much more spatially extended, relative to the higher ones, than is apparent when plotted agains pixel number. At 1.4 GHz, the improvement is striking. While the CLEAN method severely overestimates the brightness temperature in the right-most peak and underestimates that in the left one, the self-calibrated map matches these features well. At 4.8 GHz the CLEAN method underestimates the brightness temperatures, notably in the right-most peak, but self-calibration yields values ~ 0.4 MK closer to the VLA's, although the mark is missed. The missing flux here is

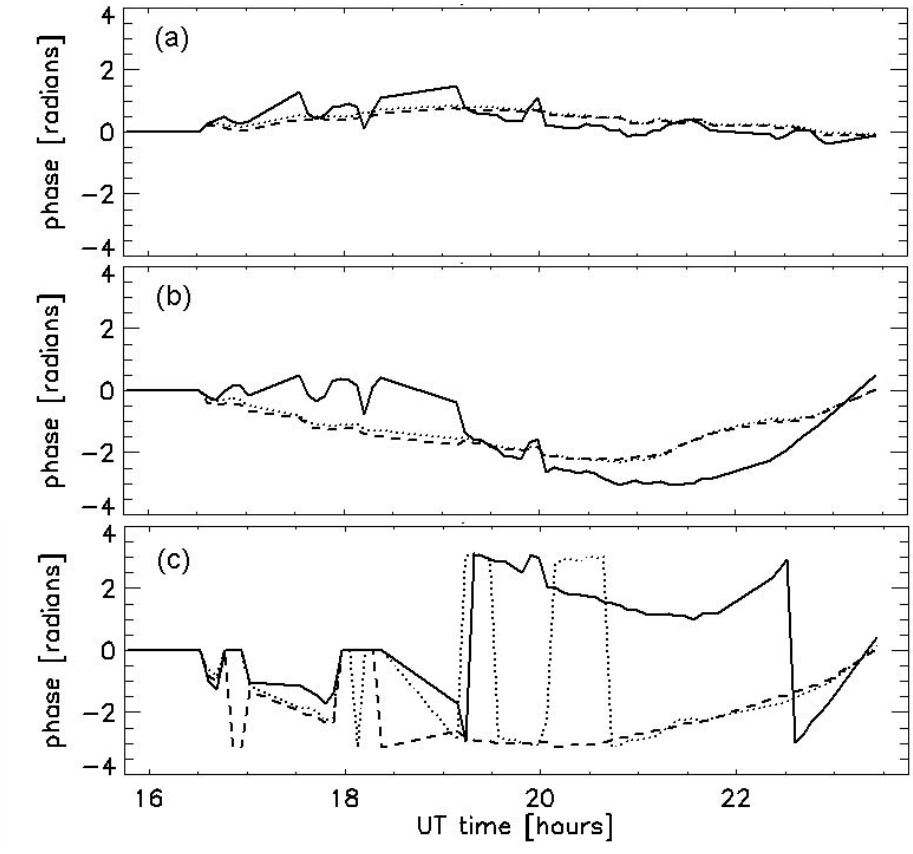

Figure 2.8 Calibrated visibilities (solid), first (dotted) and second (dashed) phase-only self-calibration phase vs time behavior for baseline 4-5 at (a) 1.4 GHz, (b) 4.8 GHz, and (c) 8.2 GHz.

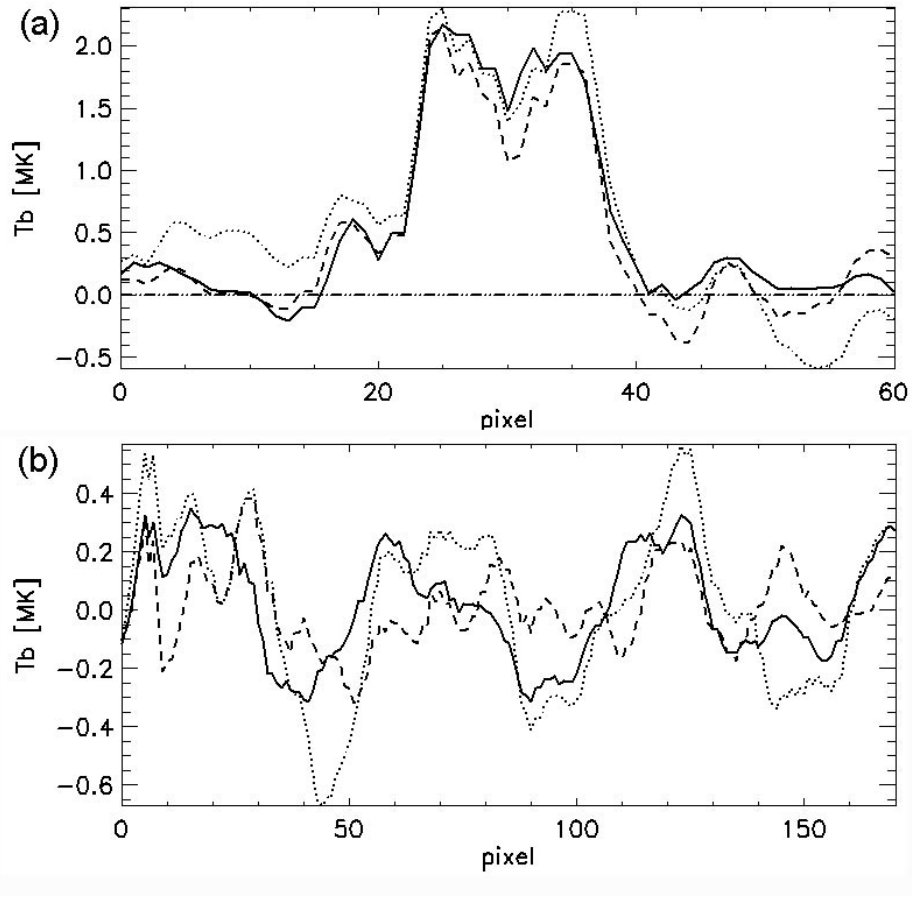

Figure 2.9 1-dimensional T_b profiles from the CLEAN map made with baseline 4-5 (dotted), CLEAN map made without this baseline (dashed), and self-calibrated map made with baseline 4-5 across (a) the two lobes of the main source, and (b) across the banding, away from the source.

probably a result of the complexity of the source and incomplete uv coverage of the OVSA instrument. At 8.2 GHz, the self-calibration peak brightness temperature is $\sim$ 0.8 MK closer to the VLA's than that from the CLEAN map, a substantial improvement. The side lobes close to the source in the self-calibration map at this frequency are more severe than in the CLEAN map. However, the improved source amplitude is worth such increased Fourier "ringing". Maps from the current OVSA cannot be expected to completely match the VLA's because of the low number of baselines available. Despite the reduced sky coverage, the correct execution of the self-calibration method results in an improved amplitude and spatial structure match to the VLA, improved continuity in frequency, and overall reduction in rms noise level away from the sources. These improvements make these images the best single-frequency OVSA maps ever produced.

2.3 Inversion of Total Intensity Spectra

Radio emission from both the free-free and gyroresonance mechanisms leaves the corona in one of two magnetoionic modes, the ordinary mode (o-mode) and the extraordinary mode (x-mode). They are completely circularly polarized when they leave the source, and they correspond generally to either the right (R) and left (L) circular polarizations, depending on the orientation of the magnetic field at the layer height (Gelfreikh, 2004). Polarization observations of free-free emission may be used to determine the longitudinal component of the magnetic field but the degree of polarization from free-free emission is low ($\leq$ 15%). The sidelobe confusion in OVSA images bring the uncertainties up to or above the polarization signal and such a study cannot be carried out with these data. While the VLA samples the sky much more accurately, the reduced number of frequency points limits its use for spectral studies. Furthermore, analysis of the joint polarization spectra reveals that even at higher frequencies, where gyroemission dominates, the frequency separations

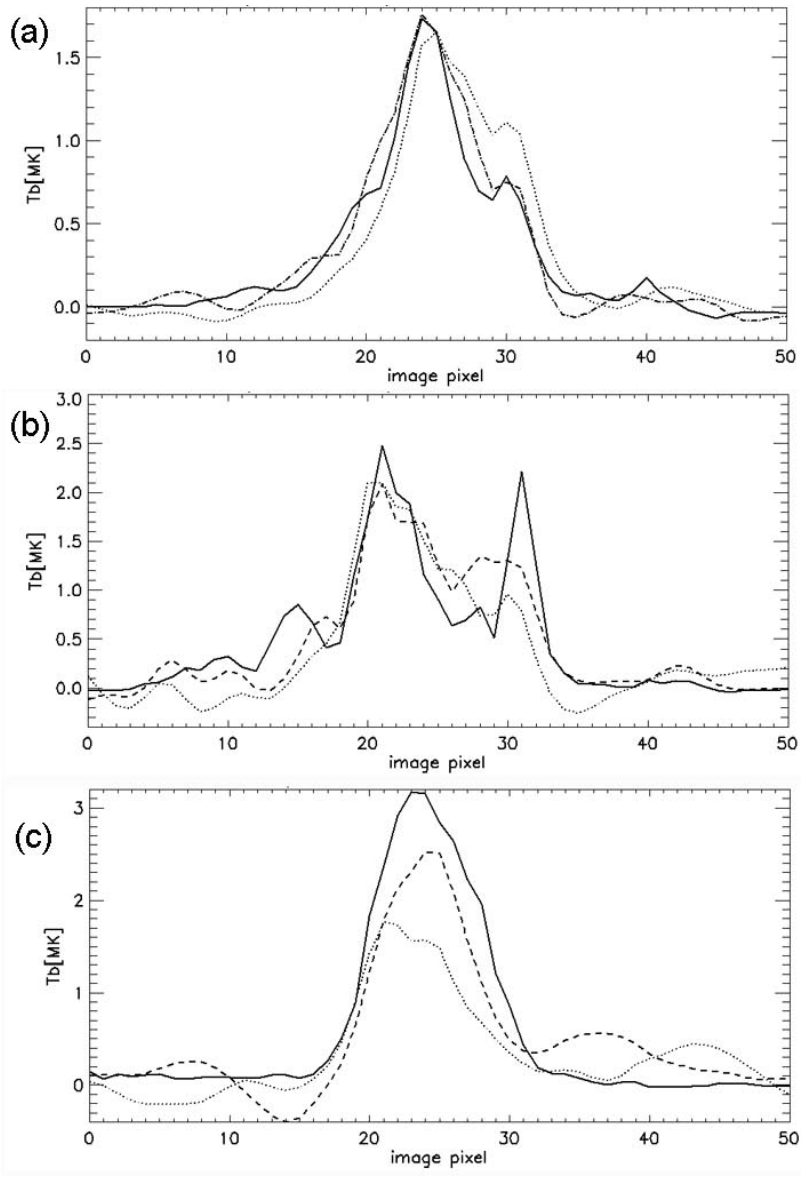

Figure 2.10 1-dimensional T_b profiles across the sources at (a) 1.4, (b) 4.8, and (c) 8.2 GHz. Pixel resolutions at these frequencies are 16.4, 4.8, 2.8 $''$/pixel, respectively. The VLA data (solid) has been convolved to the OVSA resolution and compared to the CLEAN (dotted) and self-calibrated (dash-dot-dot) results.

between the turnovers from both polarizations yield results that, while consistent with respect to the expected outcome, do not usefully constrain it. The analysis is therefore carried out with total intensity (Stokes I) spectra, where $I = (R + L)/2$. Since the harmonic information is embedded in the polarized signal and is lost in the construction of I, such an approach must first be validated.

As was mentioned earlier, the different modes may become optically thin at different harmonics. This means that spectra in individual polarizations may turn over at different frequencies. Zheleznyakov (1970) found that the opacity of x-mode harmonic is an order of unity higher than that for the o-mode except when the angle between the magnetic field and the line of sight is close to 0 or 90 degrees. Figure 2.11 shows such spectra from simulations of observations of a coronal model presented by Mok et al. (2005). The simulation is from a study (Gary & Hurford, 2004) for the proposed Frequency-Agile Solar Radiotelescope (FASR) which would have many elements sampling the sky with a high spectral resolution. For this reason the sample spectra in the figure reflect the direct model's spectra quite well and small details are visible. Here it is sufficient to note the difference in turnover frequencies between the R and L spectra such that their ratio would allow the harmonic number to be determined.

A number of studies have shown that only the lowest harmonics can play a role in the solar corona (Alissandrakis et al., 1980; Felli et al., 1981; Alissandrakis & Kundu, 1982; Zlotnik et al., 1996; White & Kundu, 1997; Vourlidas et al., 1997). In general, $s = 2$ for o-mode and $s = 2$ or 3 for x-mode. Only under very special circumstances the $s = 4$, x-mode layer may become optically thick (Holt & Ramaty, 1969; Zheleznyakov, 1970; Takakura, 1972; Ramaty & Petrosian, 1972; Vourlidas et al., 1997). The $s = 1$ x-mode emission does not propagate out into the corona because that gyroresonance layer lies beneath its own reflecting point (Zlotnik et al., 1996). The o-mode from this harmonic may propagate but opacity calculations made

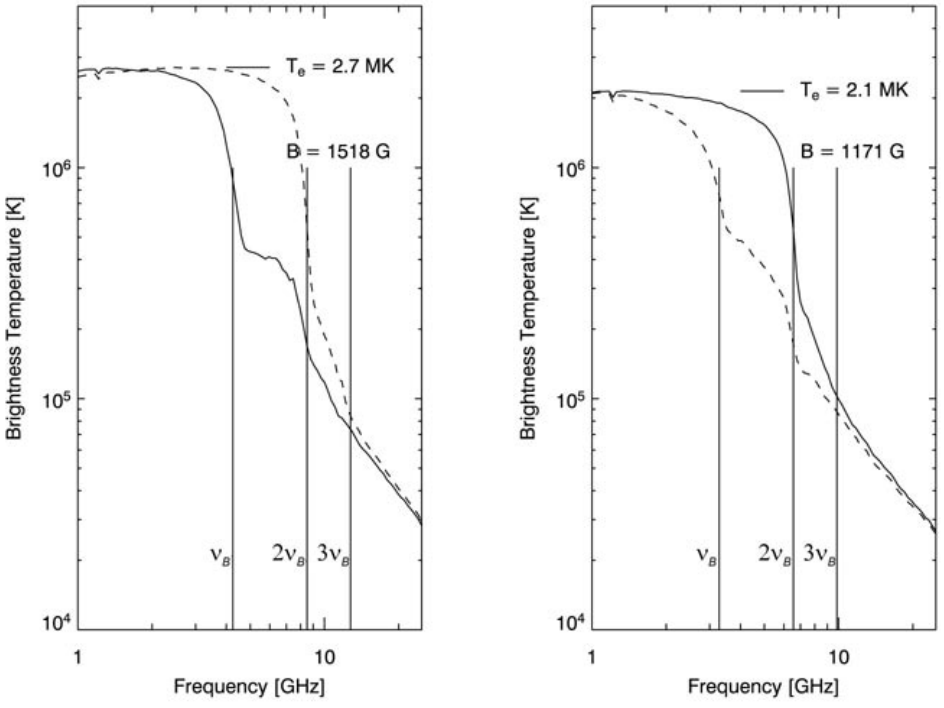

Figure 2.11 T_b spectra for R (solid) and L (dashed) circular polarizations along two different lines of sight in an active region coronal model (Mok et al. 2005). The model was sampled with a FASR-like instrument with excellent sky sampling at 100 frequencies from 1-24 GHz, resulting in exceptional detail. The spectra become optically thin at different harmonics, and the ratios between the drops are used to identify the harmonic number. Source: Gary & Hurford 2004)

with a model sunspot find that even when the $s = 2$ layer above it is optically thin and would allow the emission to go through, the $s = 1$ o-mode is optically thin as well (White, 2004).

Since the turnover frequency is used to determine $B_{\rm tot}$ at the base of the corona, the same model from Mok et al. (2005) is now used to determine the error in magnetic field strength as derived from total I spectra instead of R and L. The ideal model R and L spectra are sampled only at the frequencies available in the joint VLA-OVSA data. Noise is added at a level that mimics the errors introduced by the incomplete sky sampling, here 10% of the value at each frequency. The I spectrum is formed and fitted with a representative spectrum that has a slope of ν^{-5}. The value of $B_{\rm tot}$ is calculated from $\nu_{\tau=1}$, obtained directly from the model fit, considering $s = 2$ and 3. The actual value of $B_{\rm tot}$ and the correct harmonic are obtained from the uncorrupted spectra and the values are compared. Figure 2.12 shows an example spectrum illustrating the steps in this process. It is found that for differences between the 2nd and 3rd or between the 3rd and 4th harmonics, the errors for $B_{\rm tot}$ from the noisy I spectra and the actual value for the polarization spectrum that corresponds to the lower harmonic are 5-15%. The I spectrum follows the fall in T_b at the lower harmonic and becomes steeper once the higher harmonic turns over. The conclusion is that the analysis on I spectra will give $B_{\rm tot}$ values that match those from the lower harmonic within 15%. The problem of determining the proper harmonic from the actual data will be addressed via optical depth calculations using the magnetic field extrapolation.

In conclusion, in this chapter the optimization of the OVSA imaging algorithms has been described, along with the implementation of self-calibration, which produces improved-quality maps that are consistent with the corresponding ones from the VLA. The same level of improvement is expected for intermediate frequencies not measured with the VLA, thus increasing the fidelity of the resulting spectra. The

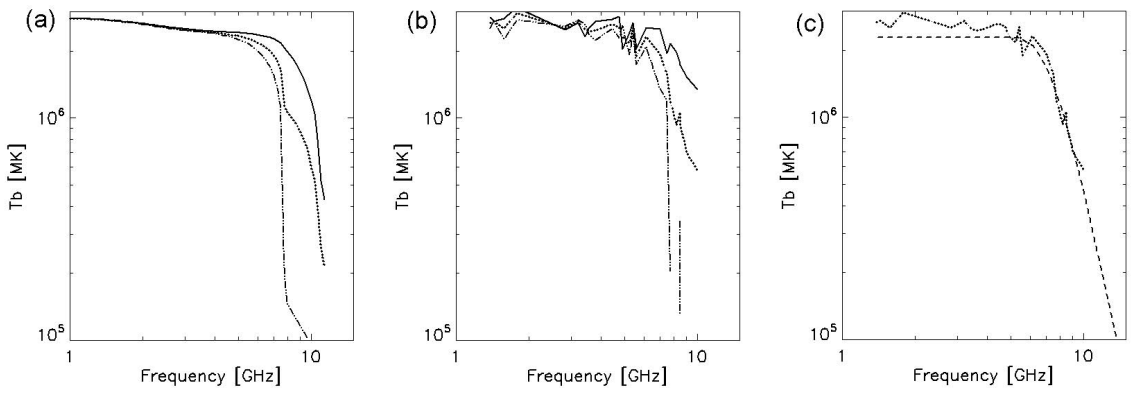

Figure 2.12 Sample steps in the determination of errors in $B_{\rm tot}$ from the use of I spectra: (a) ideal R and L spectra from the model, sampled at the same frequencies of the VLA-OVSA observations and the I spectrum (dotted), (b) same spectra after 10% noise has been added and the new I (dotted), and (c) the noisy R and L spectra with the fit to the I spectrum (dashed). This last panel shows how closely the fit to the I spectrum follows the spectrum from the lower harmonic, in this case s=2. For this spectra $B_{\rm tot}$ from the fit for s=2 is 1445 G while the value from the model is 1378 G, off by $\approx 5\%$.

use of total intensity data has been justified, and the errors in the values of B_{tot} derived from its use are estimated to be within 5-15%. The next chapter provides a description of the entire data set available for this study, an explanation of the models and methods used, and the physical results thus obtained.

CHAPTER 3

ANALYSIS OF THE MULTI-WAVELENGTH DATA SET FOR AR 10923

3.1 Observations and Auxiliary Data

3.1.1 Active Region NOAA 10923

The observations of NOAA active region (AR) 10923 were carried out on 2006 November 10. On this day it was a mature, stable region of alpha configuration located at about $S11$, $E49$. The MDI magnetogram shows that at this time the AR consisted of a single large, fairly undisturbed negative-polarity sunspot surrounded by a scattered plage of opposite polarity fields, some of them extending to distances $\sim$ 100 Mm *East* of the sunspot (Figure 3.1). A minor B1 flare event occurred on this day starting at 22:40 UT, but it did not appear to change the loop structure as determined from X-ray and EUV observations or photospheric magnetic fields as seen in the magnetogram data. The region was stable until a C3 event at 21:55 on November 12 and developed a light bridge on November 13 (Katsukawa et al., 2007). For this observation day, then, the AR is considered stable enough to perform full-day Earth-rotation synthesis with the radio data.

3.1.2 Very Large Array Observations

The VLA is a 27 element astronomical interferometer which provides excellent *uv* coverage at a few frequencies. On this date the VLA observations of AR 10923 were taken by the author from 15:18–22:46 UT. The data were obtained in left- and right-circular polarizations (LCP, RCP) at 1.41, 4.84, 8.48, and 14.96 GHz (L, C, X, and U bands) while the instrument was in "C" configuration (Thompson et al., 1980). The angular resolution was $\sim$23″, 6.6″, 3.7″, and 2.2″at these bands, which along with the instrument's available 351 baselines render it capable of adequately mapping complex structure at each frequency. The data were calibrated using 3C286 and 1543-079 as

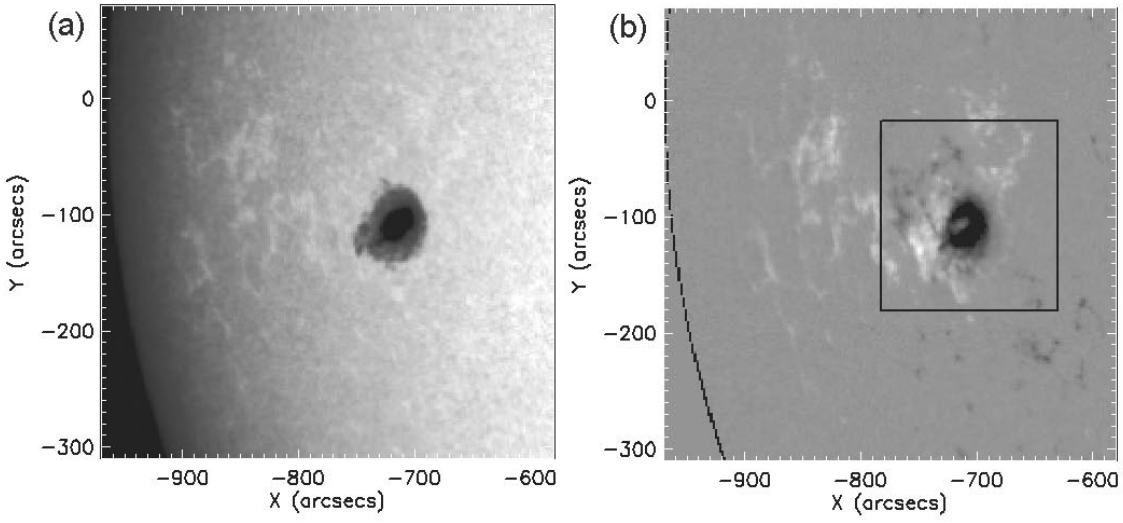

Figure 3.1 AR 10923 at the photospheric level on Nov. 10 2006: (*a*) MDI continuum map, (*b*) MDI magnetogram with the SOT-SP field of view outlined in black.

the amplitude and phase calibrators, respectively. Calibration for the attenuators, necessary for solar observations with the VLA, was carried out by T. Bastian using the latest SOLCAL data. The maps were CLEANed and self-calibrated using the standard AIPS software. After self-calibration, the rms noise in the maps was ∼1-3% of the peaks. For this study the maps were combined to form the Stokes I total intensity maps in order to make use of OVSA data, as discussed in the next section.

3.1.3 Owens Valley Solar Array Observations

OVSA is a 7-element solar-dedicated interferometer, operated by NJIT, which on this date observed the Sun at 39 frequencies from 1.2-18 GHz, providing high spectral resolution.After flagging data affected by radio frequency interference, hardware errors, and calibration problems, a total of 21 frequencies remain, ranging from 1.4 to 10 GHz. Twenty minutes of data from around the time of the small B1 flare was excluded, leaving 7 h 25 m of data. The *uv* sky coverage was enhanced by the use of Earth-rotation synthesis from an integration of the entire day's data. As described in

Chapter 2, new IDL-based code was developed to implement the L1 self-calibration algorithm (Schwab, F. R., 1982; Cornwell & Fomalont, 1999) in order to address calibration problems due to atmospheric as well as instrumental effects. As mentioned, these are the best monochromatic maps ever produced from OVSA data. However, the low number of antennas gives limited uv coverage, which in turn results in high side-lobe levels in the synthesized maps. These artifacts are not addressed by self-calibration and persist in the data. This degrades the fidelity of the maps to the level where polarization spectra yield ambiguous results. For this reason a polarization study is not supported by these data. The uncertainties introduced due of the use of the total intensity I instead of the R and L circular polarizations have been addressed in Section 2.3.

3.1.4 *Hinode* SOT Observations

The target AR was observed by the suite of instruments aboard the *Hinode* satellite. Level 2 Solar Optical Telescope (SOT) Spectro-Polarimeter (SP; Lites et al. 2001) vector magnetogram data were obtained which had a field of view (FOV) of $102'' \times 162''$ at $0.148'' \times 0.158''$ pixel resolution (Figure 3.1b). These data report a maximum field strength of about -3300 G near the sunspot center. Since the absolute pointing of the SOT observations is not well determined (HSO, 2009), data from the corresponding MDI magnetogram, whose pointing is well known, was used to co-align the data. Figure 3.2a shows the corresponding B_z contours from the co-aligned data. The outer contours match up well and were used to achieve a co-alignement better than $2''$. The inner contours of the MDI data show a level of saturation to be discussed in the following sections. The purpose of the photospheric magnetic field data in this study was to provide the boundary conditions for a non-linear force-free field (NLFFF) extrapolation of the magnetic field which could then be used to compare to the results from the radio data, aiding in the interpretation of the physical

results as well as providing an independent test for the extrapolation. However, after obtaining the extrapolation it was found to be inconsistent with expectations based on EUV data and the radio results. It was determined that the small FOV of the instrument did not encompass enough of the positive flux surrounding the sunspot, in particular to the *East*, and therefore provided inaccurate boundary conditions for a proper extrapolation. (De Rosa et al., 2009) arrived at the same conclusion from extrapolations from SOT-SP data for several active regions. Therefore, the use of SOT-SP data is limited to using the B_z component to complement MDI data (described next) as a boundary condition for a potential field extrapolation, the details of which will be described in Section 3.1.6.

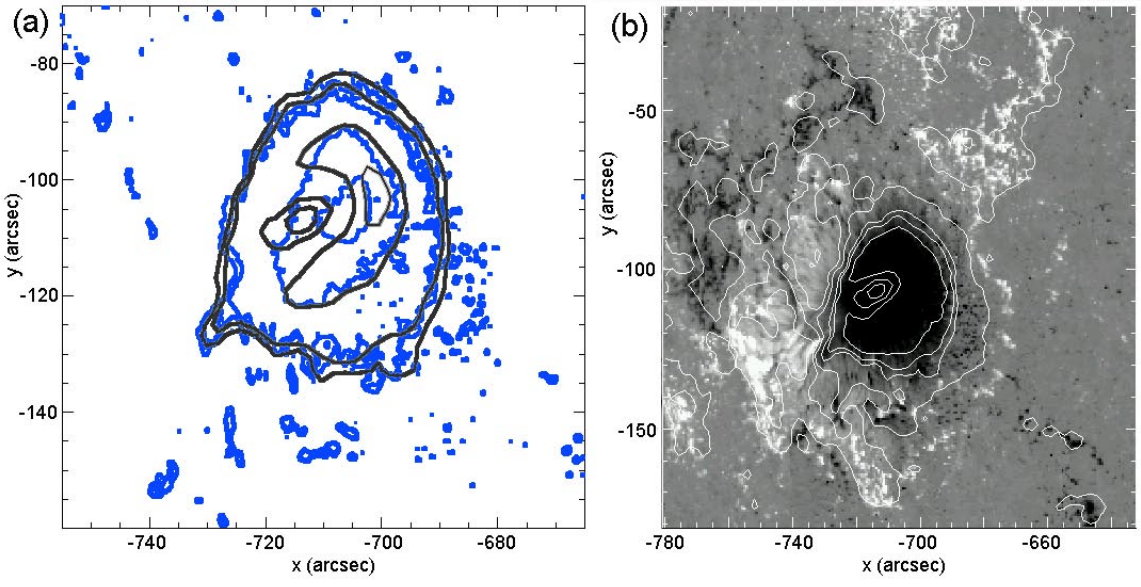

Figure 3.2 B_z contours levels 2500, 2000, 1500, and 1000 G from the co-aligned (*a*) SOT-SP (blue) and MDI magnetogram (dark grey), and (*b*) MDI contours on the continuous SOT-SP B_z map.

3.1.5 *SoHO* MDI/EIT Observations

EUV data were available from the EIT (Delaboudinière et al., 1995) while magnetogram data were available from the MDI (Scherrer et al., 1995) instruments aboard the *SoHO* satellite. In this study, the full-disk Fe IX/X 171Å, Fe XII 195Å, and Fe

XV 284Å EUV maps are used qualitatively to check the validity of the extrapolation by loop comparison. The full-disk MDI magnetogram has $1.98'' \times 1.98''$ resolution and provides the B_z component of the photospheric magnetic field. In view of the aforementioned shortcomings of the NLFFF extrapolation, it was decided to perform a potential field extrapolation, with the MDI magnetogram providing the surface boundary condition. However, it was found that the MDI magnetogram was saturated near the peak of the field which requires correction as discussed next.

3.1.6 Potential Field Extrapolation

The study of coronal magnetic fields is enhanced by the analysis of microwave measurements combined with magnetic field extrapolations. One manner in which the results of radio studies can be used is as tests of the extrapolations (White, 2004). In this sense, the magnetic field strength in the corona, obtained from radio observations, is compared to the extrapolated field strength. Field extrapolation models can also be used to validate the physical results of the radio analysis. In particular, extrapolations can provide the magnetic field strength $B(h)$ as a function of height h above the photosphere while radio observations provide the electron temperature $T_e(B)$ as a function of magnetic field strength. As a result, combined analysis can potentially provide information on $T_e(h)$. This will be explored in further detail in Chapter 5.

The choice of appropriate extrapolation technique to use is open to debate. A general, fairly realistic, but non-unique choice may be the nonlinear force-free field (NLFFF) extrapolation method that (i) provides an equilibrium solution while relaxing the unrealistic uniform-twist requirement of a linear force-free field (LFFF) extrapolation and (ii) does not preclude very weak electric currents, in the sense that it can asymptotically converge to a current-free, potential solution. NLFFF extrapolations, however, are still an open research topic with different methods applied

to the same boundary giving notably different results (Schrijver et al., 2006, 2008; Metcalf et al., 2008). De Rosa et al. (2009), in particular, showed that NLFFF extrapolations applied to data from the SP instrument alone may provide unreliable estimates of the coronal magnetic field as they are based on incomplete boundary conditions. One of the proposed treatments in this case was to use vector magnetogram data with a much larger field of view to account for more of the electric currents associated with a given AR. Unfortunately high-resolution vector magnetograms over wide fields of view were not available for the time of these observations. Because of the relative simplicity of AR 10923 it is reasonable to assume that the field is approximately potential. For the above reasons there was a deliberate choice made to use a current-free extrapolation applied to the normal photospheric field component over a wide field of view as the preferred extrapolation method for this study. It is expected that the comparison of the $B_{\rm tot}$ values inferred by radio observations to the well-known, unique potential-field solution will reveal the areas where strong electric currents persist, thus forcing the observational and extrapolated $B_{\rm tot}$ to disagree, while also showing the areas where weak or absent electric currents allow observed and extrapolated magnetic field values to reasonably agree with each other.

3.1.6.1 Boundary Conditions. The potential-field extrapolation requires a sizable patch of the solar photospheric line-of-sight magnetic field from the *SoHO*/MDI magnetogram enclosing AR 10923. The steps taken to derive the extrapolation were to (i) calculate the heliographic plane corresponding to the chosen field of view (Gary & Hagyard, 1990) and (ii) interpolate the cosine-corrected normal magnetic field component on this plane. Before performing the above calculations, however, an effort is made to improve the realism of the boundary condition by treating the saturation present in the *SoHO*/MDI data. Saturation in the MDI magnetogram can be seen as an island of less negative flux within the umbra in

the MDI contours overlaid on the SOT-SP B_z map in Figure 3.2. The SP magnetogram, derived from spectral polarimetry, is not saturated but, as mentioned above, its field of view only covers the central region of the AR. After verifying that the data from both instruments reported equivalent levels in areas away from the saturation (Figures 3.2 and 3.3b), which justifies combining the data sets, a composite MDI-SP magnetogram is constructed by embedding the appropriately spatially rescaled SP B_z map into the MDI magnetogram. A section of the combined magnetogram large enough to encompass all of the prominent magnetic flux of the active region (Figure 3.3a) is used. De Rosa et al. (2009) used a similar approach to improve the boundary conditions for their extrapolations.

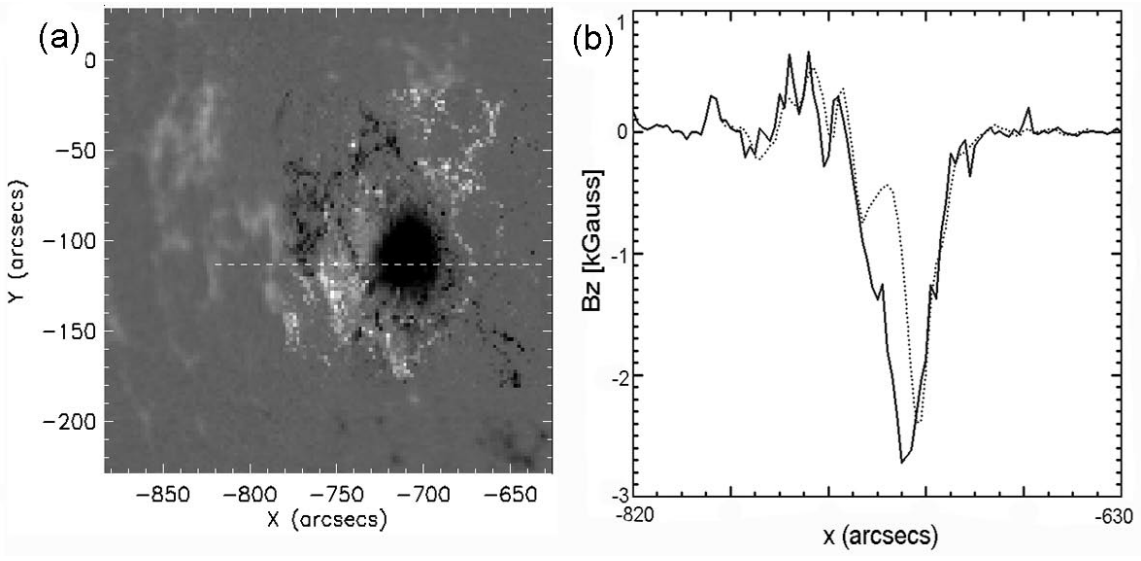

Figure 3.3 Composite magnetogram of AR 10923:*a*) field of view of the composite MDI/SOT-SP magnetogram used for the extrapolation. (*b*) Comparison of SP (solid) and MDI (light dots) B_z levels along the dashed line in *b*, depicting the matching and saturation areas.

3.1.6.2 Extrapolation Method. To implement the potential extrapolation the Green's functions method as implemented by Schmidt (1964) on Cartesian geometry (see also Georgoulis & LaBonte 2007) is used. Schmidt's (1964) method gives an exact solution, providing potential fields and subsequent zero electric cur-

rents up to machine accuracy. The method is much more accurate than the potential (or LFFF) extrapolation techniques relying on fast Fourier transforms (Alissandrakis, 1981) but, in return, it is much more computationally intensive. This expense was taken, nevertheless, as increased accuracy is preferred in order to precisely pinpoint possible discrepancies between the function $B(h)$ as estimated by radio observations and the extrapolated $B(h)$, without concern for numerical uncertainties in the extrapolation. This extrapolation explicitly ignores electric currents, so observed discrepancies should indicate either uncertainties in the observationally inferred $B(h)$ or areas where the potential approximation breaks down, meaning that magnetic field lines are notably distorted by the existence and action of local electric currents. Figure 3.4 displays sample field lines from the resulting extrapolation overlaid on the EIT 171Å and XRT Al-med maps to demonstrate general agreement between the model and the location of sources from observations.

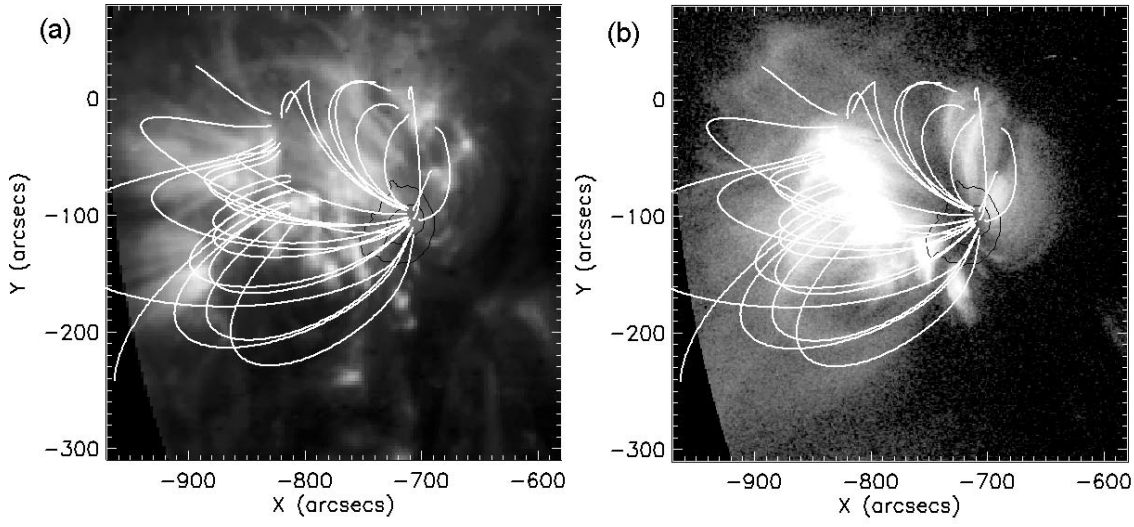

Figure 3.4 Selected field lines from the potential field extrapolation overlaid on (*a*) EIT 171Å and (*b*) XRT Al-med maps. The location of the field lines generally agrees with the location and shape of the EUV and soft X-ray sources observed. The umbral and penumbral boundaries are outlines in black.

3.2 Joining VLA-OVSA Data and Spectral Analysis

3.2.1 VLA-OVSA Correlation and Co-alignment

The joint VLA-OVSA data samples AR 10923 at 25 frequencies from 1.4-14.96 GHz. All maps were resampled to the resolution of the 10 GHz map of $2.3'' \times 2.3''$ pixels for co-alignment and selection of the field of view within which to carry out the analysis. This pixel resolution only under-samples the VLA's U-band map, which has a pixel resolution of $0.5''$, and over-samples all the other maps. It was shown in Chapter 2 that the self-calibrated OVSA maps nearly match the VLA's in amplitude and structure. Because the VLA maps were convolved to the OVSA resolution using the beam parameters at the OVSA near-frequencies, similar T_b contours are then expected to overlay to some extent. A comparison with VLA maps at similar frequencies showed that the OVSA phase center was off by about $94''$. Since the VLA's phase center is well known, the appropriate shift was found by co-aligning OVSA's 4.8 GHz map to the closest-frequency map from VLA at 4.82 GHz. Since the T_b and structure matches are not exact (Figure 3.5a), a compromise in the overlay was reached between the outer contours and the positions of the peaks. The alignment is estimated to be good within $\sim 3''$, on the order of the pixel resolution of the averaged maps. Applying this fixed shift to all the OVSA maps yielded good spatial agreement at other nearly-shared frequencies. This is particularly evident in the 8.2 GHz display (Figure 3.5c) because the source is small and the peaks coincide within a small area. The co-location of the peaks in the 1.4 GHz display (Figure 3.5b) is also clear. Once co-aligned, the maps were averaged over 4×4 pixel areas to further reduce noise in the derived spectra. The final maps in the data cube consisted of 64×64 pixel arrays where each pixel covers a $9.2'' \times 9.2''$ area.

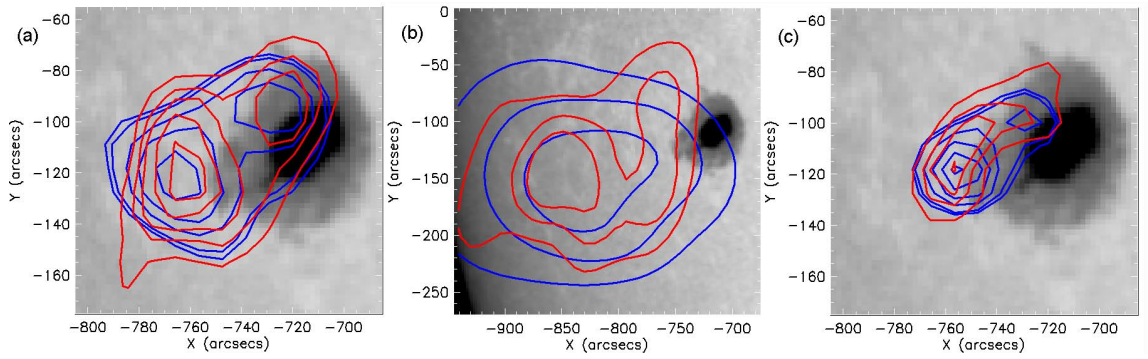

Figure 3.5 Contour overlays demonstrating the OVSA (red) and VLA (blue) alignment. (a) contour alignment at 4.8 GHz of levels=[0.7, 0.8, 1.1, 1.4, 1.8] is used to align the rest of the OVSA data, resulting in verified peak location matches at (b) 1.4 GHz and (c) 8.2 GHz. The low resolution of the VLA's 1.4 GHz map is a consequence of the convolution to the OVSA resolution, which is not as evident at the other frequencies.

3.2.2 Frequency dependent behavior of T_b maps

Brightness temperature maps convey information about the source temperature at a given frequency, where T_b=T_e when the source is optically thick and T_e when it is optically thin, as discussed in section 1.2. A selection of T_b maps from the joint OVSA-VLA data set is displayed in figure 3.6, with contour levels 0.3, 0.4, 0.6, 0.8, 0.9 times the maximum T_b in each map. The -1000 and 500 G contours from the composite magnetogram are underlaid in grey for reference, the negative polarity contour appearing circular while the positive contour to the SE has a triangular shape. The behavior in frequency of the T_b maps is typical of that seen in previous radio studies. That is, at low frequencies the source is large and covers the entire active region but shifted to the limbward side, decreasing in size with rising frequency. At 1.4 GHz (panel a), the OVSA and VLA maps show an extended source with a peak 130″ SE of the sunspot center. The maximum T_b is of 1.72 MK, so that the contours overlying the sunspot are $\leq$ 1 MK. At 1.8 GHz (panel b), the maximum T_b is 1.4 MK and the source still covers a large area. At 3.2 GHz (panel c) the

maximum T_b has risen to 1.98 MK. The source is smaller and the location of the peak has shifted to regions overlying the strong magnetic fields of and around the sunspot. Panel (d) shows that the source at 4.4 GHz has become localized above the sunspot region, with its two T_b peaks overlying the neutral line to the SE and the NW edge of the negative polarity sunspot. The maximum T_b at this frequency is 2.1 MK. Previous studies have shown that the hot, sunspot-associated sources at 4.8 GHz and above are emitted via the gyroresonance emission mechanism (e.g. Lang & Willson, 1980, 1982; Alissandrakis & Kundu, 1982; Chiuderi-Drago et al., 1982; Shevgaonkar & Kundu, 1985; Gopalswamy et al., 1991; Zlotnik et al., 1996, 1998), while away from these sources, at the same frequency, the radiation is from optically thin free-free emission (Felli et al., 1981; Gary & Hurford, 1987). As will be shown through the maps of physical parameters presented later in this chapter, the spectra away from the main source at 4.4 GHz show optically thin free-free emission while the source itself is hot and quite optically thick. Therefore, at 4.4 GHz, the brightness temperature maps are already dominated by gyroresonance emission. This conclusion might also apply at lower frequencies, as inferred by the rising temperature and position shift at 3.2 GHz. Panel (e) displays the OVSA and VLA contours at 4.8 GHz, with a maximum T_b of 2.23 MK. The source is now completely confined to the regions of strong photospheric field. The source now gradually decreases in size and temperature with rising frequency. The drop in T_b has an exception at 8.48 GHz (panel g), the VLA's X-band, where the maximum is about 0.3 MK higher than expected from the OVSA data's dropping T_b trend. The 8.2 GHz map shown in the same panel displays a similarity in size and shape not greatly affected by this discrepancy. Unresolved structure at higher temperatures, as observed by the OVSA, could account for a discrepancy in reported temperatures. At the highest frequency available, 14.95 GHz from the U-band, the source is considerably confined, centered above the neutral line, and has dropped in temperature to a maximum of 0.8 MK.

Because emission at higher frequencies arise from deeper in the corona, the study of the frequency behavior of the single-frequency T_b maps provides clues to the behavior of the microwave emission with height. In order to better quantify this behavior, a spectral study of the data is necessary, and described now.

3.2.3 Spectral Analysis and Two-component Model

With the OVSA data set improved by the VLA's additional points, and the frequency range extended two-fold, the spectral-fitting method employed by Gary & Hurford (2004) was automated, fitting individual spectra with isothermal brightness temperature spectral models representing either free-free or gyroresonance emission. The free-free models had a frequency dependence of ν^{-2} in the log-log scale, and the gyroresonance models were allowed a variable frequency dependence from ν^{-5} to ν^{-10}. This large interval was chosen in order to encompass the theoretical range of possible slopes for gyroresonance emission (Dulk, 1985), although actual observations should have slopes on the shallower end of that range (Gary & Hurford, 1994). While several spectra were fit well with such models (Figure 3.7a, b), most of the spectra near the sunspot were not since they have a positive slope in the optically thick, low frequency portion. This slope presents a wider range of temperatures than in flat spectra, and so is not fit well by a single temperature model. Figure 3.7c shows a gyroresonance type model fit that appears ok at the lower and at the higher frequencies, but completely misses the data points at middle frequencies. Figure 3.7d shows a spectral fit that misses several data points in every one of these ranges. These positive slopes are of the same type as Gary & Hurford (2004) found in some of their spectra. For these spectra it is obvious that the homogeneous corona model does not fit the data well.

Gary & Hurford (2004) proposed three possible explanations for their observed positive-slope spectra: 1) a non-thermal electron population, 2) low resolution at

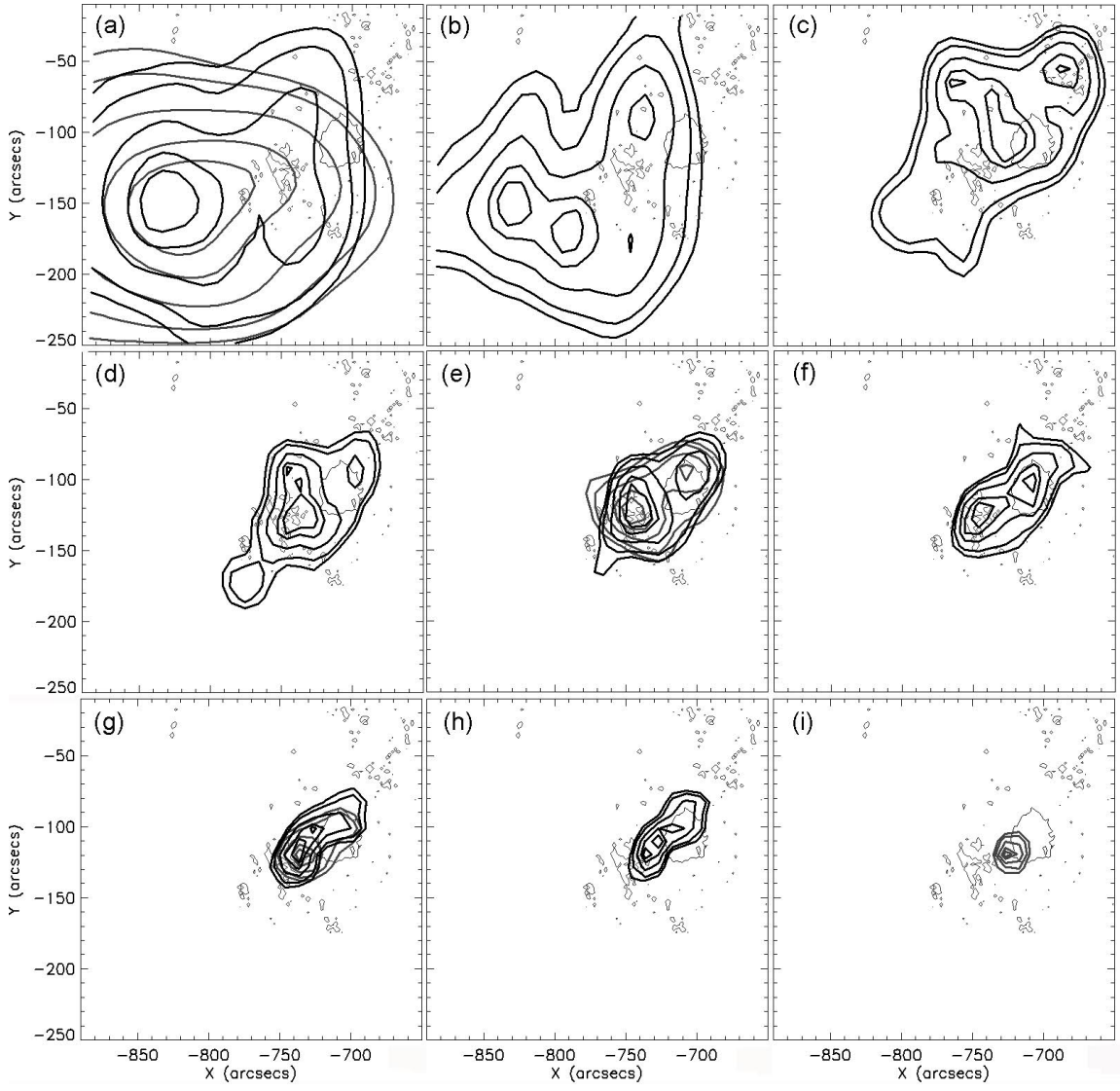

Figure 3.6 OVSA (black) and VLA (grey) brightness temperature contours at various frequencies, over the -1000 and 500 G B_z contours from the SOT-SP. T_b levels of 0.3,0.4,0.6,0.8,0.9 times the maximum temperature in each map are displayed. The OVSA and VLA near-frequencies are plotted on the same map. (a) 1.4 and 1.41 GHz, $T_{b,max}$=1.72 MK, (b) 1.8 GHz, $T_{b,max}$=1.41 MK, (c) 3.2 GHz, $T_{b,max}$=1.98 MK, (d) 4.4 GHz, $T_{b,max}$=2.11 MK, (e) 4.8 and 4.84 GHz, $T_{b,max}$=2.23 MK, (f) 6.2 GHz, $T_{b,max}$=1.91 MK, (g) 8.2 and 8.48 GHz, $T_{b,max}$=2.09 MK, (h) 10 GHz, $T_{b,max}$=1.35 MK, (i) 14.95 GHz, $T_{b,max}$=0.8 MK.

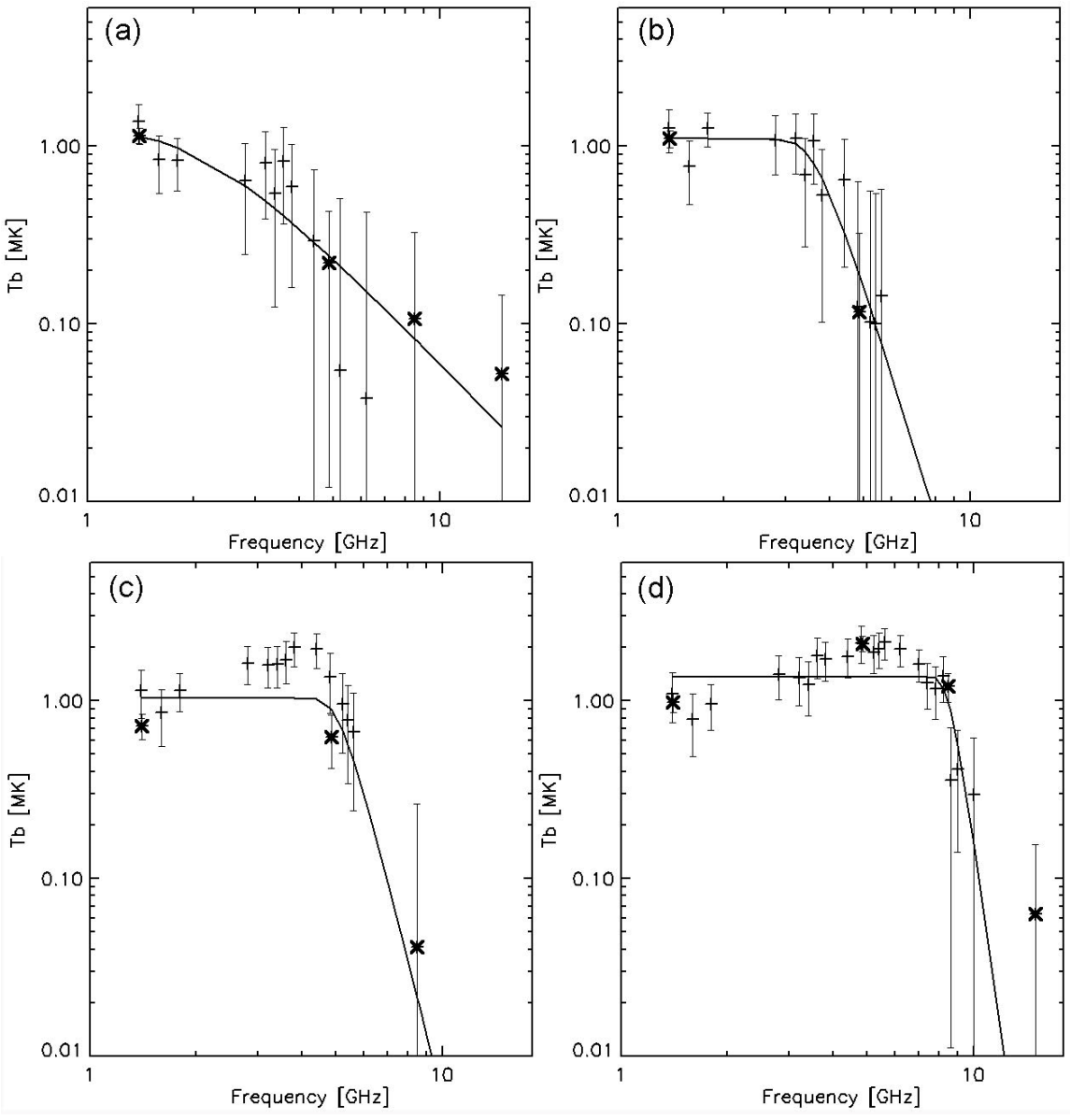

Figure 3.7 Sample T_b spectra fit with single-temperature, single-emission mechanism models (solid lines). The OVSA (+) and VLA (**X**) are plotted with their corresponding error bars. These are log-log plots, and so the errors appear "stretched" towards the bottom. (a) a spectrum well fit with a free-free emission model, (b) a good gyroresonance fit, (c) the spectral fit lies between most error bars (although the VLA data point at 1.4 GHz is missed) but all of the points at the top of the mid-frequency temperature rise are missed, (d) the best fit to this spectrum represents an average of values, which is sufficiently bad as to miss data points at every frequency, even the more heavily weighted VLA data points.

low frequencies not being able to resolve all the structure, or 3) a cooler (1 MK) medium overlying a hotter (3 MK) source. On the first point consideration must be given to the fact that the radio maps are produced from all day integration of the radio data. In order for the signature of a non-thermal population to appear in such maps, the brightness temperatures reached should be quite high, such as with flares or peculiar, neutral-line sources (Alissandrakis et al., 1993), or the population should be sustained for a large portion of the observation time. As mentioned before, the data around the single, small flare have been excluded from the Earth-rotation synthesis maps and no other significant brightness fluctuations appear in the data. That all the spectra over the strongest photospheric fields, covering an area slightly larger than the sunspot, exhibit the positive-slope feature at varying levels further brings into question the sustainability of such a spatially wide-spread population over a large portion of time. The second possibility also seems unlikely to apply to this data set, since the target active region is spatially much simpler than the one studied by Gary & Hurford (2004). The T_b maps show that at low frequencies the peak occurs well to the east of the region of positive-slope spectra. The original VLA map, before convolution to the OVSA 1.4 GHz resolution is able to easily resolve the structure of the source. As noted in the previous section, the location of the peak shifts to the sunspot region and the temperature rises at slightly higher frequencies. If the high coronal temperature observed over the sunspot at high frequencies extended to greater heights, it should be reflected in a separate, if reduced, free-free (low-frequency) temperature peak at that location. Such a feature is not seen in any form. While these arguments are qualitative, they cast doubt on the viability of the first two solutions for explaining the distribution of positive-slope spectra.

The third possibility, a cooler component overlying a hotter one, seems to be supported by the results of previous spectral studies mentioned in the Chapter 1. In accordance with the results of the single or sparse frequency studies discussed

there, free-free emission must dominate at low frequencies while gyroemission takes over at higher ones. To explore this configuration, the algorithm was modified to fit the spectra with a two component model where a hot gyroresonance component underlies a cooler, but still of MK order, free-free component. This radiative transfer model is of the form

$$T_b = T_{e,\mathrm{gyro}}(1 - e^{-\tau_{\mathrm{gyro}}})e^{-\tau_{\mathrm{ff}}} + T_{e,\mathrm{ff}}(1 - e^{-\tau_{\mathrm{ff}}}) \tag{3.1}$$

where $\tau_{\mathrm{ff}} = \alpha/\nu^2$ and $\tau_{\mathrm{gyro}} = \beta/\nu^5$, giving the model's free-free component's optically thin portion a frequency dependence of ν^{-2} and the gyroresonance factor one of ν^{-5}. The observing frequencies when the τ parameters become unity are obtained directly from the model fit since then $\nu_{\mathrm{ff},\tau=1} = \alpha^{1/2}$, and $\nu_{\mathrm{gyro},\tau=1} = \beta^{1/5}$. The values of $T_{e,\mathrm{ff}}$ and $T_{e,\mathrm{gyro}}$ are also obtained directly from the fits. This frequency dependence for the gyroresonance component is chosen because, as mentioned in §3.1, actual observed spectra will have a frequency slope at the shallower end of the expected range. This is because of temperature and density inhomogeneities within the resolution element or along the line of sight (Gary & Hurford, 1994). The slope is further reduced by combining the polarization information into the Stokes I parameter. In any case, it was found that every gyroresonance slope in our data can be adequately fit with such a model.

An example of how well these spectra are fit with the two component model is shown in Figure 3.8. In order to easily assess the effect of the two-component model, the spectra displayed are for the same lines of sight as in Figure 3.7. Panels a and b of Figure 3.8 show the flexibility of the method. These spectra were well fit with a single component model in the previous method and remain so after the new model is used. The improvement can be easily verified in panels c and d of the same figure, where the previously ill-fit spectra are now represented by a model that passes through the majority of the error bars at each data point. Panel d of this figure also shows the behavior of the individual components if the other was not present. The

combined behavior, through the radiative transfer model in Equation 3.1, produces the matching spectra. The free-free component is optically thick at low frequencies, dominating the T_b spectrum. As the frequency increases the free-free spectrum becomes optically thin ($\tau_{\rm ff} < 1$) and the gyroresonance component begins to dominate, raising T_b since $T_{e,\rm gyro} > T_{e,\rm ff}$. This configuration indicates that the actual peak temperature of the gyroresonance component is hotter than the observed brightness temperature for some lines of sight. There is a possibility that the T_b spectra represent a change in temperature amongst the various gyroresonance layers, so that the spectrum is simply reflecting these changes. This view, however, is hard to reconcile with the requirement for optically thick free-free emission at the lowest frequencies. This is because the free-free absorption coefficient has a fixed ν^{-2} dependence on frequency and, for high optically thick temperatures the absorption has an influence that extends to the higher frequencies. Small variations are possible, such as reducing the gyroresonance temperature at the lowest frequencies, but the data are not of sufficient quality to explore more subtle variations than those represented by the two component model. As will be seen in the analysis, when the two-component model fits are applied to the entire field of view, this algorithm reproduces the known results where free-free emission dominates over the plage areas of the AR and gyroemission is the chief mechanism over the sunspot area. However, there is an area where the two regimes overlap to produce spectra like that in Figure 3.8, thus yielding a stratified coronal model. Although the radio data alone do not provide an estimate of the spatial separation between the two layers, the vertical separation is a step towards a three-dimensional mapping based purely on observations.

3.2.4 Maps of Physical Parameters

The temperature distributions of the two components plotted over the SP-MDI magnetogram are displayed in Figure 3.9*a*, with the gyroresonance T_e contours in red

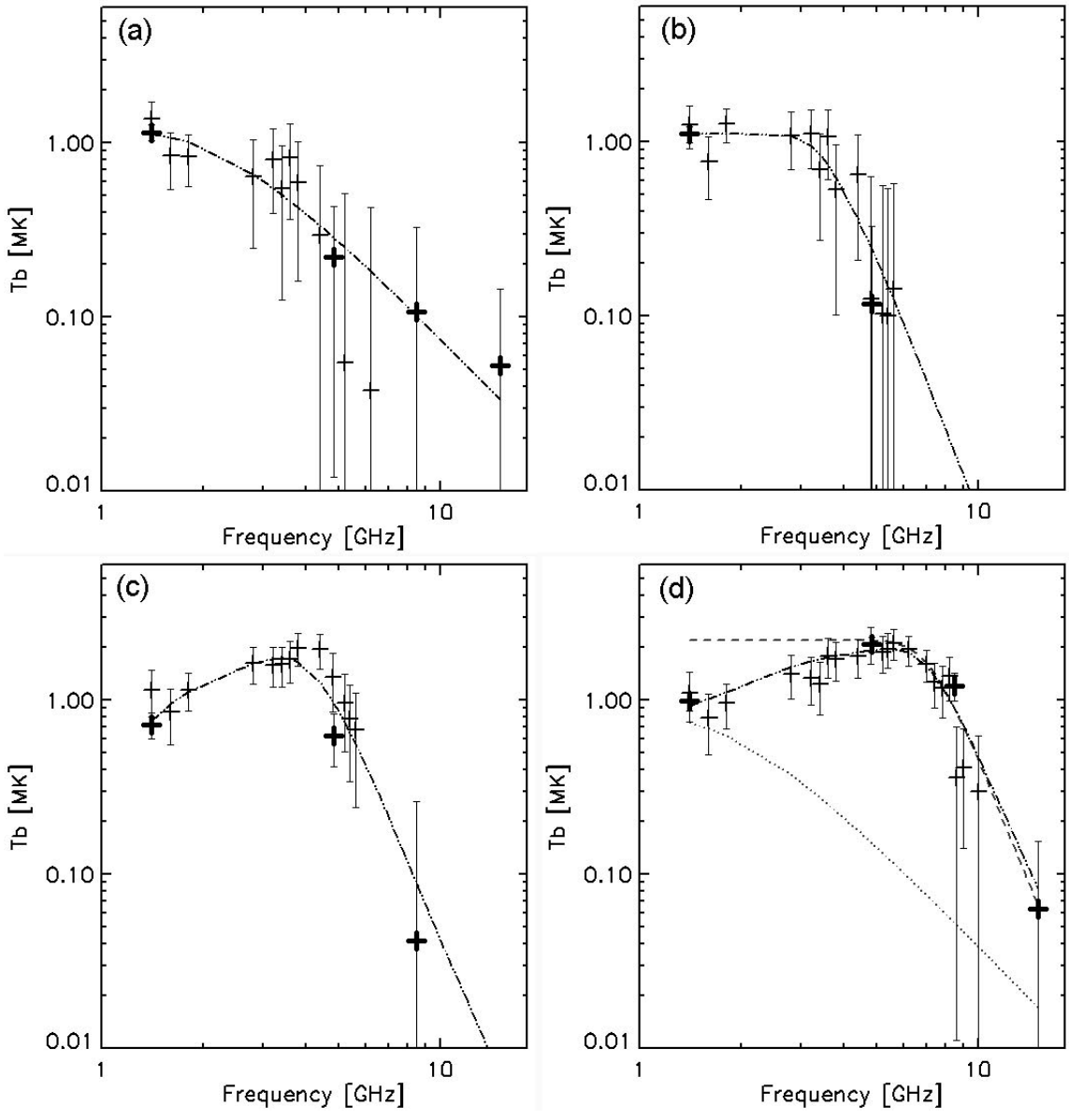

Figure 3.8 Sample T_b spectra corresponding to the same lines of sight represented in Figure 3.7, now fit with a two-emission models where each component has an independent temperature (dash-dot-dot lines). The OVSA (+) and VLA (**X**) are plotted with their corresponding error bars. (a) the free-free fit remains the best fit for this spectrum, (b) as does the gyroresonance only model for this spectrum, (c) improved fit to the spectrum in Figure 3.7c, (d) improved fit to the spectrum in Figure 3.7d. The individual free-free (dotted) and gyroresonance (dashed) components are also plotted.

and the free-free ones in yellow. The gyroresonance component reaches a peak temperature of 2.5 MK while the maximum in the free-free distribution is 1.6 MK. The gyroresonance electron temperatures exhibit a two-peak structure with one peak directly over the B_z peak and the other, higher T_e peak aligned N-S over the region of scattered positive photospheric magnetic flux directly adjacent to the SE of the sunspot. The free-free T_e distribution has its single peak over a region about 130″SE of the sunspot while the entire distribution covers a large area encompassing the photospheric plage region. The spatial arrangement of the two components is in agreement with the well-established influence of free-free emission over the plage areas and of the dominance of gyroresonance emission near the sunspot. Notably, that these distributions exhibit smooth spatial continuity and reproduce results obtained from single-frequency studies is important since they were obtained through model fits to spectra corresponding to individual pixels, each fit independent from all others.

Figure 3.9*b* displays the same elements as in 3.9*a*, now overlaid with a sample of field lines from the potential field extrapolation. In this view, the peak of the free-free temperature distribution is co-located with the tops of loops connecting the central portion of the extended plage to the sunspot. Long field lines reconnect to the negative-polarity sunspot and the legs of these loops are co-located with the distribution of gyroresonance temperatures. These inferences agree with the conclusions of previous studies where the free-free dominated emission from VLA's *L*-band maps comes from loop tops reconnecting sunspots within ARs (Gary & Hurford, 1987; Vourlidas et al., 1996) and that gyroresonance dominates when the magnetic field is strongest, near the base of the corona over sunspots. The tops of the loops extending to the N of the sunspot do not have a significant radio-derived temperature co-located with them. Knowledge of the temperature at the loop tops and foot points also places additional constraints on the transport of heat along the loop itself.

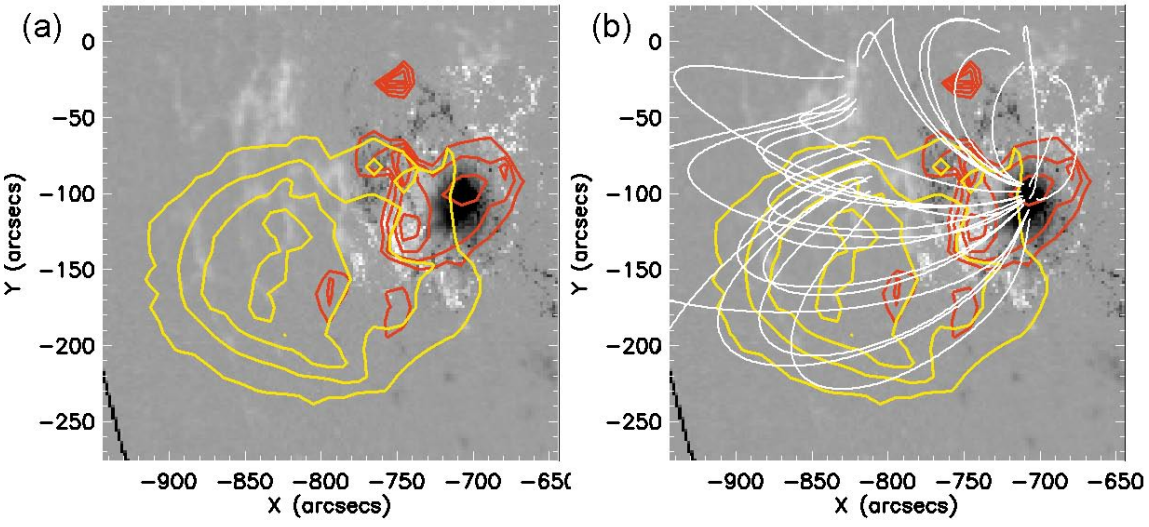

Figure 3.9 Temperature distributions on the combined SOT-SP/MDI magnetogram: (*a*) $T_{e,\mathrm{gyro}}$ (red) and $T_{e,\mathrm{ff}}$ (yellow) with levels=[0.3, 0.5, 0.7, 0.8, 0.9]$\times T_{\max}$, where $T_{\max}$=1.6 MK for free-free and $T_{\max}$=2.5 MK for gyroemission, and (*b*) the same contours with representative field lines from the extrapolation.

The values for the column emission measure (EM) were obtained only for the pixels containing a free-free component, since the equation is valid only for this mechanism. Further constraints were imposed on the pixel selection for this quantity, since the resulting turnover frequency from the model fit is used. The contours for levels 12, 19, 70, and 130×10^{27} cm^{-5} are shown on the EIT 195Å and XRT's C-poly maps in Figure 3.10. These values are within an order of magnitude with those found by Gary & Hurford (2004). The peak of the EM is outlined in black and overlies what appear to be loop foot points in EUV and the bottom edge of the brightest emission in X-rays. A $T_{e,\mathrm{ff}}$ contour (white) outlining the peak of that distribution is included in the EIT map to show that the greatest EM values occur away from the $T_{e,\mathrm{ff}}$ peak. The shape and location of these higher EM values do not appear to correspond to the overall features in the displayed maps, which sample the corona above the AR. A plausible explanation for this distribution will be presented in §4.2.

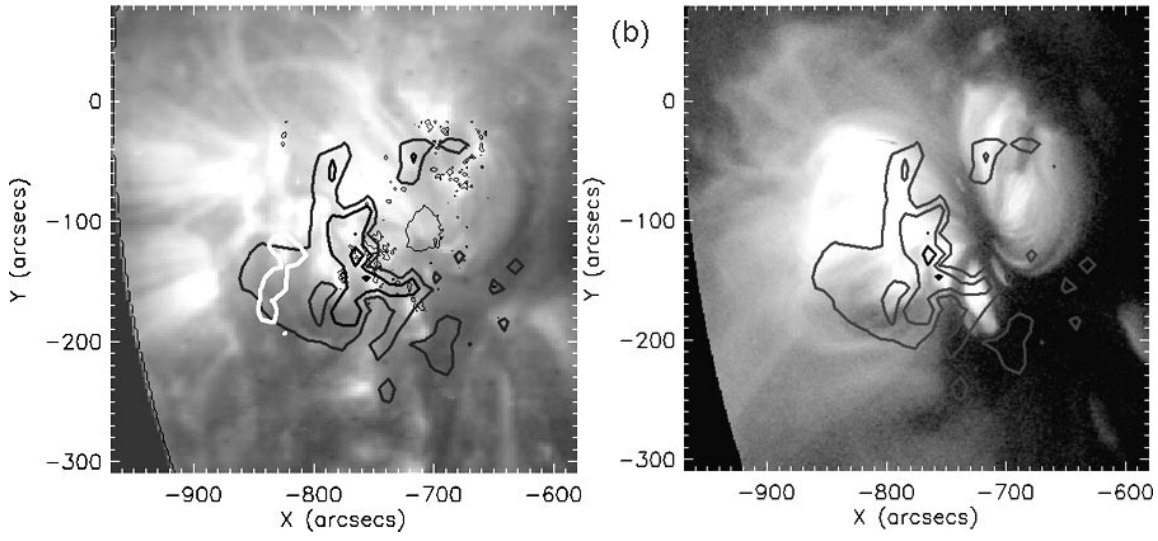

Figure 3.10 Emission measure levels 20,60, and 120×10^{27} cm^{-5} (gray to black) on (a) EIT's 195Å map with the $T_{e,\mathrm{ff}}$=1.4 MK contour in white for reference, and (b) XRT's C-poly filter map.

Finally, the contours for B_{tot} of the last optically thick layer along each line of sight for a single harmonic, in this case s=3, are overlaid on the combined SOT-SP/MDI magnetogram in Figure 3.11a. The gyroresonance spectra turn over due to the rapid drop in temperature from coronal to chromospheric values, so these contours delineate the total magnetic field at the base of the corona. Since the base of the corona is only about 2000 km above the photosphere some correlation is expected between these contours and the photospheric field. Indeed, the radio-derived contours cover the region of strongest photospheric flux of both polarities. The locations of the peaks of the photospheric B_z (white plus sign) and the coronal-base B_{tot} are displaced by $\sim 28''$. The B_{tot} peak lies over the neutral line. Such displacements of coronal to photospheric magnetic field peaks has been encountered in previous studies (Gary & Hurford, 1994; Nindos et al., 2000), but the reason for the displacement has not been determined. A natural and compelling explanation for this will be explored in Chapter 5. Figure 3.11b shows the same contours over

the MDI continuum map. This overlay shows that the location of the coronal-base $B_{\rm tot}$ peak is directly over the umbra/penumbra border.

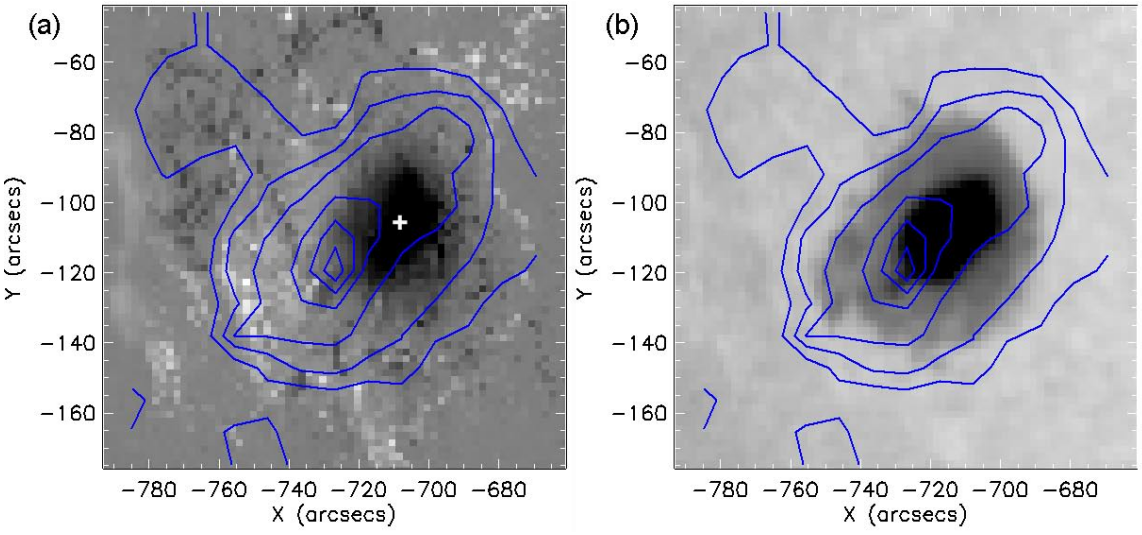

Figure 3.11 $B_{\rm tot}(s{=}3)$ levels 0.3, 0.6, 0.8, 1., 1.3, 1.5 kG on (a) SP/MDI magnetogram with the peak in B_z denoted by the white +, and (b) on the MDI continuum map. The $B_{\rm tot}$ peak lies over the neutral line, directly over the umbra-penumbra border.

Since the temperature of the last optically thick layer can be read directly from the spectral fit, the derived temperature and magnetic field distribution at the base of the corona are explored concurrently. Figure 3.12a outlines $B_{\rm tot}(s=3)$ in white contours over the T_e distribution, shown in grey-scale. The pixelization of the T_e distribution reflects the $9.2'' \times 9.2''$ pixel size of the averaged data, as discussed in section 3.2.1, viewed in this $180'' \times 180''$ field of view. The negative sunspot is outlined by the contours in black while the positive 500 G contour is outlined in light gray. There is a temperature peak over the contours of positive photospheric field, while both hot and cooler temperatures are found within the negative, umbral region. As noted earlier, the peak of the $B_{\rm tot}$ contours lies between the region of strong negative-polarity and the weaker positive-polarity flux. The letter labels in the map denote regions whose spectra are displayed in Figure 3.12b, c, and d.

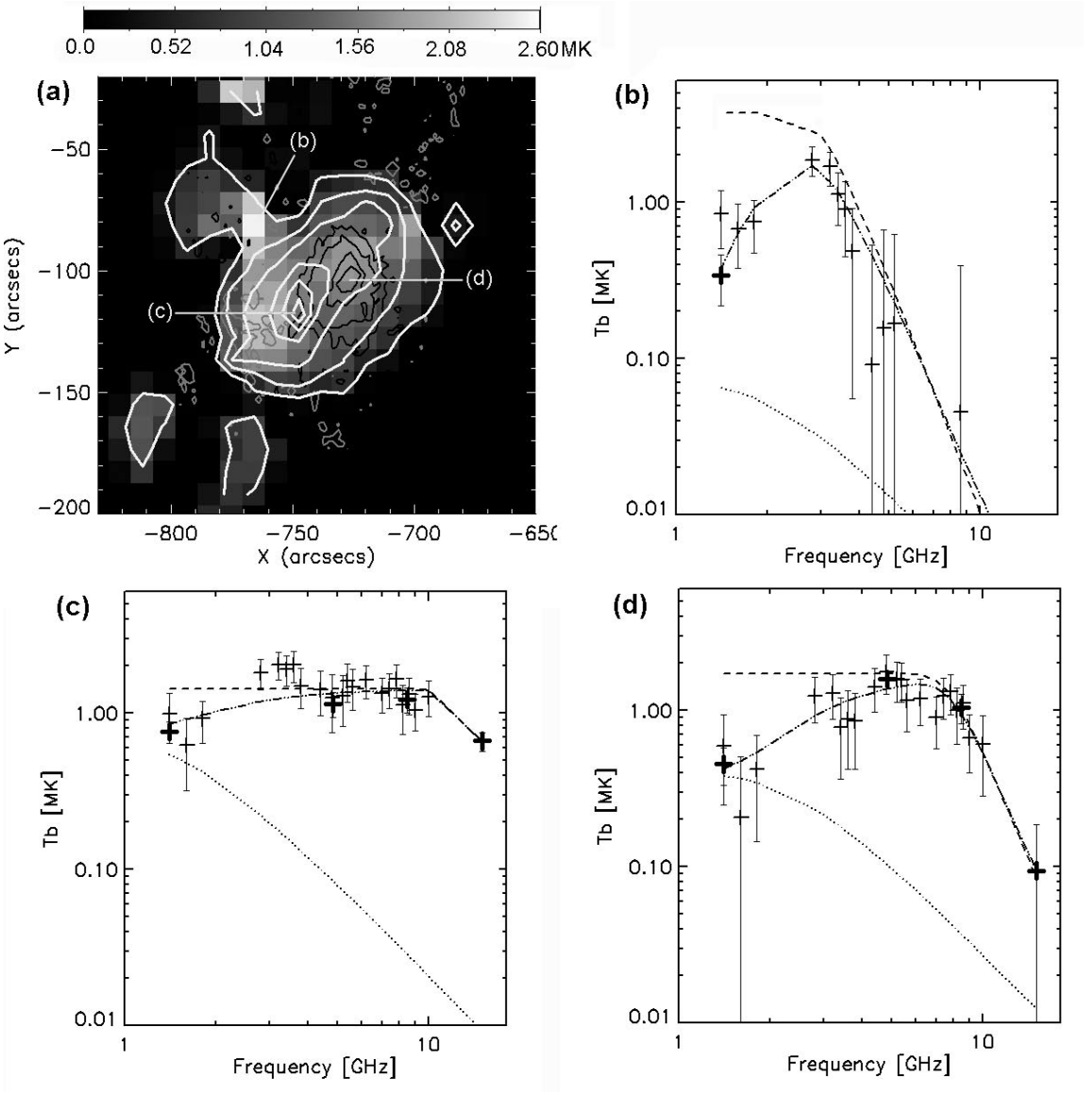

Figure 3.12 Radio-derived $T_{e,gyro}$ and $B_{\rm tot}$ distribution and sample spectra: (a) $B_{\rm tot}$ 0.7, 0.8, 0.9, 1.0, 1.4, 1.6 kG contours (white) over T_e (grey scale in color bar), with MDI B_z contours for reference, (b) radio spectrum from the location labeled "(b)" in panel a, corresponding to the $T_{e,gyro}$ peak, (c) spectrum corresponding to the $B_{\rm tot}$ peak at location "(c)", and (d) spectrum corresponding to location "(d)", at the photospheric B_z peak.

Figure 3.12*b* shows the spectrum corresponding to the location directly above the absolute T_e peak (location "b"). The high temperature is a consequence of the homogeneous T_e assumption for each component forced to fit to the low-frequency temperatures. However, the value of $\nu_{\tau=1}$, and therefore of $B_{\rm tot}$, is not affected by this assumption and it is clear that there is a MK signature at the turnover frequency. Figure 3.12*c* corresponds to location "c", which lies over the neutral line and corresponds to the peak of the radio-derived $B_{\rm tot}$ distribution. The turnover frequency read from the gyroresonance component corresponds to $B_{\rm tot} = 2.43, 1.62$ kG for $s = 2, 3$. Both the $s = 2$ and 3 values are quoted since the appropriate harmonic is not yet known at this stage. Figure 3.12*d* shows the spectrum over the peak of the photospheric B_z (location "d"). The optically thick temperature of the gyroresonance component is higher than that at location "c", yet the turnover occurs at a lower frequency, resulting in $B_{\rm tot} = 1.33, 0.89$ kG for $s = 2, 3$. The two component model reliably fits these spectra, and demonstrates how the displayed distributions are derived.

3.3 Determination of Harmonic Number

As was just mentioned, the harmonic number for the last optically thick layers is not determined from these radio spectra. Only high-quality polarization observations, such as those simulated using the Mok et al. (2005) model and shown in Figure 2.11, would exhibit sufficient precision to determine the responsible harmonics directly from the radio spectra by taking the ratio of turnover frequency from each polarization spectrum as described in Section 2.3. The available data do not permit this level of separation along any line of sight. This is one of the ambiguities that led to use of I instead of R and L spectra for this analysis. As was described in Section 2.3, the Stokes I spectrum turns over at the same frequency as that of the polarization with the lowest optically thick harmonic, with a small margin of error. The

fitting algorithm returns a turnover frequency $\nu_{\tau=1}$ for each line of sight that is adequately fit with a gyroresonance component, from which $B_{\rm tot}$ can be calculated if s is known. The possible values of $B_{\rm tot}$ are limited to harmonics s of the fundamental gyrofrequency, *i.e.,* $s = 2, 3$, and possibly 4 under coronal conditions. Thus, for a given line of sight, there are only three possible values of $B_{\rm tot}$ corresponding to the three possible harmonic numbers. Since the polarization signature in the data is of insufficient quality to obtain the correct harmonic independently, the potential field extrapolation is used to calculate which of these harmonics are optically thick. The extrapolation provides only θ, the angle between the magnetic field vector and the line of sight. The rest of the parameters are obtained from observations.

The current-free extrapolation was de-rotated from the heliographic plane back into the image plane corresponding to the day's observations. The rotated extrapolation is resampled to the resolution of the radio observations so that there is a direct pixel-to-pixel correspondence in x, y, where each pixel represents a line of sight along z. At each pixel with a gyroresonance component and therefore with three possible values of $B_{\rm tot}$, the extrapolation is searched for the location in z where the values are matched, and the optical depth is calculated at these locations. Since these values correspond to a single turnover frequency, the optically thick layer closest to the observer is the one responsible for the observed emission. By resolving the issue of appropriate harmonic, the magnetic field strength of the last gyroresonance layer in the corona for each line of sight is determined. The method is then applied to all lines of sight independently.

For the calculations of optical depth the exact equations are required, since the various approximations often used have been shown to have various problems (Vourlidas et al., 1997). The full equations for optical depth of the two wave modes are obtained from Vourlidas (1996) as derived from the corrected formulae of Melrose & McPhedran (1991). The value of T_e and B are observables obtained directly from

the spectrum. The value of θ, the angle between the magnetic field and the line of sight, is obtained from the extrapolation at the matching location for each of the possible values of B. For the electron density n_e an array of values of [8.5, 9, 9.5, 10]$\times 10^9$ cm^{-3}, which covers the range of values found from previous studies (i.e Shevgaonkar & Kundu 1985; Gary & Hurford 1987; Lee et al. 1993), was employed. The studies quoted obtained the higher values for high frequency observations, up to 15 GHz, while the lowest value is from a turnover frequency of 4 GHz. In addition, several workers report that $\tau_{\rm gyro}$ is not as greatly affected by the choice of n_e as by the choice of θ (Vourlidas et al., 1997). Then, by using a range of values derived from previous studies, realistic results should be obtained. In the ensuing analysis, the differences from using the various densities are minimal, confirming that the results are not very dependent on density. A pixel is set to be optically thick if $\tau > 0.9$ in the calculations.

The results of the optical depth calculations in terms of area coverage are now explored. Figure 3.13 displays the optically thick pixels (grey) for both o and x modes for $s = 2$ and 3. The $s = 4$ layer is nowhere optically thick so it is not displayed. The 400 G contour from the radio derived $s = 3$ map is displayed as it outlines the edge of the gyroresonance source. Some MDI contours are also included as a reference. The calculations show the expected structure (White, 2004) as follows: there is a window above the sunspot center where only the $s = 2$ x-mode layer is optically thick, the $s = 3$ layer covers a larger area than the $s = 2$ layer because it comes from lower magnetic fields at higher altitude, and the $s = 3$ o-mode layer is optically thick only at particularly inclined angles and so it has a wider window of optically thin pixels over the sunspot center.

Figure 3.14a shows the total area covered by optically thick pixels with the same reference contours. The areas where the radio spectral fitting returns a gyroresonance signature, but the calculations do not yield optically thick pixels, are labeled

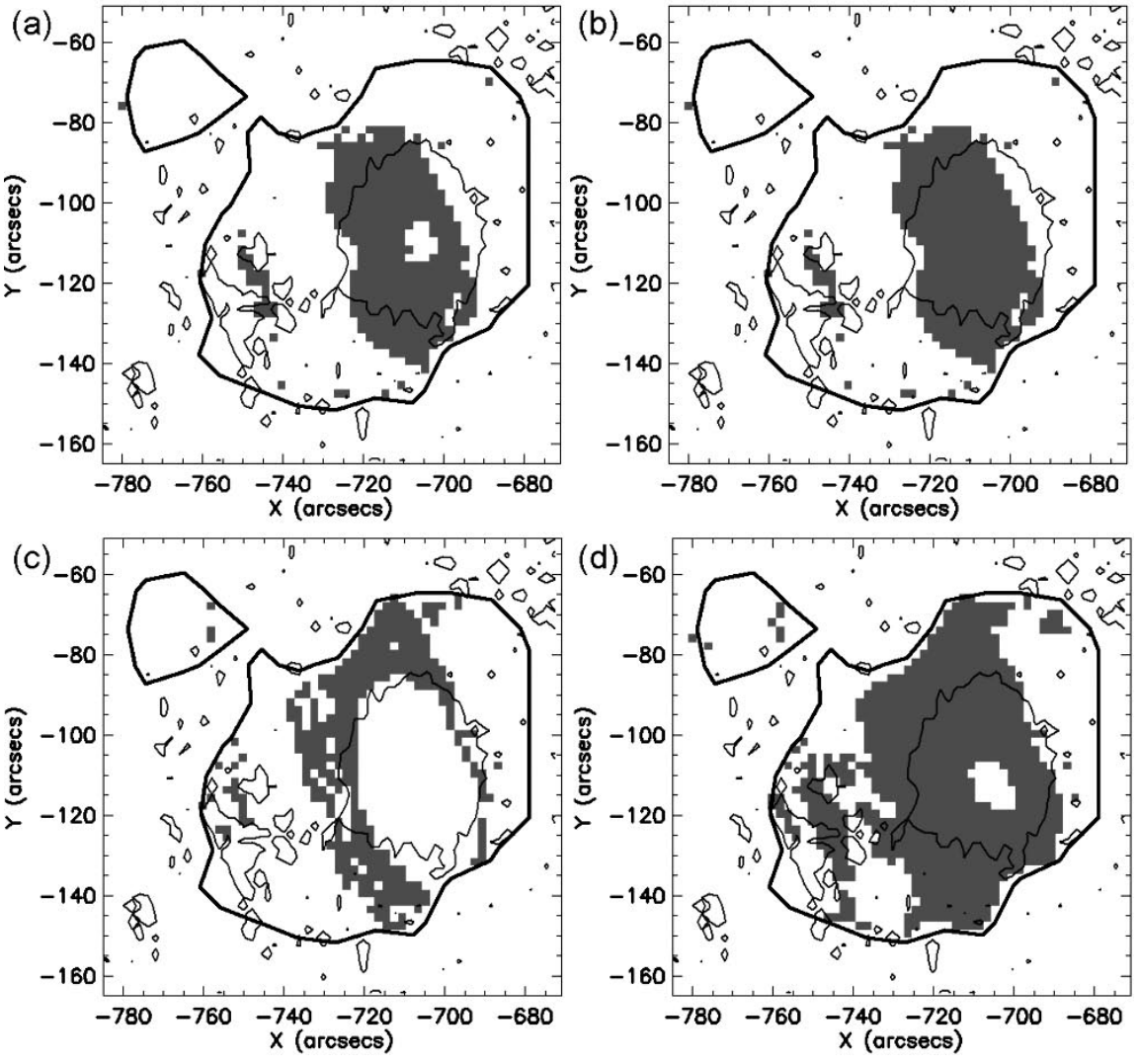

Figure 3.13 Optically thick lines of sight (grey) for the various gyroresonance layers, as determined from calculations with radio data. The 400 G contour from the radio-derived $s = 3$ $B_{\rm tot}$ (black) and the $(-600, 500)$ B_z contours are included for reference (gray): (a) $s = 2$, o-mode, (b) $s = 2$, x-mode, (c) $s = 3$, o-mode, and (d) $s = 3$, x-mode.

A-*D*, and can be considered regions where the extrapolation is not consistent with the radio observations. It is interesting that these regions are also the locations of temperature peaks in the gyroresonance T_e distribution, as seen in Figure 3.14*b*. Figure 3.15 displays spectra from each of the labeled locations *A*-*D*. These spectra display a clear gyroresonance signature, ensuring that the derived B_{tot} values are real. Further inspection reveals that the discrepancy occurs because the extrapolation does not contain high enough magnetic field strengths along these lines of sight to match those derived from the radio spectra. While the method shows that the extrapolation is able to match observations along many lines of sight, the derived T_e distribution is now used to further explore the areas where there is a discrepancy.

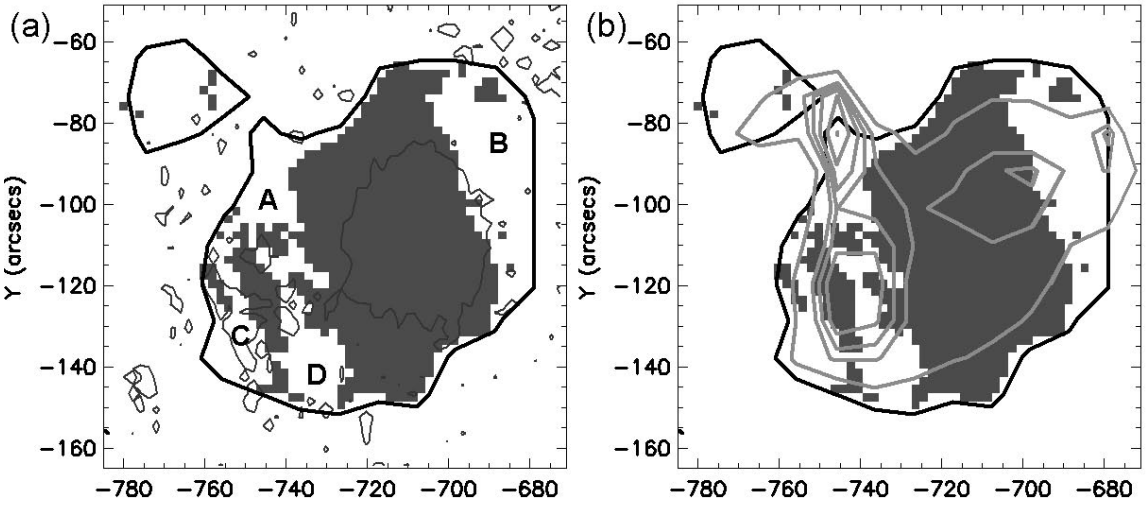

Figure 3.14 (*a*) Total area covered by optically thick lines of sight –a combination of pixels in Figure 3.13, (grey), with other contours as in that figure. The areas labeled *A*-*D* are regions where the extrapolated *B* field is too low to match that derived from the radio spectra. (*b*) Gyroresonance-derived T_e distribution in the same field of view. The locations of the T_e peaks coincide with (A,C,D) or straddle (B) the regions of discrepancy.

3.4 Location of Inferred Coronal Currents

A comparison of the gyroresonance component's T_e distribution with X-ray data from XRT shows that the peaks in temperature correspond to the foot points of

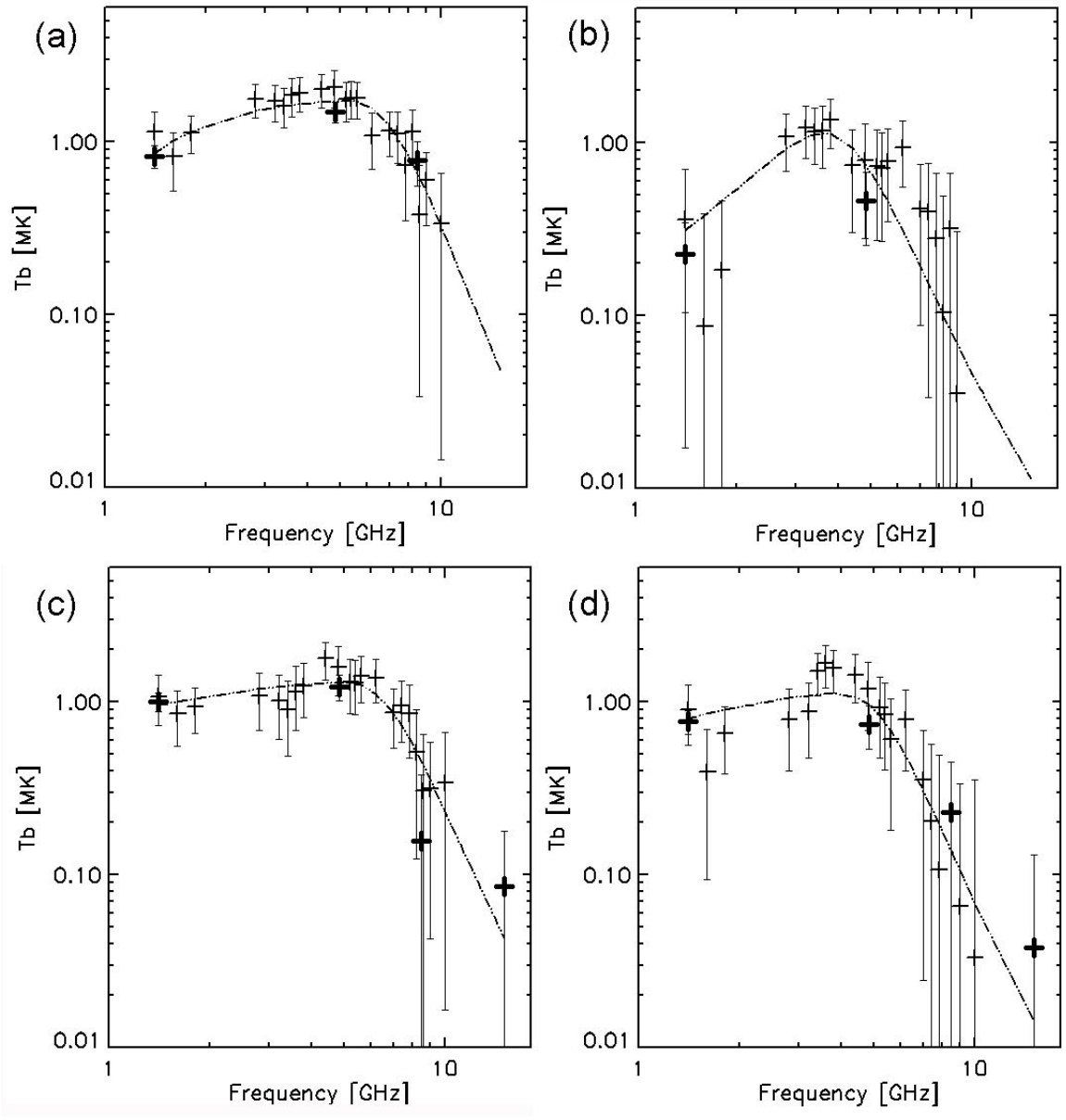

Figure 3.15 OVSA (+) and VLA (bold +) spectra corresponding to the labeled points in Figure 3.14*a* along with the fit's two-component model (dashed) and corresponding rms error bars: (*a*) spectra for location *A*, (*b*) location *B*, (*c*) location *C*, and (*d*) location *D*.

X-ray loops. In turn, these X-ray loop footpoints lie directly over the penumbra (Figure 3.16a). When considering the map overlays in these figures it is important to keep in mind that the AR is at $\sim 49E$ longitude and projection effects will make the forward loop component appear to overlie the leading part of the umbra. Other workers have reported this effect (i.e. Vourlidas et al. 1997 and references therein). The existence of very hot, X-ray emitting plasma, coinciding with the peaks of the gyroresonance temperature at the base of the corona, in regions where the observed magnetic field strength is higher than that in the extrapolation, imply that these are regions with an increased heating function where coronal currents raise the magnetic field above potential-state values.

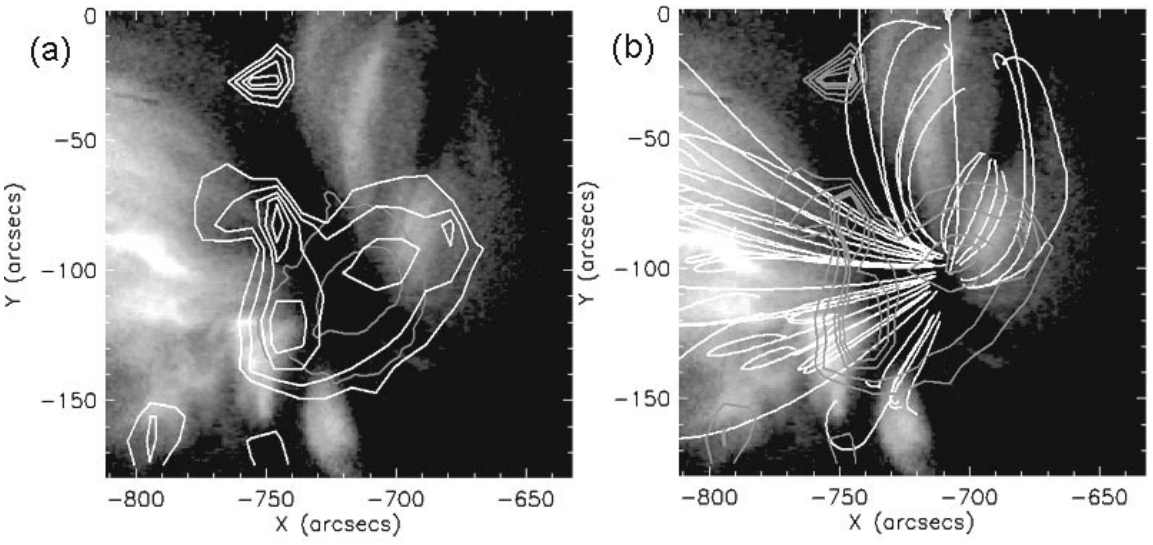

Figure 3.16 XRT's Al-med filter data overlaid with (a) the white-light umbral and penumbral boundaries (gray) and the gyroresonance T_e (white) and (b) the same T_e (now grey) with field lines (white) corresponding to X-ray emission. Field line matching is discussed in section 4.1.

The finding that a two-component free-free and gyroresonance model best fits the radio spectra returns a stratified view of the corona above AR 10923. Specifically, the free-free emission is associated with the tops of long loops, while the gyroresonance emission comes from the legs or foot point of loops converging onto the sunspot region. In addition, maps of the emission measure for the free-free emission and the

total magnetic field at the base of the corona are derived. The boundary condition for a current-free extrapolation was optimized through a combination of data from the MDI and SOT instruments. This resulted in a magnetic field model that agrees with the loop configuration observed in EUV and X-ray data. Analysis with this extrapolation shows that the derived physical parameters yield the expected results from optical depth calculations. These calculations, in turn, point to the co-location of areas where the model and observations differ with the foot points of hot X-ray loops. Since gyroemission is observed over the entire sunspot region, the differences between the areas of congruence and of discrepancy warrant further exploration. This analysis is undertaken in the following chapter.

CHAPTER 4
IMPLICATIONS FOR THE ATMOSPHERIC STRUCTURE ABOVE AR 10923

There are two main results from the model fitting: (1) that the corona, as seen through radio observations, can be modeled as two stratified layers, the lower one of which is dominated by gyroresonance emission while the higher one emits via free-free emission, and (2) that the base of the corona is not uniform in temperature nor magnetic field strength, with the hottest areas also exhibiting magnetic field strengths above those expected from a current-free state. These results can be used in conjunction with other data to explore the three-dimensional configuration of the corona. In the following discussion, these results are used to obtain such information.

4.1 Thermal Free-free Emission in the Corona

While it is not expected that the transition from the gyroresonance to free-free dominated regime is abrupt or co-planar, the changeover provides restrictions on the temperature and density distributions along coronal loops. As can be seen in Figure 3.9*b*, the free-free emission dominates at the tops of certain loops, and gyroemission corresponds to the legs or foot points. During an effort to understand the conditions in this configuration, it was found that the free-free emitting loops do not appear different in length or shape from some non-emitting loops in the extrapolation. Hence, they must differ from the non-emitting loops due to some other factor, such as the location of their foot points. This might come about due to the variations in the heating function at the base of the corona over the entire AR. It also implies that different loop systems can be associated with different combinations of emission mechanisms.

Rosner et al. (1978) found that, for loops in hydrostatic equilibrium, the temperature maximum is near the loop apex. Because of the stability of the region's photospheric magnetic field and coronal EUV and X-ray loop configuration throughout

the observation day, this condition may be considered a valid approximation for AR 10923. Based on this assumption the observed radio and X-ray free-free emission are identified as emanating from two distinct loop systems. To identify the radio free-free loop system, an arbitrary but reasonable minimum temperature of $T_e > 0.9$ MK is chosen to denote peak coronal temperatures and only those loops whose mid-points lie within this temperature contour are selected and plotted (Figure 4.1*a*). A comparison of these radio loops on the XRT map (Figure 4.1*b*) shows that, while some of these loops coincide with diffuse X-ray emission, particularly obvious in the Southern-most loops, the brightest X-ray signatures lie below these loops. Similarly, X-ray emitting loops are identified as those whose tops are co-aligned with the brightest X-ray free-free emission from the Al-med XRT filter (Figure 4.1*c*). A comparison of these loops to to the radio's temperature criterion (Figure 4.1*d*) shows that the tops of only a few of the longest of these X-ray loops lie within the 0.9 MK contour. These comparisons demonstrate that while there is some overlap in emission from both radio and X-rays, as would be expected because both wavelength regimes are a produced by the same emission mechanism, the bulk of the emission coincides with the loop tops from two different loop systems. Why, then, should the different loop systems be dominated by free-free emission at the two different wavelengths?

Having associated radio and X-ray free-free emission with different loop systems, the extrapolation is used to create a model schematic of the field line configuration. The diagram displayed in Figure 4.2*a* shows the configuration as seen from solar North. Here field lines matching the radio source are in blue and the ones matching the X-ray sources are in red. The X-ray associated field lines have a wide range of loop lengths and heights, and surround the sunspot. The field lines responsible for the bulk of the radio free-free emission reach greater heights than the X-ray loops, and all have positive-flux foot points in the farthest portion of the plage *East* the sunspot. The distance between foot point locations of the tall radio loop and the

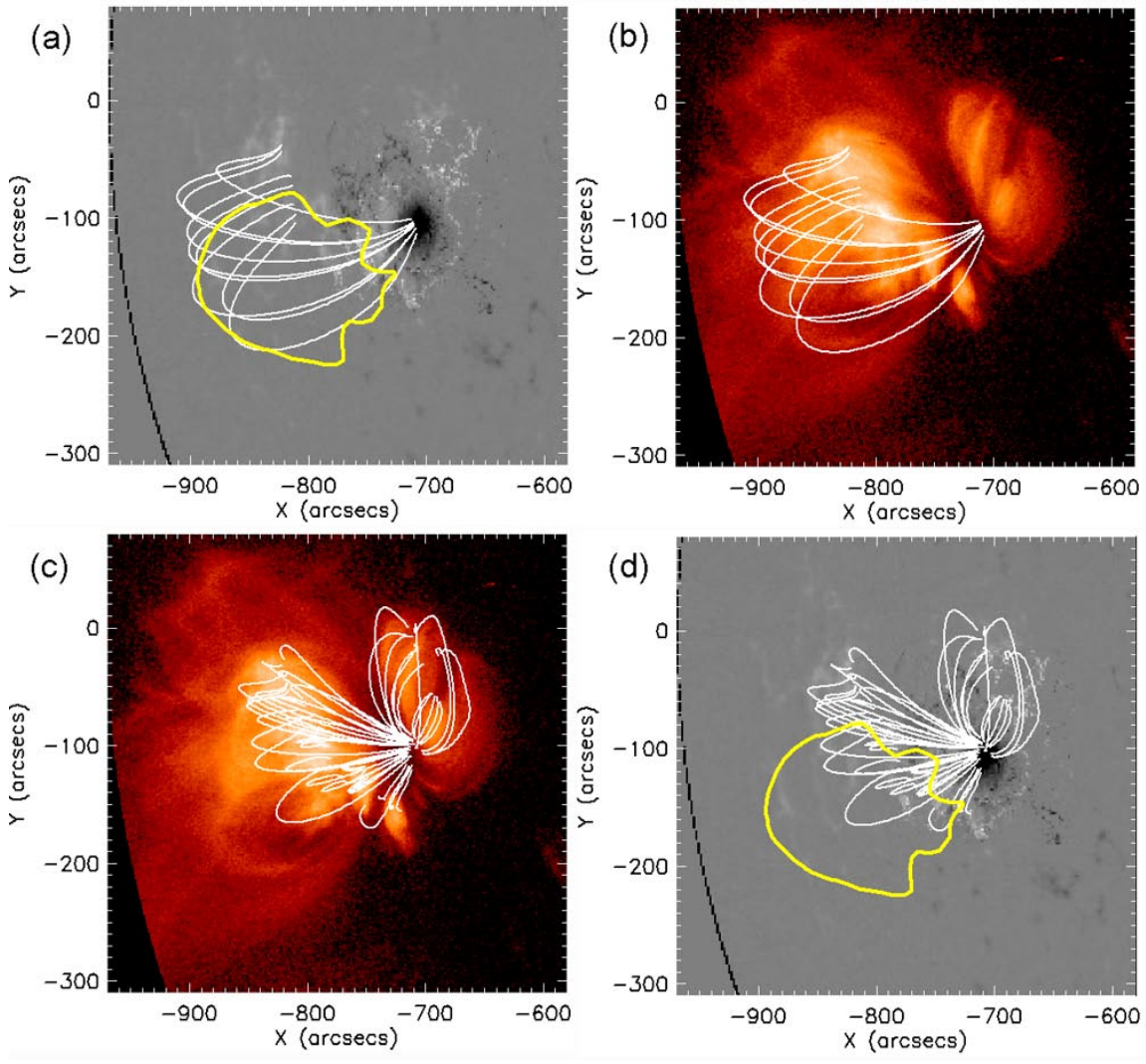

Figure 4.1 Field line matching to emission source: (a) field lines whose loop tops coincide with radio free-free emission at $T_e > 0.9$ MK (yellow), (b) the radio source matching field lines overlaid on X-ray data (Al-med) from XRT, (c) field lines with loop tops within the brightest X-ray free-free emission from the same filter, and (d) the X-ray matching field lines overlaid with the same radio T_e contour as in (a). There is some diffuse cross emission between both loop systems.

shorter X-ray loop foot points in this far plage region was found to be minimal, with separations of only a few arcseconds at some locations. Negating the possibility that the height of the loop is a condition for association with radio emission, the diagram also shows field lines of equal length and height as the radio emitting loops, in black, that show neither radio nor strong X-ray emission. The difference, then, must lie in the location of the foot points and associated heating. Figure 4.2*b* displays the image-plane view of the two loop systems, showing that the radio loops converge to a point inside the nest made by the X-ray loop foot points.

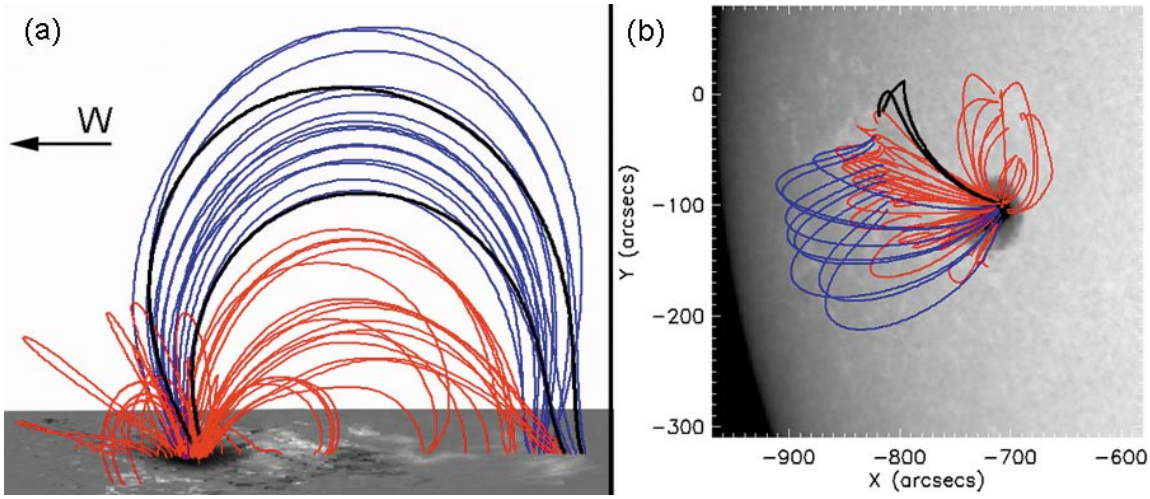

Figure 4.2 Schematics of the distribution of the X-ray (red) and radio (blue) emitting groups of loops, and non-emitting field lines in black : (*a*) as seen looking *S* from solar *N*, and (*b*) overlaid on the MDI continuum map as observed in the image plane. Note the differences in height and foot point locations.

As discussed in section 3.4, the available observations show that the X-ray foot points are anchored in the penumbral region. Therefore the free-free loops fall within the umbra. This means that the foot points of the X-ray emitting loops are associated with the outer portions of the radio-derived $T_{e,gyro}$ and $B_{\rm tot}$ distributions at the base of the corona, discussed in section 3.2.4. Closer to the center of those distributions are the foot points of the radio associated loops, which are dominated by the gyroresonance mechanism because of the increase in magnetic field strength.

Within the extrapolation, field lines emerging directly from the peak of the photospheric magnetic field reconnect to the plage areas far *East* and *North* of the sunspot and are associated with a dark X-ray corridor extending diagonally to the $North - East$ from the sunspot (see, for example, Figure 4.1*b* to see this darkened region). Many workers have reported the detection of cooler material over sunspot umbrae than in the surrounding corona (i.e. Foukal et al. 1974; Felli et al. 1981; Kundu et al. 1981; Alissandrakis & Kundu 1982). Other results have suggested that umbral loops may extend to higher altitudes and are filled with cooler plasma (Gary & Hurford, 1987; Vourlidas et al., 1997). Vourlidas et al. (1997) found that observed polarization in VLA data could be accounted for only if the umbral and penumbral loops formed two distinct systems with different densities and temperatures, heated by varying heating rates at their foot points. The implication of these results and the conclusion from the analysis just described is that the field lines reach a peak temperature that depends on the foot point location within the sunspot region, with temperatures varying greatly between very closely spaced foot point locations, even within the umbra. The X-ray loops may have the density required for free-free radio emission, but may be too hot for emission to be optically thick at radio wavelengths because of the dependence of the optical depth on $T_e^{-3/2}$ (Eq. 1).

4.2 Implications for the Emission Measure Distribution

Radio emission at low frequencies and X-ray emission are produced by the free-free process. The difference arises from the kinetic temperature of the electron population producing the emission (high for X-rays, lower for the longer radio waves) and the consequent difference in impact parameter in the Coulomb interactions. X-ray data can be inverted to obtain an estimate of the coronal temperature and emission measure, and these parameters can be directly obtained from the radio observations, as described in Chapter 1. Based on the assumption that the X-ray and radio emission

arises from different wings of the same thermal distribution, there have been many attempts at comparing these quantities as derived from both wavelengths (Webb et al., 1987; Nitta et al., 1991; Schmelz et al., 1992; Brosius et al., 1992; Lang et al., 1993; Klimchuk & Gary, 1995). The majority of these studies report that the temperature estimated from X-rays is consistently higher, about twice that obtained from radio data, and agreement is found by invoking the presence of cool (10^5 K) intervening material. One exception the values derived from X-ray and radio data agree is Gopalswamy et al. (1991). Comparison of the emission measures are found to be incompatible as well.

The proposed separation of X-ray and radio free-free emission by loop system presents a plausible explanation for the differences in plasma temperature and emission measure from the two energy regimes. Namely, a straight-forward comparison is not always possible because the X-ray and radio wavelengths are emitted from two different loop systems and do not necessarily represent the same set of temperatures and emission measures. In addition, the association of the free-free radio emission with a particular loop system points to an explanation, discussed next, for the derived two-dimensional emission measure distribution which, as discussed in section 3.2.4, does not appear to correspond to features observed at any wavelength.

The emission measure, defined in Equation 1.3, is the integral along the line of sight of the density squared. Thus it is weighted by the density, although the dependence on path length is not easily removed. In the previous section it was determined that free-free emission dominates at the tops of certain loops while gyroresonance is responsible for the emission near the foot points. Since plasma transport across field lines is inhibited in the low-β corona, as these loops converge the density should increase, increasing the EM if the path length does not vary at a rate faster than the increase in n_e^2. The increase in EM would not be observed beyond the region along the converging loops where gyroresonance absorption takes over. The peak of the

derived EM distribution should then overlie the region of increasing density along the converging radio-emitting field lines at heights where the dominating emission mechanism is still free-free. That this configuration is reasonable can be seen in the co-location of the converging radio loops with the EM peak, as shown in Figure 4.3.

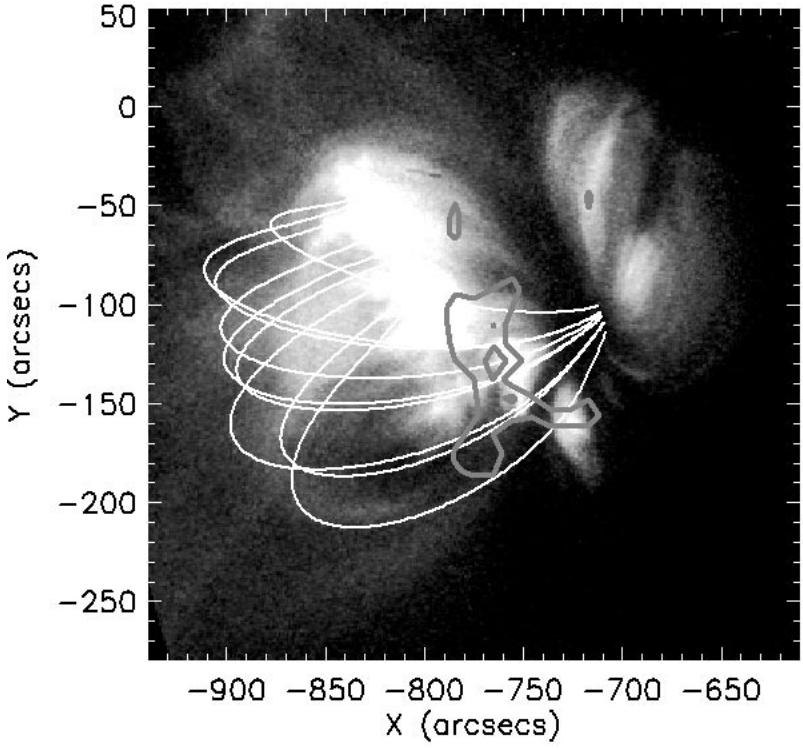

Figure 4.3 Field lines correlated with free-free radio emission and the derived emission measure distribution levels 60 and 120 $\times$ 10^{27} cm^{-5} on XRT's Al-med filter map.

In summary, the assumption of loops in hydrostatic equilibrium lead to the association of radio and X-ray emission with two distinct loop systems. These loop systems differ in the location of their foot points and presumably also differ in the associated heating function. The X-ray loops are anchored in the penumbra, where radio-derived temperatures show a peak and the observed magnetic field values are higher than those from a current-free extrapolation. The radio loops have foot points within the umbra, in regions of slightly cooler temperatures and increased agreement with the extrapolation. The overall implication of this configuration is that the

sunspot dominates the temperature and emission behavior of the entire active region, its reach extending tens of thousands of kilometers above the photosphere and around the sunspot. The confinement of the bulk of the radio emission to the tops of certain loops also presents a plausible explanation for the differences in the temperatures and emission measures derived from X-ray and radio observations. That is, such comparisons are not straightforward because the two emissions arise from two distinct loop systems. This view also presents an explanation for the radio-derived emission measure distribution. Having used the results of the radio analysis, in conjunction with the extrapolation, to explore their implications for the corona, in the next chapter attention is turned to an analysis of one of the lowest regions of the solar atmosphere, the transition region.

CHAPTER 5

ON THE TRANSITION REGION

Radio observations alone, or from any single wavelength regime for that matter, can not generally provide direct information about their source heights. The possible exceptions to this are limb observations and stereoscopic studies. In limb observations, the geometry lends itself to the derivation of the height distribution in the image plane but not along the line of sight. Stereoscopic studies, in which the height of radio sources is geometrically determined from changes in the aspect angle throughout multi-day observations, must assume that the target AR is stable throughout the entire observation time. Often, a combination of these techniques is used to determine source height. Concerning gyroresonance dominated frequencies, Alissandrakis and Kundu (1984) determined a height of 1×10^4 km at 4.87 GHz, while Lang et al (1982) found twice the height (2×10^4 km) for their 5 GHz source, and Shibasaki et al (1983) obtained a height of 6×10^3 km for a 4.7 GHz source. At a higher frequency, Lee at al (1993) determined a height of 5.2×10^3 km for a 7.2 GHz gyroresonance layer. At even greater frequencies, Aschwanden et al (1995) found heights of 3.3×10^3 km to 1.1×10^4 km for 10 to 14 GHz sources. Gyroresonance sources, then, occupy the first 5-10 thousand km of the solar atmosphere, with height generally increasing with decreasing frequency (for a possible exception see Aschwanden et al 1995). These studies have produced typical height estimates of the centroids of entire source regions, but none have attempted the mapping of height of the emission as a function of position over an entire AR. The high-quality spectra and the type of analysis and model fitting developed in this thesis presents a unique opportunity to demonstrate an approach by which this can be done. The purpose of this chapter, then, is to outline the method by which the results of the spectral analysis of the radio data and the subsequent comparison to the magnetic

field extrapolation can be used to obtain the three-dimensional temperature distribution in height from the coronal base through the transition region down into chromospheric temperatures, $T_e(x, y, h)$.

5.1 Principles of the Method

Since the high frequency fall-off of brightness temperature in gyroresonance spectra begins at the frequency emitted by the last optically thick layer at coronal temperatures, the slope conveys information from the base of the corona and the underlying transition region where the temperature falls to chromospheric values. The result of the analysis of the gyroresonance component described in section 3.2 returns the magnetic field at the base of the corona. The gyroresonance emission from the emitting region must be optically thick in order to be observed $T_b = T_e = T_e(B_{\tau=1})$, where $B_{\tau=1}$, given by equation 1.4, is the magnetic field at the location where the model parameter τ (which is not the optical depth of the emitting material) is equal to unity. However, equation 1.4, from which the above relationship was derived, holds for any frequency where the emission is due to the gyroresonance process, not only $\nu_{\tau=1}$. The spectrum, then, represents $T_e(B(\nu))$ for all ν where gyroresonance emission dominates. This condition is guaranteed for all frequencies along the slope of the gyroresonance spectra, so long as the emission is optically thick. At each frequency along the spectrum the magnetic field matching the resonance condition for the observed emission occurs at a specific but unknown height h above the photosphere. If the height distribution $B(h)$ were known, the spectra could be inverted to derive the temperature distribution as a function of height $T_e(h)$. Such an analysis carried out over all lines of sight where there is a gyroresonance component would yield $T_e(x, y, h)$, where x and y are the usual heliocentric coordinates. Knowledge of this distribution is valuable in the investigation of the transition region, where there is a known temperature discontinuity of several million degrees (Stix 2004).

Magnetic field extrapolations provide $B(h)$, although some caveats must be considered when using this information. If the true $T_e(x, y, h)$ is to be derived, the extrapolation must exactly represent the coronal $B(h)$ for every line of sight. As was shown in section 3.3 and by other researchers (i.e. DeRosa et al 2009 and references therein), extrapolations of solar magnetic fields have limitations. However, the limitations of the extrapolation only limit the scope of the resulting distribution and not of the demonstration of the method itself. This study has shown that the potential field extrapolation used matches the expected field values obtained from the radio observations (Figure 3.14) over the majority of the lines of sight exhibiting gyroresonance emission. Ideal T_b spectra, such as the model spectra of Figure 2.11, would be analyzed in each polarization, not in total intensity as done in this study. As described in section 2.3, this has the effect of reducing the steepness of the high-frequency slope from that of the polarization spectra. In addition, all T_b spectra from this data set are well fit by a gyroresonance model with a single, idealized frequency dependence given by equation 3.1 with $\tau_{gyro} = 1$. While the turnover frequency is different for the various lines of sight, our fits fix the slope as ν^{-5}. Having the same slope certainly masks more subtle temperature variations in frequency, and therefore height, that better data might exhibit. Nevertheless, the methodology is applicable to gyroresonance spectra of any shape, and leads to some interesting result even for this limited data set.

5.2 Implementation of the Method

The method of obtaining $B(\nu)$ and the appropriate harmonic is the one outlined in Chapter 3 for the frequency $\nu_{\tau=1}$ where the τ parameter of the gyroresonance model becomes unity. Because the fitted model is of known form, the temperature at any frequency can be directly obtained from the model. Equation 1.4 is then used to calculate the magnetic field strength $B_{\rm tot}$ for the s= 2, 3, and 4th harmonics of that

frequency. The data cube containing the extrapolation is first rotated and aligned with the observed image plane, and is then searched along the corresponding line of sight for the magnetic field value that matches one the three assigned from the spectral analysis. At the locations matching a harmonic's field strength, the optical depth is calculated as described in section 3.3. This is done for all harmonics and the optically thick harmonic layer closest to the observer is set to be the observed harmonic, since all are emitting at the same frequency. The height of this gyroresonance layer is recorded once the $B_{\rm tot}$ match is found. It is therefore at this height that the temperature obtained from the spectrum for this frequency is appropriate, resulting in the desired $T_e(h_1)$, where h_1 is the height of this single frequency layer. The same procedure is repeated at other frequencies along the same spectrum to derive $T_e(h)$ for this line of sight. By carrying out the same analysis for each line of sight with a gyroresonance component the $T_e(x, y, h)$ from the base of the corona down towards the chromosphere is finally obtained.

Upon performing this procedure on this data set, it was found that the frequency separation of the points to consider is limited by the resolution of the potential field extrapolation used. Because the pixel resolution of the photospheric B_z map from which the extrapolation was created is 1.98″x 1.98″, the same vertical resolution was used. This is a reasonable value since complexity in the resulting model is limited by the input magnetogram. At the heights at which the extrapolation and radio-derived magnetic field strengths match, the field strength in the model increases very quickly towards the photosphere. The gradient is so steep that the heights of the magnetic field strengths corresponding to different frequencies are often within the same extrapolation z-layer pixel. This issue is addressed by increasing the line of sight resolution of the extrapolation with a spline fit with 1/4 the original resolution. This increase in resolution is sufficient to separate out layers from a modest frequency

interval, as will be shown later, while increasing it further provides no greater insight from this particular set of spectra.

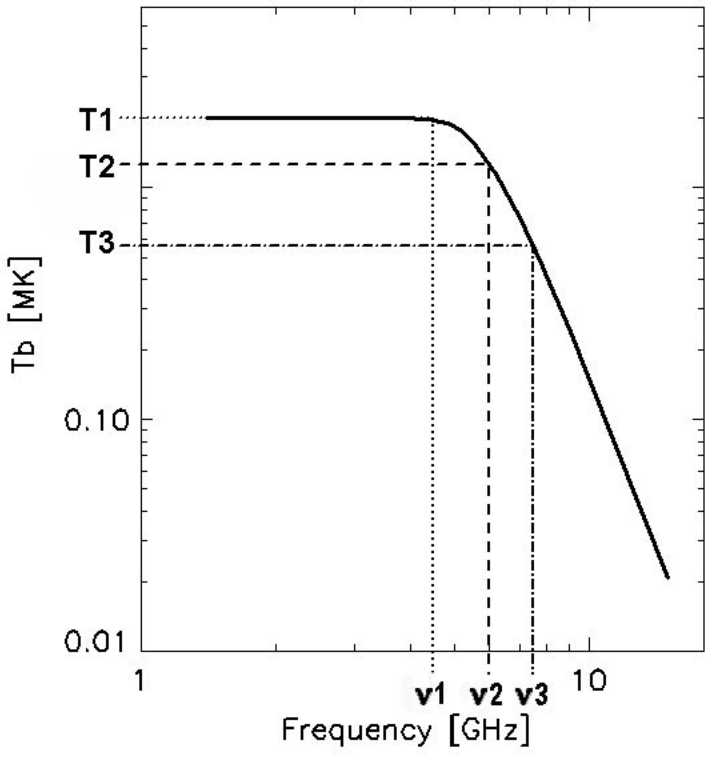

Figure 5.1 Example gyroresonance spectrum showing the frequency intervals used in the calculation of $T_e(x, y, h)$. The $\nu 2$ frequency marks where the model's τ parameter becomes unity, while $\nu 1 = \frac{3}{4}\nu 2$ and $\nu 1 = \frac{5}{4}\nu 2$. T1, T2, and T3 are the temperatures corresponding to $\nu 1$, $\nu 2$, $\nu 3$, respectively. These proportions depict the intervals used in the analysis, as described in the text, while the values for the various spectra vary.

Three equidistant frequency points along each spectra are chosen at which to carry out these calculations. The frequency proportions used are displayed in Figure 5.1, denoted by the labels $\nu 1$, $\nu 2$, and $\nu 3$. The frequencies are relative to that at which the model's τ parameter equals 1. In this figure that frequency is relabeled as $\nu 2$, here at 6 GHz, and at this location the spectrum returns a temperature $T_e = T1 * (1 - e^{-1})$. $T1$ is the coronal temperature in this representation, here chosen to be 2 MK, which is on the high end of the temperature values in the radio data. At the frequency $\nu 1 = \frac{3}{4}\ \nu 2$ the corresponding temperature is T1. On the

other side of $\nu 2$, the spectrum at the frequency $\nu 3 = \frac{5}{4}\ \nu 2$ has a corresponding temperature of $T_e = T1 * (1 - e^{-\frac{1}{1.25^5}})$. Since each spectrum has its own values for T1 and $\nu 1$, the actual values of each frequency used are different, but the proportions are kept the same. Once the calculations of $T_e(h)$ have been carried out for the three designated frequencies over all pixels with gyroresonance spectra, the resulting three-dimensional maps are de-rotated back to the original sunspot-centered frame to investigate the results relative to the solar surface.

A top view of the results of these calculations is displayed in Figure 5.2 over the de-projected B_z map for reference, with all axes in units of arcseconds. The resulting layers have been minimally smoothed in the visualization volume for aesthetic purposes and blue, red, and green color scales have been used to present the surfaces corresponding to the $\nu 1$, $\nu 2$, and $\nu 3$ steps, respectively. The color scales also reflect temperature variations on each surface, the hotter regions being lighter while the cooler ones take on darker shades. A comparison with Figure 3.14 shows the match expected between both calculations, taking into account the effects from viewing the AR from a different viewing angle. Figure 5.3 shows rear perspective views of all three surfaces in panels (a), (b), and (c), while panel (d) shows the layers superposed on each other, demonstrating the stratification of the transition region. It is important to restate that the $\nu 2$ surface depicts the shape and height of the base of the corona, as derived from the height values obtained from the extrapolation, and the $\nu 1$ and $\nu 3$ surfaces depict the temperature distribution at equidistant frequency intervals above and below the coronal base, corresponding to coronal and transition region temperatures, respectively. These are neither isothermal nor isogauss surfaces, and their importance lies in their location in this very important region of the solar atmosphere. Keeping in mind the limitations of the potential-field extrapolation, an analysis of these results is now discussed.

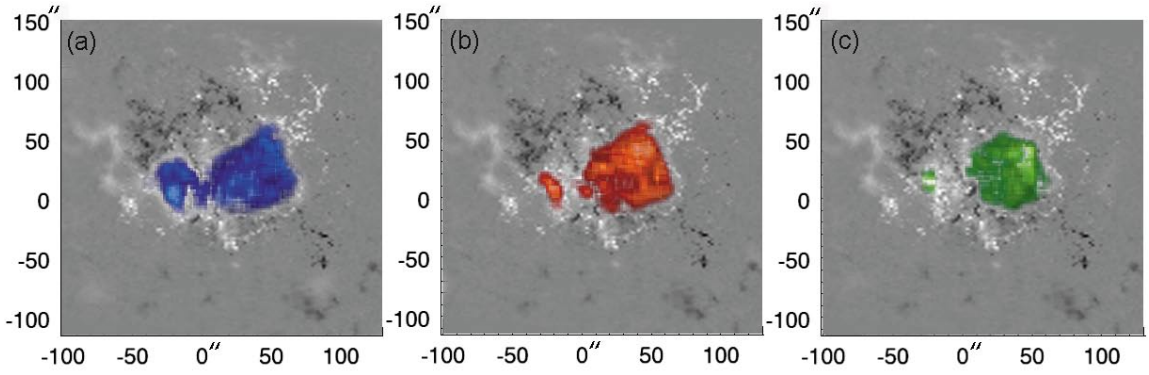

Figure 5.2 Surfaces depicting the temperature distributions on the layers corresponding to the (a) $\nu 1$, (b) $\nu 2$, and (c) $\nu 3$ frequency intervals. The axes are in units of arcseconds from the approximate center of the AR with solar *North* pointing up.

5.3 Results of the Method

In section 3.3 it was shown that the potential-field extrapolation fails to match the radio derived magnetic field strengths in regions coincident with X-ray loops. Coronal currents in these regions can raise the actual magnetic field strength in these regions above potential state values, causing a local change in the magnetic field distribution. That the extrapolation used is not a bad approximation over much of the region may be inferred from the well-matched current-free and X-ray loops in Figures 3.3b and 4.1. In addition, since magnetic-field strength matches were found over large portions of the coronal base (Figure 3.14), this is an indication that at least in these regions the potential and true magnetic field distributions are in a reasonable level of agreement. Hence, while the entire three-dimensional distributions derived here should not be used for a quantitative analysis of the transition region, there are some general features that should be pointed out, restricting the discussion to regions of agreement.

The lowest layers of all three surfaces are within the lowest extrapolation layer, which corresponds to 1.6″above the photosphere. The lowest point occurs near the neutral line, where the radio data report a temperature peak. Over the umbra, the $\nu 3$

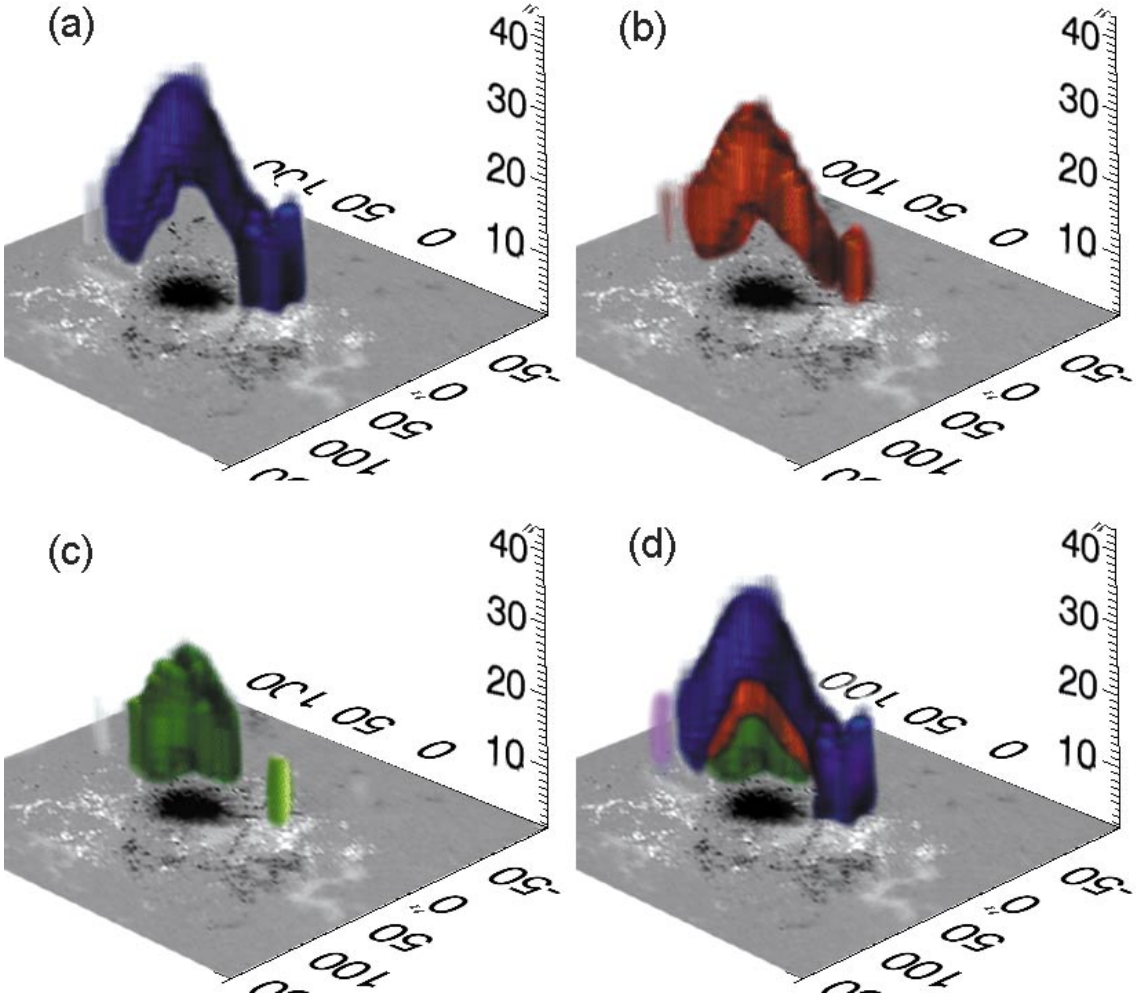

Figure 5.3 Temperature distributions of the same layers as in Figure 5.2, at an angled view from the $North - West$ corner. The blue, red, and green color scales correspond to the (a) $\nu 1$, (b) $\nu 2$, and (c) $\nu 3$ frequency intervals, respectively. Panel (d) shows the superposition of these surfaces, demonstrating the stratification of the transition region as derived from the analysis. The surfaces share heights above the positive (white) photospheric flux, while the greatest separation between them occurs at the greatest heights reached, directly over the sunspot umbra. The vertical scale has been exaggerated to improve visualization.

surface reaches a height of 19.5″. At the Sun, 1″ ≈ 725 km, so the range spanned by this lower surface is 1.15x10^3 km to 1.41x10^4 km. The temperatures covered by this surface range from 1.5x10^{-3} MK to 6.5x10^{-1} MK. The peak height corresponding to the $\nu 2$ surface is 29.4″ (2.1x10^4 km) with a temperature range of 1.5x10^{-3} MK to 1.5 MK . For the $\nu 1$ surface these values are 35.3″(2.5x10^4 km) for the height above the umbra and 8.7x10^{-3} MK to 2.3 MK for the temperature. The frequency range of optically thick matches is from 4.4 to 14.1 GHz, indicating that the height values are in very good agreement with those obtained from the studies mentioned in the introduction to this chapter. These values demonstrate the height variations seen in figure Figure 5.3, in which the vertical scale is exaggerated to make the height variations clearer. A view of the calculated surfaces in correct proportion to their lateral extent is shown in Figure 5.4. At these proportions, the surfaces appear almost colocated, although the rise in height over the umbra is still obvious. The height variations also indicate that the transition region, often regarded as extremely spatially thin because of the sharp discontinuity in temperatures, is highly variable in height across the AR, although generally thin. The point of greatest separation between the surfaces is only above the sunspot, with height differences of up to 15.8″ while the minimum height differences elsewhere are less than the pixel resolution of 1.98″.

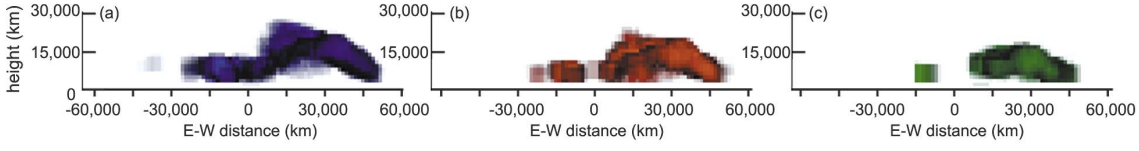

Figure 5.4 View from solar *South* of the the temperature distributions on the layers corresponding to the (a) $\nu 1$, (b) $\nu 2$, and (c) $\nu 3$ frequency intervals, demonstrating the variation in maximum height and surface size. The vertical and horizontal scales are now in proportion.

The region low in the corona where there is a temperature peak near the neutral line (Figure 3.14) also corresponds to the umbral/penumbral border closest to the neutral line between the strong negative polarity umbra and the strongest patch of positively directed magnetic flux. It is also near this location that a large portion of the X-ray loop footpoints converge (Figure 3.13b) and the single harmonic B_{tot} peak is located (Figure 3.8). At this location, then, one would conclude that the corona dips to low heights to a region of increased heating. Over the umbra, the situation is reversed. The cool temperatures of the $\nu 3$ surface indicate that there is a volume of cool material directly over the sunspot, a feature inferred by previous workers using different techniques (i.e. Foukal et al. 1974; Felli et al. 1981; Kundu et al. 1981; Alissandrakis & Kundu 1982). Section 4.1 presented arguments showing that hot, X-ray loops have foot points in the sunspot penumbra, and slightly cooler radio loops have foot points just within the umbra. The field lines converging directly onto the center of the umbra, where the photospheric magnetic field is the strongest, are cooler, as inferred from the lack of associated radio or X-ray emission. Considering the results of the transition region mapping just presented, the radio and non-emitting loops have foot points over the core of cool material directly over the sunspot umbra, between the chromosphere and coronal base. This result explains the differences between the heating functions operating above the umbral and penumbral regions in AR 10923.

The shape of the $\nu 2$ surface also explains why the peak of the radio derived magnetic field is displaced from the peak of the photospheric field at the center of the sunspot (Figure 3.11). The material above the umbra remains at sub-coronal temperatures to greater heights, reaching coronal temperatures where the strength of the magnetic field has considerably decreased. The magnetic field values derived from the radio spectra correspond to the base of the corona, which drops considerably in height towards the neutral line, close to the area of strongest positive magnetic flux.

It is therefore at this location that strong field lines combine with coronal temperatures to produce observable gyroresonance emission at greater frequencies, reporting a peak in the magnetic field strength. Another feature of the three-dimensional mapping is that the surfaces decrease in size with increasing frequency, a known behavior of source sizes in individual frequency maps, as shown in Figure 3.6. That the combined analysis of radio data with the extrapolation returns this trend is an additional attestation to the strengths of the technique.

This demonstration of method yielded some interesting results, mostly the stratification of the transition region, but also the determination of the existence of a core of cool material over the sunspot umbra. This finding, in turn, presents an explanation for the different heating functions in the umbra and penumbral regions, as determined from the work in Chapter 4. If such features are verified by further observations of other ARs, it may be found that this configuration is a general feature of the umbral-penumbral-plage transition. A similar study carried out with better imaging and reliable polarization data might reveal the subtleties of interplay between the harmonics. Such data would justify a more concrete numerical analysis. Regardless, the good-quality joint OVSA-VLA data have afforded a demonstration of the method, providing a preliminary mapping out this important region in three dimensions. Here, the information not directly derived from observations is the angle between the magnetic field and the line of sight at the height where the field strengths match, both of which are obtained from the extrapolation. In this regard, the method just presented can be used in an iterative process of improving the parameters of a NLFF magnetic field extrapolation that allows for currents to exist in the corona. Further investigation of the lower solar atmosphere can also be sought through stereoscopic methods, which may afford independent measurements of height as a function of frequency, as demonstrated by Aschwanden (1995). Such future work will be important in accurately determining the morphology of the transition

region and the base of the corona, further explaining the mechanisms that create and maintain the observed structures.

CHAPTER 6

CONCLUDING REMARKS

This dissertation has been driven, since the beginning, towards the goal of a three-dimensional mapping of the corona above active regions. The originally proposed techniques of stereoscopy and the use of Spectro-Spatial Maximum Entropy Method (Bong et al. 2005) were not fruitful, mostly due to the important role the VLA data play in the calibration of the OVSA data, and pinning down the spectral analysis. Because the VLA data were only available on a single day, the stereoscopy of AR 10923 had to be abandoned. However, the revision to existing imaging programs and the implementation of the L_1 self-calibration method produce brightness temperature maps of an unprecedented quality for OVSA data. OVSA is undergoing a complete upgrade, increasing the number of antennas and completely replacing hardware with modern, digital technology (Gary 2010). Although this combination will produce an improved *uv* coverage excellent polarization calibration, and higher time and frequency resolution, proper care must still be given to the imaging algorithms. The stable, 27-element VLA does not have a point-and- click imaging algorithm because a "best mapping technique" does not apply to all observations (Briggs, 1995), which is likely to be true even for a solar dedicated instrument.

The quality of the OVSA maps presented in this dissertation was verified with comparisons to VLA data taken on the same day, as well as through the improved continuity in the spectra. This improvement to the spectra allowed for the development of an automated model fitting algorithm. In order to fit a variety of spectra, some of which had a positive slope in what is normally a flat temperature domain, a two component model was adopted, with good results. Such models generally require additional components, since all observations of the solar corona indicate that it is a highly inhomogenous medium, in temperature and spatial structure. Vourlidas et al (1994) achieved optimal fits to spectra made from the few frequencies available

from the VLA with multi-thermal free-free emission models. That this should apply to gyroresonance spectra and combined mechanism spectra is obvious. However, it should be the data that guide the model fits, and the predicted quality of the upgraded OVSA holds great promise towards this end.

The optimization of the magnetograms used for the potential field extrapolation was key to some of the findings in this dissertation. Without a field of view large enough to encompass all of the magnetic flux in the plage, the NLFF extrapolation originally attempted gave magnetic field values inconsistent with those expected from the radio and did not show the proper shifts in heights necessary to match the locations of the low frequency brightness temperature maps. The potential field extrapolation used is apparently only affected by the divergence from potentiality in a few, constrainable regions, but the overall model proved quite useful in this study. As radio spectral analysis presented here is attempted on future observations, possibly of more complicated, non-potential regions, it will be necessary to reconcile the requirements of a vector magnetic field with the need to encompass as much of the pertinent flux as possible in order to produce extrapolations that can better approximate the true coronal magnetic field distribution.

One major finding in active region structure was the association of the dominance of free-free and gyroresonance radio emission with different portions of magnetic loops. The emission is not exclusive to the tops (free-free) or the foot points (gyroresonance), and the result should not be taken to imply a complete spatial separation of these processes. Rather, the differentiation of the regions where the two mechanism dominate can be used to place constraints of the transport of energy along the loop. Stereoscopic observations analyzed in this manner will make these constraints much more concrete, as the need for an extrapolation to obtain heights is removed, and additional clues to the true three-dimensional distribution along all portions of the corona are revealed.

Another major result is the association of radio and X-ray free-free emission with two distinct loop systems. This led to the observation that X-ray loops have foot points at exactly the locations where (1) the radio-derived magnetic field values differ from those in the extrapolation, (2) there was an increased gyroresonance temperature, and (3) the magnetic structure at the surface coincides with the sunspot penumbra. Because the foot points of the slightly cooler radio loops were within the umbra, the two regions were determined to represent different environments. This corroborated similar conclusions from previous researchers (Vourlidas et al 1997). This conclusion ties in perfectly with those from the implementation of a three-dimensional mapping technique for the base of the corona and transition region. There it was found that there is a cool core of material directly above the sunspot, in the regions where the radio and non-emitting loops converge. The base of the corona and the transition region drop in height, as well as come closer together, over the penumbra, suggesting a greater heating function and producing gyroresonance emission at the lower heights where the photospheric magnetic fields are still strong. These conclusions about the structure in the corona present explanations for the reasons why radio observations appear as they do, the inconsistencies in the comparison of radio and X-ray temperature and emission measure values, the lateral displacement of the peaks in photospheric and coronal base magnetic field, and suggest that different heating functions are working in the umbral and penumbral regions.

This all comes down to what may be considered a beautiful realization. The extent to which the sunspot dominates the active region structure over a much larger area is remerkable. Granted, the sunspot has a magnetic field strength much stronger than anywhere else on the solar surface and its control over the region should be expected. Nevertheless, from a small region it inhibits convection to set up a varied landscape in the corona above it, it controls the manner in which temperature and energy is transported in the corona, separating out the various loop systems observed

at different wavelengths through different mechanisms, ultimately driving out large volumes of plasma and energy through Coronal Mass Ejections and flares. Understanding sunspots , then, is essential to an understanding of the associated active regions and activity.

REFERENCES

2009, Hinode Solar Optical Telescope Data Analysis Guide

Alissandrakis, C. E. 1981, A&A, 100, 197

Alissandrakis, C. E., Gel'Frejkh, G. B., Borovik, V. N., Korzhavin, A. N., Bogod, V. M., Nindos, A., & Kundu, M. R. 1993, A&A, 270, 509

Alissandrakis, C. E., & Kundu, M. R. 1982, , 253, L49

Alissandrakis, C. E., Kundu, M. R., & Lantos, P. 1980, A&A, 82, 30

Aschwanden, M. J. 2006, Phyics of the Solar Corona, an Introduction (Berlin, Germany, Chapter 1: Springer-Praxis)

Brosius, J. W., Willson, R. F., Holman, G. D., & Schmelz, J. T. 1992, , 386, 347

Chiuderi-Drago, F., Bandiera, R., Willson, R. F., Slottje, C., Falciani, R., Antonucci, E., Lang, K. R., & Shibasaki, K. 1982, Sol. Phys., 80, 71

Chiuderi Drago, F., Felli, M., & Tofani, G. 1977, A&A, 61, 79

Cornwell, T., & Fomalont, E. B. 1999, in Astronomical Society of the Pacific Conference Series, Vol. 180, Synthesis Imaging in Radio Astronomy II, ed. G. B. Taylor, C. L. Carilli, & R. A. Perley, 187

De Rosa, M. L., et al. 2009, ApJ, 696, 1780

Delaboudinière, J., et al. 1995, Sol. Phys., 162, 291

Dulk, G. A. 1985, ARA&A, 23, 169

Dulk, G. A., & Gary, D. E. 1983, A&A, 124, 103

Felli, M., Lang, K. R., & Willson, R. F. 1981, ApJ, 247, 325

Foukal, P. V., Noyes, R. W., Reeves, E. M., Schmahl, E. J., Timothy, J. G., Vernazza, J. E., Wilhbroe, G. L., & Huber, M. C. E. 1974, ApJ Lett., 193, L143

Gary, D. E., & Hurford, G. J. 1987, ApJ, 317, 522

—. 1994, ApJ, 420, 903

—. 2004, Solar and Space Weather Radiophysics, ed. D. E. Gary & C. U. Keller (Kluwer Academic Publishers)

Gary, G. A., & Hagyard, M. J. 1990, Sol. Phys., 126, 21

Gelfreikh, G. B. 2004, Solar and Space Weather Radiophysics, ed. D. E. Gary & C. U. Keller (Kluwer Academic Publishers)

Georgoulis, M. K., & LaBonte, B. J. 2007, ApJ, 671, 1034

Gopalswamy, N., White, S. M., & Kundu, M. R. 1991, ApJ, 379, 366

Holt, S. S., & Ramaty, R. 1969, Sol. Phys., 8, 119

Hurford, G. J. 1986, in Solar Flares and Coronal Physics Using P/OF as a Research Tool, ed. E. Tandberg, R. M. Wilson, & R. M. Hudson (Washington D.C.: NASA)

Kakinuma, T., & Swarup, G. 1962, ApJ, 136, 975

Katsukawa, Y., et al. 2007, PASJ, 59, 577

Klimchuk, J. A., & Gary, D. E. 1995, , 448, 925

Kundu, M. R., Schmahl, E. J., & Rao, A. P. 1981, A&A, 94, 72

Lang, K. R., & Willson, R. F. 1980, in IAU Symposium, Vol. 86, Radio Physics of the Sun, ed. M. R. Kundu & T. E. Gergely, 109

Lang, K. R., & Willson, R. F. 1982, ApJ Lett., 255, L111

Lang, K. R., Willson, R. F., & Gaizauskas, V. 1983, ApJ, 267, 455

Lang, K. R., Willson, R. F., Smith, K. L., & Strong, K. T. 1987a, ApJ, 322, 1035

—. 1987b, ApJ, 322, 1044

Lang, K. R., et al. 1993, , 419, 398

Lee, J. W., Gary, D. E., & Hurford, G. J. 1993, Sol. Phys., 144, 349

Lites, B. W., Elmore, D. F., & Streander, K. V. 2001, in Astronomical Society of the Pacific Conference Series, Vol. 236, Advanced Solar Polarimetry – Theory, Observation, and Instrumentation, ed. M. Sigwarth, 33

Melrose, D. B., & McPhedran, R. C. 1991, Electromagnetic Processes in Dispersive Media, ed. Melrose, D. B. & McPhedran, R. C. (Cambridge University Press)

Metcalf, T. R., et al. 2008, Sol. Phys., 247, 269

Mok, Y., Mikić, Z., Lionello, R., & Linker, J. A. 2005, ApJ, 621, 1098

Nindos, A., Kundu, M. R., White, S. M., Shibasaki, K., & Gopalswamy, N. 2000, ApJS, 130, 485

Nitta, N., et al. 1991, , 374, 374

Ramaty, R., & Petrosian, V. 1972, ApJ, 178, 241

Rosner, R., Tucker, W. H., & Vaiana, G. S. 1978, ApJ, 220, 643

Scherrer, P. H., et al. 1995, Sol. Phys., 162, 129

Schmelz, J. T., Holman, G. D., Brosius, J. W., & Gonzalez, R. D. 1992, , 399, 733

Schmidt, H. U. 1964, NASA Special Publication, 50, 107

Schrijver, C. J., et al. 2006, Sol. Phys., 235, 161

—. 2008, ApJ, 675, 1637

Schwab, F. R. 1982, http://www.vla.nrao.edu/memos/sci/136.pdf

Shevgaonkar, R. K., & Kundu, M. R. 1985, Sol. Phys., 98, 119

Takakura, T. 1972, Sol. Phys., 26, 151

Thompson, A. R., Clark, B. G., Wade, C. M., & Napier, P. J. 1980, ApJS, 44, 151

Vourlidas, A. 1996, PhD thesis, New Mexico Inst. Mining Tech., (1996)

Vourlidas, A., Bastian, T. S., & Aschwanden, M. J. 1997, ApJ, 489, 403

Vourlidas, A., Bastian, T. S., Nitta, N., & Aschwanden, M. J. 1996, Sol. Phys., 163, 99

Webb, D. F., Holman, G. D., Davis, J. M., Kundu, M. R., & Shevgaonkar, R. K. 1987, , 315, 716

White, S. M. 2004, Solar and Space Weather Radiophysics, ed. D. E. Gary & C. U. Keller (Kluwer Academic Publishers)

White, S. M., & Kundu, M. R. 1997, Sol. Phys., 174, 31

White, S. M., Kundu, M. R., & Gopalswamy, N. 1992, ApJS, 78, 599

Zheleznyakov, V. V. 1962, Soviet Ast., 6, 3

—. 1970, Radio emission of the sun and planets, ed. Zheleznyakov, V. V.

Zlotnik, E. Y., Kundu, M. R., & White, S. M. 1996, Radiophysics and Quantum Electronics, 39, 255

Zlotnik, E. Y., White, S. M., & Kundu, M. R. 1998, in Astronomical Society of the Pacific Conference Series, Vol. 155, Three-Dimensional Structure of Solar Active Regions, ed. C. E. Alissandrakis & B. Schmieder, 135